Dipole response of ^{238}U to polarized photons below the neutron-separation energy

by
Samantha L. Hammond

A dissertation submitted to the faculty of the University of North Carolina at Chapel Hill
in partial fulfillment of the requirements for the degree of Doctor of Philosophy
in the Department of Physics and Astronomy.

Chapel Hill
2011

Approved by:

Dr. Hugon Karwowski

Dr. Jonathan Engel

Dr. Reyco Henning

Dr. Christian Iliadis

Dr. Nalin Parikh

Abstract

SAMANTHA L. HAMMOND: Dipole response of ^{238}U to polarized photons
below the neutron-separation energy (Under the direction of Dr. Hugon Karwowski)

An investigation of dipole states in ^{238}U is important for the fundamental understanding of its structure. In the present work, precise experimental information on the distribution of $M1$ and $E1$ transitions in ^{238}U has been obtained with the nuclear resonance fluorescence technique at the High-Intensity γ-ray Source at the Triangle Universities Nuclear Laboratory. Using 100% linearly-polarized, monoenergetic γ-ray beams with incident energies of 2.0-6.2 MeV, the spin, parity, integrated cross section, width, branching ratio, and γ-strength of the observed deexcitations were determined. These measurements form a unique data set that can be used for comparison with theoretical models of collective excitations in heavy, deformed nuclei. The data can also provide isotope-specific signatures to search for special nuclear materials.

Acknowledgments

This work was supported in part by the United States Department of Homeland Security through the Academic Research Initiative with grants 2008-DN-077-ARI014 and 2008-DN-077-ARI010 and by the United States Department of Energy with grant DE-FG02-97ER41041.

I would like to thank my collaborators: Dr. A. S. Adekola, Dr. C. T. Angell, and Dr. H. J. Karwowski from the *University of North Carolina at Chapel Hill*. Dr. J. H. Kelley from *NC State University*. Dr. E. Kwan, Dr. G. Rusev, Dr. A. P. Tonchev, and Dr. W. Tornow from *Duke University*.

The depleted uranium targets used in this work were loaned by Lawrence Livermore National Laboratory, in particular Dr. M. S. Johnson and Dr. D. P. McNabb. Data-taking assistance and technical discussions were appreciated from the following: C. Huibretgse, Dr. A. L. Hutcheson, Dr. R. Raut, G. C. Rich, D. R. Ticehurst, and J. R. Tompkins. Helpful explanations and QRPA calculation discussions were also most welcomed from Dr. E. Guliyev.

I would also like to thank: My parents Ray and Diane, my sisters Cathy and Jenny, my brother-in-laws Jeff and Kevin, and my grandmother Catherine, for all of their love and support these past five years. My unbelievably good friends, especially Briana, for

everything I could ever have wished for in a best friend. I would never have made it this far without all of you.

Thank you God, for all of the strength and integrity you have most graciously bestowed upon me. Every one of the life lessons you had me learn has come from your love for me. As Father Anthony DeMello said, "Faith is an openness to truth, no matter the consequences, no matter where it leads."

Table of Contents

List of Tables

List of Figures

List of Abbreviations

B	backward-angled detector
b	barns
cm	centimeters
Co	cobalt
Cu	copper
DHS	Department of Homeland Security
DNDO	Domestic Nuclear Detection Office
$E1$	electric dipole
$E2$	electric quadrupole
e	electron
eV	electron volts
Er	erbium
FEL	free electron laser
FINDER	fluorescence imaging in the nuclear domain with extreme radiation
FWHM	full-width half-maximum
fm	femtometers
Gd	gadolinium
GDR	giant dipole resonance
GeV	giga-electron volts
g	grams
H	horizontal detector

Hf	hafnium
HIγS	high intensity γ-ray source
HPGe	high purity germanium
h	hours
IAS	isobaric analog state
IVGDR	isovector giant dipole resonance
IVGQR	isovector giant quadrupole resonance
ITDB	illegal trafficking database
K	potassium
keV	kilo-electron volts
$\mu_N{}^2$	nuclear magnetons squared
$M1$	magnetic dipole
MCNPX	Monte Carlo n-particle extended
MeV	mega-electron volts
MHz	mega-Hertz
MLO	modified double Lorentzian fit to the GDR
m	meters
mb	milli-barns
meV	milli-electron volts
mm	millimeters
NaI	sodium iodide
NRF	nuclear resonance fluorescence

n	neutron
nm	nanometers
Pb	lead
PDR	pygmy dipole resonance
p	proton
QPNM	quasiparticle-phonon nuclear model
QRPA	quasiparticle random-phase approximation
RF	radio frequency
RPA	random-phase approximation
SLO	standard double Lorentzian fit to the GDR
Sm	samarium
SNM	special nuclear materials
Tl	thallium
Th	thorium
T-REX	Thomson-radiated extreme x-ray system
U	uranium
US	United States
V	vertical detector

List of Symbols

$\mid 0\rangle$	true ground state wavefunction
α	fine structure constant
${\alpha_\lambda}^\dagger$	quasiparticle creation operator
α_s	statistical significance
A	mass number - total number of protons and neutrons
A	generic amplitude of the cross section
$\mathbf{A}_\parallel$	parallel component of the amplitude of the cross section
$\mathbf{A}_\perp$	perpendicular component of the amplitude of the cross section
$\mathbf{A}_\lambda(\gamma_2)$	angular correlation coefficient for the scattered γ ray
A_{HV}	azimuthal asymmetry
$\bar{A}_{HV}$	average azimuthal asymmetry of the continuum
A_{ijkl}	coefficient of the RPA equations
$a^\dagger$	particle (hole) creation operator
a	Doppler width coefficient
β_2	quadrupole deformation parameter
$\mathbf{B}'_\lambda(\gamma_1)$	angular correlation coefficient for the incident γ ray
$\mathbf{B}(\Pi L)$	γ-ray dipole strength
$\mathbf{B}(E1)_\alpha$	electric dipole strength due to α-clustering
$\mathbf{B}(E1$**,GDR)**	electric dipole strength from the GDR
$\mathbf{B}(E1)_{oct}$	electric dipole strength due to octupole deformations
$\mathbf{B}(1 \rightarrow 0)$	reduced transition probability of $J = 1$ state decaying into the ground state

$\mathbf{B}(1 \rightarrow 2)$	reduced transition probability of $J = 1$ state decaying into $J = 2$ state
B_{ijkl}	coefficient of the RPA equations
b	branching ratio
C_{att}	attenuation coefficient
c	speed of light
c1	normalizing coefficient for quasiparticle operator
c2	normalizing coefficient for quasiparticle operator
$\mathbf{c}_i$	fitting coefficients for the simulated efficiency
$\mathbf{D}_\alpha$	electric dipole moment due to α-clustering
$\mathbf{D}_{oct}$	electric dipole moment due to octupole deformations
d	thickness of target
dΩ	solid angle
χ	isotopic abundance
Δ	Doppler width
δ	deformation parameter
D	mean level spacing
D	Delbrück scattering amplitude
$\mathbf{D}_\parallel$	parallel component of the Delbrück scattering amplitude
$\mathbf{D}_\perp$	perpendicular component of the Delbrück scattering amplitude
DL	detection limit
ϵ	corrections to the form factor for electron binding
$\epsilon(E)$	detector efficiency

ϵ_α	single-particle energy
η	clustering amplitude
$\mathbf{E}$	incident photon energy
$\mathbf{E}$	rest energy
$\mathbf{E}_0$	energy of the ground state
$\mathbf{E}_1$	energy of the first excited state
$\mathbf{E}_{1\rightarrow0}$	energy of a transition from a $J = 1$ excited state to the ground state
$\mathbf{E}_{1\rightarrow2}$	energy of a transition from a $J = 1$ excited state to the first excited state
$\mathbf{E}_\nu$	energy parameter for the GDR
$\mathbf{E}'$	shifted rest energy
E_{beam}	energy centroid of the beam
E_c	final energy of a Compton-scattered γ ray
$\mathbf{E}_{GDR}$	energy of the GDR
$\mathbf{E}_n$	excitation energy of the n^{th} state
$\mathbf{E}_{oct}$	energy of the low-lying octupole states
$\mathbf{E}_r$	resonance energy
$\mathbf{E}_x$	excitation energy
$\hat{e}_\parallel$	parallel component of the momentum vector of an incoming photon
$\hat{e}'_\parallel$	parallel component of the momentum vector of an outgoing photon
$\hat{e}_\perp$	perpendicular component of the momentum vector of an incoming photon
$\hat{e}'_\perp$	perpendicular component of the momentum vector of an outgoin photon
$\mathbf{e}$	charge of the electron

$\mathbf{F}_\lambda$	Ferentz-Rosenzweig coefficient
$F_n(q)$	form factor
$\hat{f}$	general one-body external field operator
$\vec{f}(E)$	strength function
f	function for the Delbrück amplitude
Γ	total width
$\Gamma\uparrow$	spreading width
Γ_0	ground-state width
Γ_1	first excited-state width
Γ_ν	width parameter for the GDR
Γ_r	resonance width parameter for the GDR
Γ_n	n^{th} partial width
$G_n(q)$	modified form factor
g	statistical factor
g	function for the Delbrück amplitude
g_{IS}	isoscalar orbital gyromagnetic factor of the ground state rotational band
g_π	gyromagnetic factor for the protons
g_ν	gyromagnetic factor for the neutrons
$\hbar$	Planck's constant
$\hat{H}$	Hamiltonian
H_{sp}	one-body Hamiltonian
$\hat{H}_{sqp}$	Hamiltonian of the single-quasiparticle motion

$\bar{H}_C$	mixing matrix element
$\hat{h}_\delta$	interactions for transitional and Galilean symmetries
$\hat{h}_0$	isoscalar restoring interaction
$\hat{h}_1$	isovector restoring interaction
$\mid HF\rangle$	Hartree-Fock ground state wavefunction
$\mathcal{I}_\pi$	moment of inertia for protons
$\mathcal{I}_\nu$	moment of inertia for neutrons
$I_\parallel$	integrated cross section parallel to the polarization plane
$I_\perp$	integrated cross section perpendicular to the polarization plane
I_s	integrated photon scattering cross section
i	number of particle states
$\vec{J}$	total angular momentum
$\mathbf{J}$	final-state spin
$\mathbf{J}_0$	ground-state spin
$\mathbf{J}_x$	excited-state spin
j	number of hole states
$\mathbf{K}$	rotational quantum number
$\hat{k}$	momentum vector of an incoming photon
$\hat{k}'$	momentum vector of an outgoing photon
$\mathbf{k}$	Boltzmann's constant
$\mathbf{k}_\lambda$	polarization coefficient
$\lambda\!\!\!^{-}$	Compton wavelength

L	orbital angular momentum
L	the order of multipole radiation
$\vec{L}_p$	orbital angular momentum for the protons
$\vec{L}_n$	orbital angular momentum for the neutrons
μ_x	mass-attenuation coefficient
$\mathbf{M}_n$	nuclear mass
m	mass of the electron
N	coherent nuclear resonance scattering amplitude
$\mathbf{N}_{\parallel}$	parallel component of the nuclear resonance scattering amplitude
$\mathbf{N}_{\perp}$	perpendicular component of the nuclear resonance scattering amplitude
N	number of neutrons
N	number of attenuated counts
$\mathbf{N}_0$	number of unattenuated counts in peak area from spectrum
$\mathbf{N}_0$	number of counts from a transition to the ground state
$\mathbf{N}_1$	number of counts from a transition to the first excited state
$\mathbf{N}_\pi$	valence proton boson number
$\mathbf{N}_\nu$	valence neutron boson number
$\mathbf{N}_A$	Avogadro's number
N_B	background counts
$\mathbf{N}_c$	number of counts in the Compton scattered peak
N(E)	number of incident γ rays with respect to photon energy
n	number of standard deviations above the 2σ detection limit

$\mathbf{n}$	number of particles or holes
$\mathbf{n}_{Cu}$	areal density of the copper plate
$\mathbf{n}_t$	resonant target nuclei per area
$\mathbf{n}_{tar}$	number of target nuclei per area
$\mathbf{n}_{tot}$	total nuclei per area
$\mid n\rangle$	excited state wavefunction
ϕ	polar angle
$\Phi(E)$	flux of incident γ rays per energy
Π	E for electric radiation or M for magnetic radiation
$\Psi(x,t)$	wave function
$\mathbf{P}_{\nu}^{(2)}(\cos\theta)$	second order Legendre polynomial
$\mathbf{P(E}_{\gamma}$	degree of polarization
Q_0	quadrupole moment
q	momentum transfer
$\mid QRPA\rangle$	ground-state wave function of the QRPA calculation
ρ	density of material
$\rho(\vec{r})$	charge density
$\mathbf{R}$	nuclear Rayleigh scattering amplitude
$\mathbf{R}_{\parallel}$	parallel component of the nuclear Rayleigh scattering amplitude
$\mathbf{R}_{\perp}$	perpendicular component of the nuclear Rayleigh scattering amplitude
$\mathbf{R}$	ratio of reduced transition probabilities
R_{exp}	experimental branching ratio

Rx	count rate with absorber of thickness x
r_0	radius of the electron
$\mid RPA\rangle$	ground state wave function of the RPA calculation
Σ	analyzing power
$\Sigma B(\Pi L)$	summed transition strength
σ	standard deviation
σ_{abs}^{max}	maximum value of σ_{abs}
$\sigma_{abs}(E)$	resonance absorption cross section
σ_c	Compton scattering cross section
σ_{coh}	total coherent-scattering cross section
$\sigma_D(E)$	Doppler broadened absorption cross section
σ_e	total effective electronic absorption cross section
$\sigma_e l$	total elastic cross section
$\sigma_{\gamma\gamma}(E)$	elastic photon scattering cross section
$\sigma_i(E)$	i^{th} partial NRF cross section
$\sigma_{NRF}(E)$	nuclear resonance fluorescence cross section
σ_{ph}	photoelectric cross section
σ_{pp}	pair-production cross section
σ_ν	amplitude parameter for the GDR
σ_r	resonance amplitude parameter for the GDR
σ_{tot}	average total γ-ray interaction cross section
S(E)	strength function

S_a	relative self-absorption
S_n	neutron separation energy
$\mathbf{t}$	time
$\mathbf{T}$	nuclear Thomson scattering amplitude
$\mathbf{T}_{\parallel}$	parallel component of the nuclear Thomson scattering amplitude
$\mathbf{T}_{\perp}$	perpendicular component of the nuclear Thomson scattering amplitude
$\mathbf{T}$	absolute temperature of the material
$\mathbf{T}_{eff}$	effective temperature
$\mathbf{T}_f$	final-state temperature
Θ_D	Debye temperature
θ	azimuthal angle
θ_c	Compton scattering angle
$\hat{V}_{\sigma\tau}$	spin-isospin interaction
$\hat{V}_{pair}$	monopole pairing interaction
$\hat{V}_{ph}$	particle-hole interaction
$\hat{V}_{pp}$	particle-particle interaction
$\mathbf{V(r)}$	electrostatic potential
$\mathbf{V}$	particle-hole interaction potential
$\mathbf{v}$	velocity
Ω	solid angle
ω_D	centroid energy of the isovector giant dipole resonance
$\omega_{\Pi L}$	mean excitation energy

$\hat{W}_1$	coherent isovector dipole vibrations of protons and neutrons
$\mathbf{W}(\theta)$	angular correlation depending on angle θ only
$\mathbf{W}(\theta)_{0\to1\to0}$	angular correlation of the J=1 state decaying back to the ground state
$\mathbf{W}(\theta)_{0\to1\to2}$	angular correlation of the J=1 state decaying to the first excited state
$\mathbf{W}(\theta,\phi)$	angular correlation depending on both angles θ and ϕ
ξ	contribution from the isovector giant quadrupole dipole resonance
$X_{ij}{}^{n}$	amplitude from the RPA equations
$Y_{ij}{}^{n}$	amplitude from the RPA equations
$\hat{\zeta}_n$	destruction operator
$\hat{\zeta}_n{}^{\dagger}$	creation operator
$\mathbf{Z}$	atomic number - number of protons

Chapter 1

Introduction

The research detailed in this dissertation describes the dipole response of ^{238}U to linearly-polarized photons below the neutron separation energy of $S_n = 6.154$ MeV. The primary goal of the project was to identify and to accurately measure discrete dipole excitations for the purpose of understanding the low-energy structure of ^{238}U. Dipole excitations can provide insight into the collective nature of nuclear excitations in general, such that the induced motion isn't centered around one particle but the interconnected motion of all the particles of the system. This complete low-energy characterization can be compared with theoretical calculations in order to improve the ability to consistently predict the structure of nuclei under the absence of experimental data. Equally, this spectroscopic information would provide a unique signature for identification of ^{238}U from other isotopes, which is important for national security purposes. Achieved measurement uncertainties were around 7-10%.

In the early 1980s, with the discovery of a new low-energy magnetic dipole ($M1$) collective mode, the "scissors mode", many measurements of rare-earth and actinide nuclei were conducted to observe it, ^{238}U being among the chosen nuclei studied [1]. These initial mea-

surements were confined to narrow energy ranges based on antiquated model calculations and theoretical predictions, and as consequence, important nuclear structure information was likely ignored. In recent years, it has become possible to improve the sensitivity of photon-scattering experiments significantly due to the availability of quasi-monoenergetic, high-intensity, and linearly-polarized beams. With these improvements, a broader energy range was probed in the present work increasing the observed energy range from a spread of 0.6 MeV [1] to one of 4.2 MeV. In addition, not only $M1$ deexcitations, but electric dipole ($E1$) and quadrupole ($E2$) deexcitations were investigated in the present work, allowing a more complete characterization of the underlying nuclear structure.

The rest of this chapter will attempt to provide external motivation for this project. Chapter 2 lays out the basic scientific understanding of interactions of photons with the nucleus and of the collective modes of excitations as a foundation for the rest of the chapters. This chapter also details the prescriptions used to explain experimental observations. A brief description of the theoretical calculations is given in Chapter 3. Chapter 4 addresses the previous measurements of ^{238}U that are relevant to this dissertation as well as providing some details about the spectroscopy of nuclei with $140 < A < 180$ for comparison with the present work in later chapters. The facility at which the experiments were performed and the description of the experimental setup are specified in Chapter 5 as well as a brief outline of the simulation codes important to data analysis. Experimental results are presented in Chapter 6 and a discussion follows in Chapter 7. Summary and final remarks are given in Chapter 8.

1.1 Nuclear Structure

Uranium is a deformed, heavy-mass nucleus with a large neutron excess. Many nuclear structure models cover the region of masses up to ^{208}Pb, since it is the heaviest spherical nucleus that can be roughly described by simple models [2, 3]. However, some collective modes of excitation, such as the $M1$ "scissors mode" or the $E1$ pygmy dipole resonance (see Chapter 2 for more details) originate from nuclear deformations. Spherical nuclei, therefore, can provide a foundation for the complex calculations that deformed nuclei need in order to explain the nature of the deformation-dependent transition strength. However, more experimental data on deformed nuclei, such as ^{238}U, are needed since it allows access to challenging nuclear structure problems for which calculations can be performed for improvement in predictions of observed phenomena. Better calculations can provide information on the structure of nuclei that can't be obtained experimentally.

Additionally, previous experiments used to characterize the low-energy structure of ^{238}U primarily used continuous Bremsstrahlung γ-ray beams (see Chapter 4). Since these types of beams would generate all deexcitations from many different states, unique identification of excited states, as well as quantifying the experimental branching ratios, becomes a challenging undertaking (see Chapter 7). Fortunately, in recent years, it has become possible to improve the sensitivity of photon-scattering experiments significantly with the availability of quasi-monoenergetic and linearly-polarized beams which are well-suited for nuclear resonance fluorescence experiments. These beams have narrow energy spreads that can eliminate any uncertainty in identification of a transition within an energy survey.

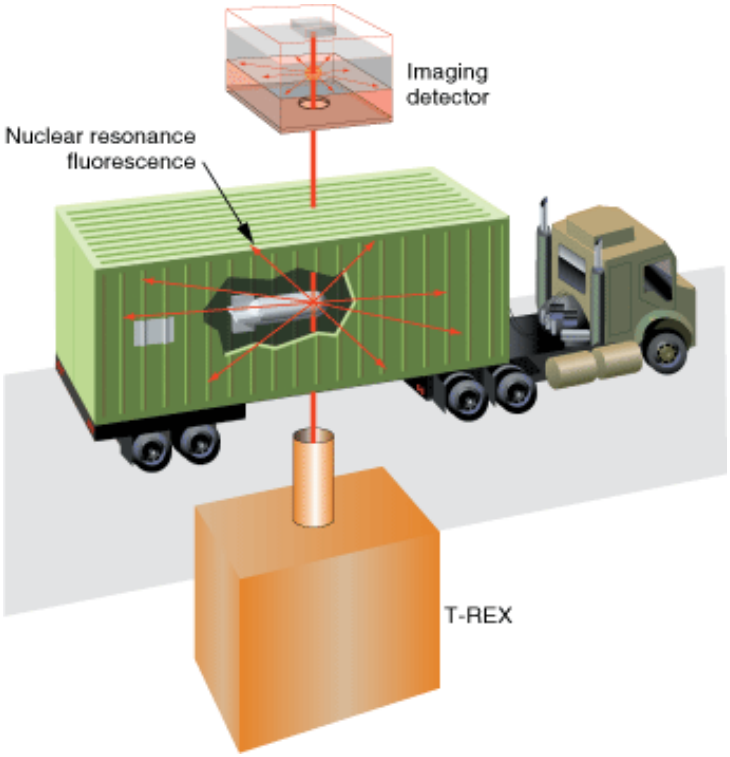

Figure 1.1: T-REX, a Thomson-radiated extreme x-ray system combined with nuclear resonance fluorescence techniques, are used to detect small amounts of nuclear materials and image their distributions within a container. Reproduced from Ref. [4].

Use of polarized beams allows assignment of parity of the excited states and provides insight into the properties of observed transitions and accompanying collective structure of actinides.

1.2 Applications

There are potentially many uses for the unique identification of materials that may be of special interest. National security interests may lie in the identification and characterization of special nuclear materials (SNM) within the context of the interrogation of shipment containers for hidden SNM (see Fig. 1.1), of nuclear waste barrels, of nuclear warheads for disarmament treaty monitoring, or of spent nuclear fuel from reactors. The nuclear

resonance fluorescence (NRF) technique (see Chapter 2 for details) allows for the nondestructive imaging of the radionuclides within a particular container of interest, which is why it is the primary mechanism for all of these applications.

Regardless of what is being assayed, the techniques and procedures outlined in this dissertation could become an integral part of proliferation resistance and monitoring. A comprehensive investigation of a shipment container, a nuclear waste barrel, or something of a similar disposition, demands good state-of-the-art detector development as well as a well-established database. Also, high-intensity photon beams, ranging from 2-8 MeV, are needed since SNM can not be easily shielded by heavy-mass materials. Finally, using the well-understood physical interaction of electromagnetism provides the capacity for the models to quantitatively describe observed phenomena.

1.2.1 National Security

This project was brought into existence as a response to the increase of global terrorism and the United States (US) government's need for protecting its citizens. On April 15, 2005, the Department of Homeland Security (DHS) created a subdivision called the Domestic Nuclear Detection Office (DNDO) to prevent and to assess threats from reaching and within the US borders under the following seven-point mission [5]:

- to develop the global nuclear detection and reporting architecture;
- to develop, acquire, and support the domestic nuclear detection and reporting system;
- to characterize detector system performance before deployment;
- to establish situational awareness through information sharing and analysis;
- to establish operational protocols to ensure detection leads to effective response;

- to conduct a transformational research and development program;
- to provide centralized planning, integration, and advancement of US nuclear forensics programs.

One of the bigger efforts of the DNDO was the Academic Research Initiative which provides funds to universities and contractors for the procurement of technologies and assessment tools to accomplish the above mission. One such project was the scanning of shipment containers at ports. Many containers pass through US ports daily, too many to involve the physical examination of each container to search for only a few grams of SNM. Thorium and the uranium isotopes form the majority of the nuclear materials that are illegally trafficked throughout the world (see Fig. 1.2). An effective solution will involve both the identification of signatures from materials such as those mentioned previously as well as the methodology for assessing high risk containers without disrupting the flow of commerce. Therefore, scanning containers and subsequently determining their contents must be done in an efficient and expeditious manner.

The 'nuclear car wash' was invented (see Fig. 1.1) as one possible solution. This technique involves high-intensity γ rays directed on all sides of the container with detectors located around the outside to collect signature γ rays emitted from interaction with the contents inside. Basic science research of the low-energy nuclear structure of SNM would identify and distinguish highly-enriched uranium from other commodities present in the shipment container. These laboratory techniques are being commissioned for public use through commercially available cargo and people scanners from companies such as Passport Systems [6] and Rapiscan Systems [7]. Additional to the nuclear car wash concept, another system, FINDER (Fluorescence Imaging in the Nuclear Domain with Extreme Ra-

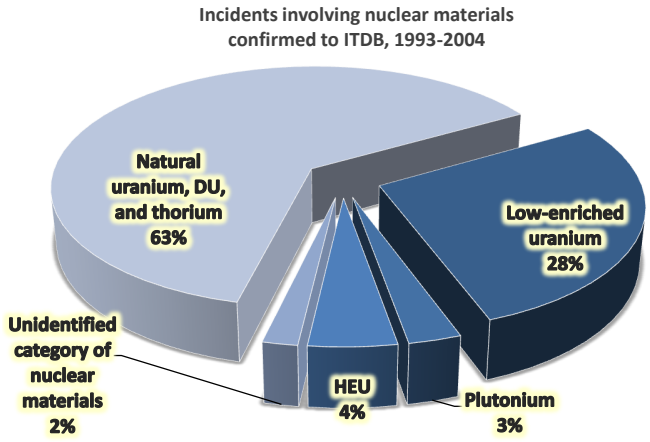

Figure 1.2: Incidences involving illegal trafficking of special nuclear materials between the years of 1993 and 2004. Reproduced from Ref. [10].

diation), developed at Lawrence Livermore National Laboratory, uses a combination of radiology and NRF scanning technologies for SNM detection [8]. Experiments [9] were performed using strong, well-characterized states in SNM to validate the abilities of these detection systems for isotope detection.

1.2.2 Nuclear Waste and Spent Fuel

The employment of NRF techniques within the management of nuclear waste barrels or spent fuel rods from reactors is another important application. Identifying the individual concentrations of about 20 nuclides to be below their required activity levels is a part of the clearance process which determines whether or not the radioactive waste material as a whole is below the required levels. Once these concentrations are identified, the waste is separated and categorized by concentration levels for distribution to an appropriate storage facility. Hajima *et al.* [11] proposed a method using the NRF process which establishes better assessments of the concentrations within nuclear waste for appropriate storage clas-

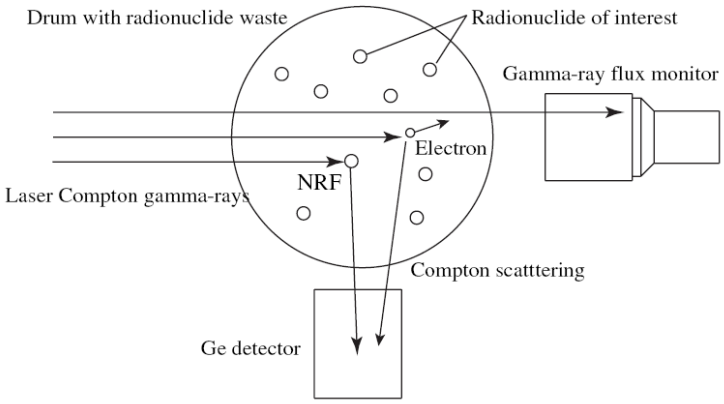

Figure 1.3: A schematic view of nuclear resonance fluorescence measurement. Reproduced from Ref. [11].

sifications. Fig. 1.3 describes this process pictorially.

Properly determining the quantity of fissionable nuclides within spent fuel rods before and after reprocessing is extremely important for nonproliferation efforts in safeguarding SNM. Current methods use simulation codes to calculate the concentrations of fissionable nuclides, which may not produce the accuracy that a physical measurement could provide [12].

Whether safeguarding the American borders through active interrogation of shipment containers or monitoring the concentration levels of particular radioactive nuclides, these applications depend on a thorough knowledge of the application of NRF techniques for real measurements as well as an all-encompassing NRF database for nuclei. The current experiments of this dissertation attempt to produce robust NRF data-acquisition algorithms that could be used for other purposes besides surveying low-energy structure of nuclei, as well as the characterization of one SNM (^{238}U) as a basis of the success of this algorithm and as a foundation for other future measurements on SNM.

Chapter 2

Photon Interactions with the Nucleus

Below the neutron separation energy S_n, photons can interact with a nucleus in two ways: (1) the photon can be *absorbed* by the target nucleus or (2) it can be *scattered* from the nucleus. All other photon interactions fall into one of these categories. Absorption includes the processes of the photoelectric effect and pair production. Photon scattering can be further subdivided into elastic and inelastic scattering. Inelastic scattering involves nuclear Raman scattering as well as Compton scattering, the latter being the process by which γ rays are inelastically scattered from electrons. Compton scattering is an important process since it allows for the measurement of the absolute beam flux during data collection (see Chapter 5 and 6 for more details).

One of the subjects of this dissertation is the investigation of the total elastic-scattering cross section, σ_{el}, for ^{238}U. As such, both the incoherent and coherent part of elastic scattering are observed. The incoherent process of elastic scattering is known as nuclear resonance fluorescence, which is the primary method applied in the current measurements. Coherent elastically-scattered γ rays result from Thomson (T), Rayleigh (R), Delbrück (D), and nuclear resonance (N) scattering which are the components of σ_{el}.

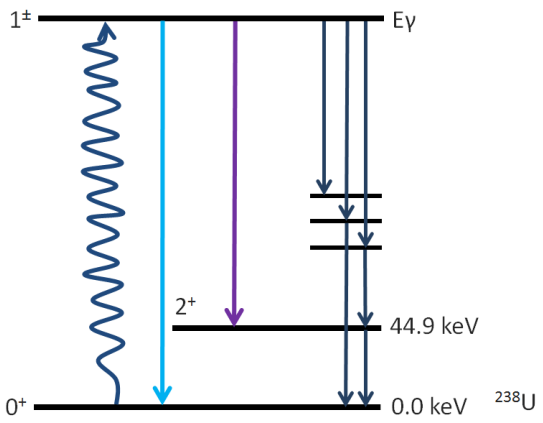

Figure 2.1: A basic description of NRF with levels drawn for ^{238}U.

2.1 Nuclear Resonance Fluorescence

Nuclear resonance fluorescence (NRF) is the incoherent absorption and emission of γ rays from a nucleus. In the NRF process, an incident γ ray of energy E_x excites the nucleus into a higher energy state, typically populating a ΔJ=1 level (a ΔJ=2 level is much less probable). Afterward, the nucleus deexcites and if $E_x < S_n$, signature γ rays are emitted, populating the ground state or lower-lying excited states (see Fig. 2.1). Since the momentum transfer associated with NRF is small, dipole (L=1) excitations are highly favored over quadrupole (L=2) ones, making it a good probe for studying $M1$ and $E1$ excitations in nuclei.

There are three NRF detection methods: scattering, transmission, and absorption. Fig. 2.2 shows the differences between these detection methods. The basic physical process of NRF is the same regardless of the detection method. An example of an NRF spectra of ^{232}Th produced by the scattering detection method is shown in Fig. 2.3. The cross section for resonance fluorescence of a γ ray as the nucleus transitions from an excited state to the

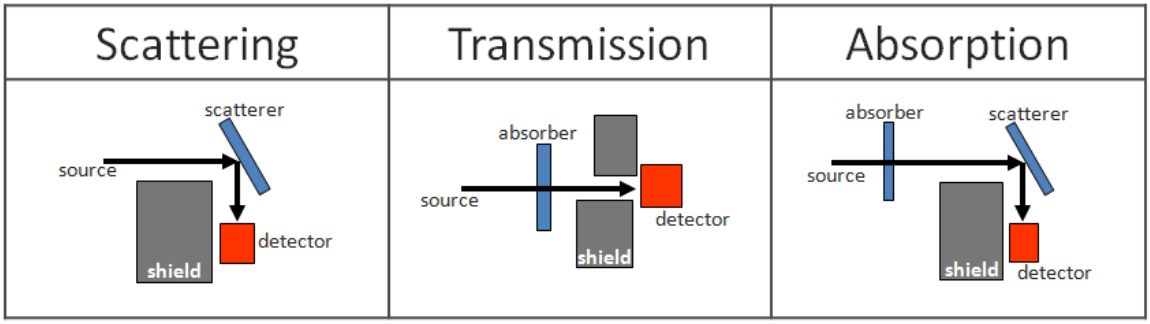

Figure 2.2: A schematic of the different NRF detection methods.

ground state [13] is

$$\sigma_{NRF}(E) = \frac{\pi \lambda\!\!\!^{-2} g}{2} \frac{\Gamma^2}{(E - E_r)^2 + \frac{1}{4}\Gamma^2} \quad , \tag{2.1}$$

where E_r is the resonance energy and $\lambda\!\!\!^{-}$ is the Compton wavelength. The statistical factor g depends on the spins of the excited state J_x and the spin of the ground state J_0,

$$g = \frac{2J_x + 1}{2J_0 + 1} \quad , \tag{2.2}$$

and the total width Γ is defined as,

$$\Gamma = \Sigma_i \Gamma_i = \Gamma_0 + \Gamma_1 + \ldots + \Gamma_n \quad , \tag{2.3}$$

where Γ_n is the n^{th} partial width for the decay from the n^{th} level. Generalizing Eq.(2.1) to deexcitations other than those proceeding exclusively to the ground state, the cross section of a deexcitation to the i^{th} state is

$$\sigma_i(E) = \frac{\pi \lambda\!\!\!^{-2} g}{2} \frac{\Gamma_0 \Gamma_i}{(E - E_r)^2 + \frac{1}{4}\Gamma^2} \quad . \tag{2.4}$$

Summing over all possible values of i for a given nucleus, the resonance absorption cross section of γ rays with energy E is

$$\sigma_{abs}(E) = \frac{\pi\lambda^2 g}{2} \frac{\Gamma_0 \Gamma}{(E - E_r)^2 + \frac{1}{4}\Gamma^2} \quad . \tag{2.5}$$

Additional spectroscopic information is obtained with the use of polarized beams as well as a properly oriented detector setup (see Chapter 5 for details). The difference between counting rates, for the horizontal and the vertical detector orientations, for both individual excitations and for the continuum, is defined as the azimuthal asymmetry A_{HV}. This asymmetry can be used to distinguish the spin and the parity for an observed state. To quantify A_{HV}, it is the degree of polarization $P(E_\gamma)$ of the incoming photon beam multiplied by the analyzing power Σ such that [15],

$$A_{HV} = P(E_\gamma) \cdot \Sigma = \frac{I_\perp - I_\parallel}{I_\perp + I_\parallel} = 1 \cdot \frac{W(90°, 90°) - W(90°, 0°)}{W(90°, 90°) + W(90°, 0°)} = \left\{ \begin{array}{l} +1 \text{ for } M1 \\ \\ -1 \text{ for } E1 \end{array} \right\} \quad , \tag{2.6}$$

where $I_\parallel$ ($I_\perp$) are the integrated cross sections I_s in the horizontal (vertical) detectors. For a point-sized detector and target as well as linearly-polarized γ rays, a pure $M1$ transition would have an $A_{HV} = 1$ and a pure $E1$ transition would have an $A_{HV} = -1$. For real detectors with finite geometry, the observed range is -1 < A_{HV} <1. The angular distribution for polarized γ rays, $W(\theta, \phi)$, is defined as follows [15]:

$$W(\theta, \phi) = W(\theta) + (\pm)_{L'_1} \sum_{\lambda=2,4} B'_\lambda(\gamma_1) A_\lambda(\gamma_2) P^{(2)}_\nu(\cos\theta) \cos 2\phi \quad , \tag{2.7}$$

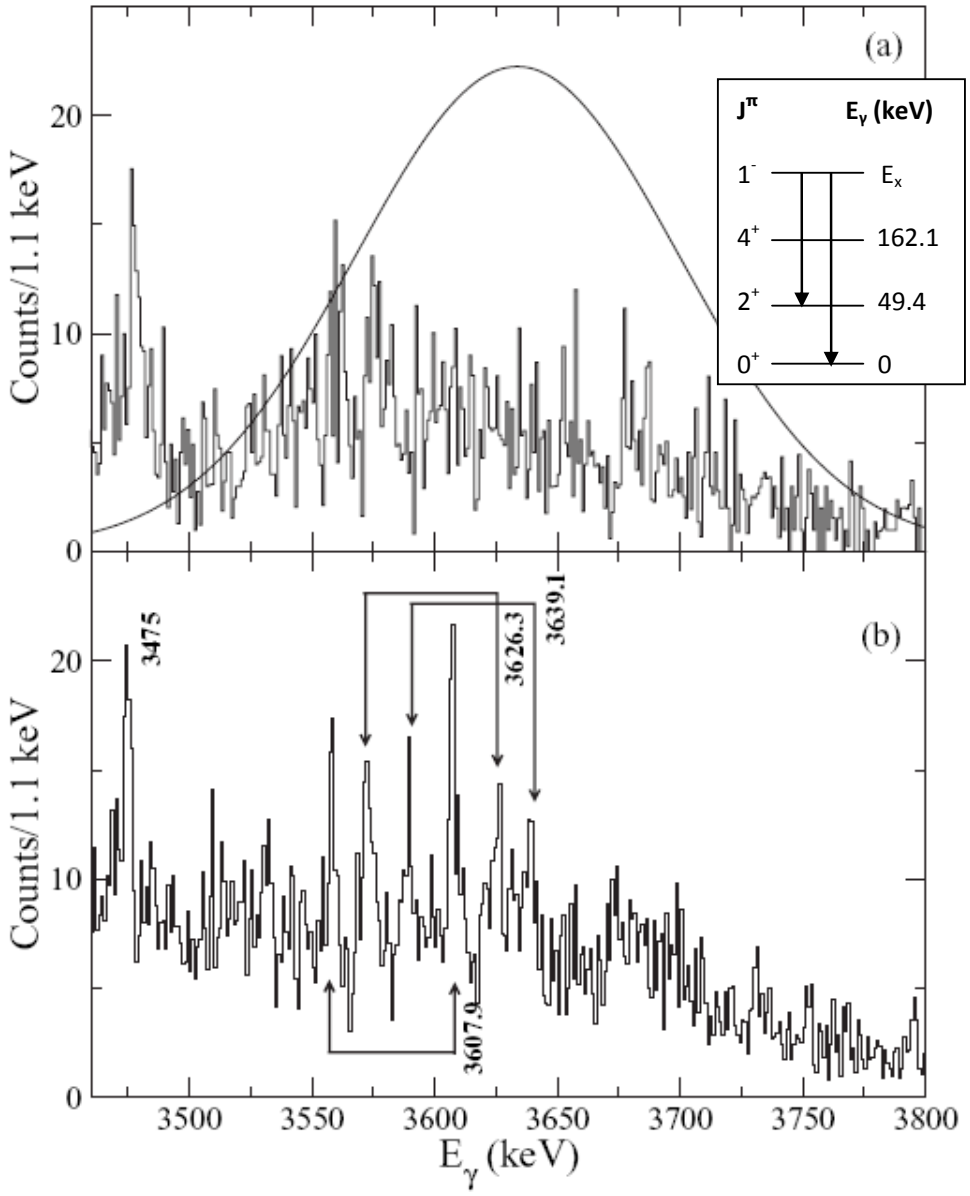

Figure 2.3: NRF spectra in the horizontal (a) and vertical (b) detectors from a ^{232}Th target using $E_\gamma = 3.6$ MeV. The line in (a) shows the energy distribution of the photon flux in arbitrary units. The brackets in (b) connect the ground-state transitions from the $J^\pi = 1^-$ levels with their corresponding transitions to the 2^+ state, separated by 49 keV. The peak at 3475 keV is a background line due to the activity in the target. Level diagram including the lowest levels of ^{232}Th is also provided in the inset of (a). Reproduced from Ref. [14].

where θ is the azimuthal angle measured from the scattering plane, ϕ is the polar angle of the outgoing radiation with respect to the linearly-polarized beam (downstream is $+\hat{z}$ axis), and $W(\theta)$ is angular distribution for an unpolarized photon beam [15],

$$W(\theta) = \sum_{\lambda_{\text{even}}} B_\lambda(\gamma_1) A_\lambda(\gamma_2) P_\lambda^{(2)}(\cos\theta) \ , \tag{2.8}$$

and the $(\pm)_{L_1'}$ corresponds to $E1$ (+1) and $M1$ (-1) transitions. The quantity $P_\lambda^{(2)}(\cos\theta)$ refers to a second-order Legendre polynomial, reparameterized in terms of angles. Fig. 2.4 shows a schematic of the angular distributions of γ rays for magnetic dipole, electric dipole and quadrupole radiation with designations for the beam direction and the polarization plane. The angular distribution of γ rays from a nucleus is a function of the angle between the nuclear spin axis and the direction of emission from the nucleus. This correlation between two γ rays, where one is absorbed and then one is subsequently emitted from a nucleus, is dependent on the spin of the excited state of the nucleus, the type of emitted radiation, and the angular momentum carried away by it. The coefficients in $W(\theta, \phi)$ quantitatively describe this physical information.

The expansion of these coefficients are defined in terms of the polarization coefficients k_λ and the Ferentz-Rosenzweig coefficients [15]:

$$B'_\lambda(\gamma_1) = \left(\frac{1}{1+\delta_1^2}\right)\left\{-k_\lambda(L_1L_1)F_\lambda(L_1L_1J_0J) + 2\delta_1 k_\lambda(L_1L_1')F_\lambda(L_1L_1'J_0J) + \delta_1^2 k_\lambda(L_1'L_1')F_\lambda(L_1'L_1'J_0J)\right\} \tag{2.9}$$

$$A_\lambda(\gamma_2) = \left(\frac{1}{1+\delta_2^2}\right)\left\{-k_\lambda(L_2L_2)F_\lambda(L_2L_2J_fJ) + 2\delta_2 k_\lambda(L_2L_2')F_\lambda(L_2L_2'J_fJ) + \delta_1^2 k_\lambda(L_2'L_2')F_\lambda(L_2'L_2'J_fJ)\right\} \ . \tag{2.10}$$

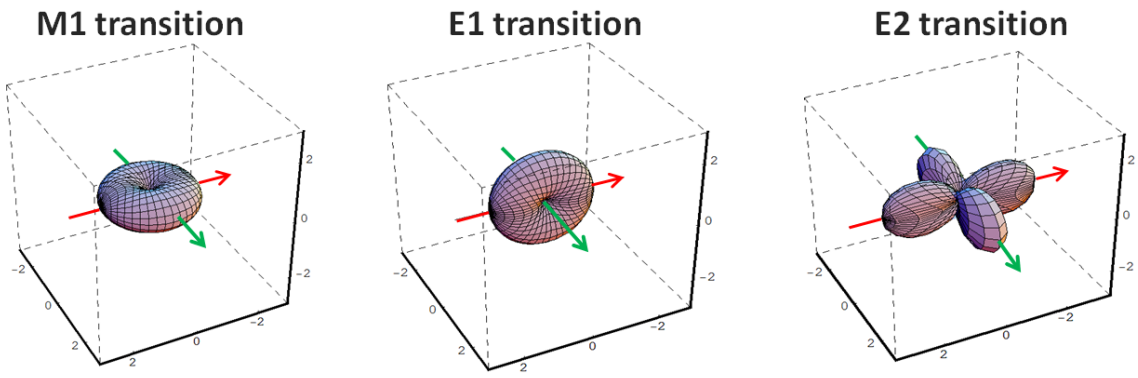

Figure 2.4: Schematic of the angular distributions of γ rays for magnetic dipole ($M1$), electric dipole ($E1$), and electric quadrupole ($E1$) radiation. Red arrows designate the beam direction while the green arrows indicate the plane of polarization.

These coefficients describe a continuous function of the mixing ratio δ with respect to the emission of L' radiation to that of the incoming L radiation. The Ferentz-Rosenzweig coefficients are defined as (with $L' = L + 1$) [16]

$$F_\lambda(LL'J_1J_2) = (-1)^{J_1+J_2+1}\sqrt{(2L+1)(2L'+1)(2\lambda+1)(2J_2+1)}\cdot\begin{pmatrix} L & L' & \lambda \\ 1 & -1 & 0 \end{pmatrix}\cdot\begin{Bmatrix} J_2 & J_2 & \lambda \\ L & L' & J_1 \end{Bmatrix}. \tag{2.11}$$

Finally, using the described method above, the angular correlation factor can quantified to correct the integrated cross section for a particular γ-ray distribution observed. These values are tabulated in Table 2.1 for the horizontal, vertical, and backward detector orientations (See Chapter 5 for details on the detector orientations).

2.1.1 Integrated Cross Section and Reduced Width

The Doppler effect is an important consideration for NRF measurements since the spectral lines appear wider than they actually are. This is due to the thermal motion of the nuclei.

Each nucleus moves with a velocity v, thereby shifting the rest energy E to E'

$$E' = \frac{E\,(1 + v/c)}{\sqrt{1 - (v/c)^2}} \approx E\,(1 + v/c) \quad . \tag{2.12}$$

If the velocities are well-described by a Maxwellian distribution function, then the likelihood of a nuclei having a component of v parallel to the source direction is

$$w(v)\mathrm{d}v = \sqrt{\frac{M_n}{2\pi kT}} e^{-\frac{M_n v^2}{2kT}} \mathrm{d}v \quad , \tag{2.13}$$

where M_n is the nuclear mass, k is Boltzmann's constant, and T is the absolute temperature of the material. If Eq. (2.12) is used to change the integration variable of Eq. (2.13), the distribution of energies is of the following form:

$$w(E')\mathrm{d}E' = \left(1/\Delta\pi^{1/2}\right) e^{-\left(\frac{E'-E}{\Delta}\right)^2} \quad , \tag{2.14}$$

where the Doppler width $\Delta = (E/c)\,(2kT/M_n)^{1/2} = aE$. It is known that the effective temperature T_{eff} of the solid target is higher than the actual temperature T [17]. Thus, a

Table 2.1: Angular correlations for each of the different detector orientations.

		Horizontal	Vertical	Backward
$M1$	$0^+ \to 1^+ \to 0^+$	1.45	0.08	1.50
	$0^+ \to 1^+ \to 2^+$	1.10	0.90	1.05
$E1$	$0^+ \to 1^- \to 0^+$	0.09	1.45	0.88
	$0^+ \to 1^- \to 2^+$	0.90	1.10	0.96
$E2$	$0^+ \to 2^+ \to 0^+$	2.50	0.00	1.47
	$0^+ \to 2^- \to 0^+$	0.00	2.50	0.08

correction to T must be made to find T_{eff},

$$T_{eff}/T = 3\left(T/\Theta_D\right)^3 \int_0^{\Theta_D/T} t^3 \left(\frac{1}{e^t - 1} + \frac{1}{2}\right) \mathrm{d}t \ , \tag{2.15}$$

where Θ_D is the Debye temperature. Averaging Eq. (2.1) over all possible values of E'

$$\sigma_{NRF}(E,t) = \int \sigma_{NRF}(E')w(E')\mathrm{d}E' = \sigma_{abs}^{max}\Psi(x,t) \ . \tag{2.16}$$

The maximum value of $\sigma_{abs}(E)$ is found by setting E equal to E_r in Eq. (2.5),

$$\sigma_{abs}^{max} = \sigma_{abs}(E = E_r) = 2\pi\lambda\!\!\!^{-2} g \frac{\Gamma_0}{\Gamma} \ . \tag{2.17}$$

If a large t ($t \gg x$) is present, $\Psi(x,t)$ takes on the the form,

$$\Psi(x,t) = \frac{1}{2\left(\pi t\right)^{1/2}} \int_{-\infty}^{\infty} \frac{e^{-(x-y)^2/4t}}{1+y^2} \mathrm{d}y = \frac{1}{2}\sqrt{\frac{\pi}{t}} e^{-x^2/4t} \ , \tag{2.18}$$

where $t = \left(\Delta/\Gamma\right)^2$ and $x = 2\left(E - E_r\right)/\Gamma$ and $y = 2\left(E' - E_r\right)/\Gamma$. The final Doppler form of the cross section is

$$\sigma_D(E) = \sigma_0^{max}\Psi(x,t) = \pi^{3/2}\lambda\!\!\!^{-2} g \frac{\Gamma_0}{\Delta} e^{-\left(\frac{E-E_r}{\Delta}\right)^2} \ , \tag{2.19}$$

where

$$\int \sigma_D(E)\mathrm{d}E = \left(\pi\lambda\!\!\!^{-}\right)^2 g\Gamma_0 \ . \tag{2.20}$$

Furthermore, if the elastic photon-scattering cross section includes thermal motion of the nuclei, it will also have a Doppler form. Thus, the differential scattering cross section, in terms of $\sigma_{abs}(E)$ and the angular correlation function $W(\theta)$, is as follows [18],

$$\frac{\mathrm{d}\sigma_{\gamma\gamma}i}{\mathrm{d}\Omega} = \frac{W(\theta)}{4\pi}\frac{\Gamma_i}{\Gamma}\sigma_{abs}(E) \ . \tag{2.21}$$

From Eq. (2.20), the cross section $\sigma_{\gamma\gamma}(E)$ can be written with a Doppler broadening as well,

$$\sigma_{\gamma\gamma}(E) = \sigma_0^{max} b\Psi(x,t) = \pi^{3/2}\lambda\!\!\!^{-2} g\frac{\Gamma_0^2}{\Gamma}\frac{1}{\Delta^2}e^{-\left(\frac{E-E_r}{\Delta}\right)^2} \ , \tag{2.22}$$

where b is the branching ratio, Γ_0/Γ. The integrated cross section is

$$\int \sigma_{\gamma\gamma}(E)\mathrm{d}E = I_s = (\pi\lambda\!\!\!^{-})^2\, g\frac{\Gamma_0^2}{\Gamma} \ . \tag{2.23}$$

The quantity I_s can be written in terms of experimental observables giving the following form,

$$I_s = \int \sigma_{\gamma\gamma}(E)\mathrm{d}E = \frac{N/t}{n_{tar}\epsilon(E)W(\theta,\phi)\Phi(E)} \ , \tag{2.24}$$

where N is the dead-time-corrected number of counts in the full energy peak in time t, $\epsilon(E)$ is the detector efficiency, and $\Phi(E)$ is the flux of γ rays interacting with the front of the target. The number of target nuclei per unit area n_{tar} is defined as

$$n_{tar} = \left(\frac{d\rho}{M_n}N_A\right)\frac{\chi_i}{100} \ , \tag{2.25}$$

where d is the target thickness, ρ is the target density, M_n is the molecular mass of the target, N_A is Avogadro's number, and χ is the fractional percentile abundance for isotope i within the target.

Using Eqs. (2.17), (2.21), and (2.23), as well as only considering the ground state, after some rearrangement, the reduced ground-state width reduces to

$$\frac{\Gamma_0^2}{\Gamma} = \frac{I_s}{g}\left(\frac{E_\gamma}{\pi\hbar c}\right)^2 \quad , \tag{2.26}$$

where Γ is the total level width, Γ_0 is the ground-state width, and E_γ is the energy of the deexciting γ ray.

2.1.2 Branching Ratios and Transition Probabilities

For even-even actinides, no transitions from the excited state to any states other than the first excited 2^+ state and the ground state are observed. The involvement of low-momentum transfers in the NRF process provides the assumption that Γ is equal to $\Gamma_0 + \Gamma_1$, where Γ_1 denotes the width of the transition to the first excited state. In particular, the energy of a transition to the first excited state in ^{238}U is equal to the beam energy E_γ-45 keV with 45 keV being the energy of the first excited state. The widths of Γ_0 and Γ_1 can be easily observed through experiments. Thus, the experimental branching ratio R_{exp} can be defined as

$$R_{exp} = \frac{\Gamma_1}{\Gamma_0}\left(\frac{E_0}{E_1}\right)^3 \quad , \tag{2.27}$$

where E_1 (E_0) is the excitation energy of a transition to the 2^+ (ground) state. It is also defined through experimental parameters such that

$$R_{exp} = \frac{N_1}{N_0} \frac{E^3_{1\to0} W(\theta)_{0\to1\to0} \epsilon(E_0)}{E^3_{1\to2} W(\theta)_{0\to1\to2} \epsilon(E_1)} \quad . \tag{2.28}$$

The Alaga rules [15, 19] show for a $J^\pi = 1^\pm$ state that R is the ratio of the reduced transition probabilities B of transitions to the first excited state and to the ground state:

$$R = \frac{B(1^\pi \to 2^+)}{B(1^\pi \to 0^+)} = \left| \frac{\sqrt{2J_1+1} < J_1, K_1, L, K-K_1 | J, K >}{\sqrt{2J_0+1} < J_0, K_0, L, K-K_0 | J, K >} \right|^2 = \begin{Bmatrix} 0.5 \text{ for K=1} \\ 2.0 \text{ for K=0} \end{Bmatrix} \quad , \tag{2.29}$$

where π is the parity of the state. Note that angular momentum J is no longer a good quantum number; only its projection on the symmetry axis, K (the rotational quantum number), is viable. For $J^\pi = 1^\pm$ states, only transitions from states with $K = 0$ and $K = 1$ are allowed. Values in between 0.5 and 2.0 can indicate either K-mixing or a violation of the Alaga rules. From R_{exp}, the branching ratio b can be deduced following the prior assumption that Γ is equal to $\Gamma_0 + \Gamma_1$,

$$b = \frac{\Gamma_0}{\Gamma} = \frac{1}{1 + R_{exp} \left(\frac{E_1}{E_0} \right)^3} \quad . \tag{2.30}$$

Once b is known, Γ_0 can be calculated such that,

$$\Gamma_0 = \frac{1}{b} \frac{I_s}{g} \left(\frac{E_\gamma}{\pi \hbar c} \right)^2 \quad . \tag{2.31}$$

Once Γ_0 is known, the reduced transition probabilities $B(\Pi L, E) \uparrow$ where Π is either E for electric radiation or M for magnetic radiation, can be defined as [20]

$$B(\Pi L, E) \uparrow = g\Gamma_0 \sum_{\Pi L=1}^{\infty} \frac{(\lambda\!\!\!^{-})^{2L+1}}{8\pi(L+1)} L\,[(2L+1)!!]^2 \quad . \tag{2.32}$$

The most probable states observed in NRF experiments on a target of an even-even nucleus are those with $J^\pi=1^\pm$. As such, deexciting transitions to states with either $J^\pi=0^+$ or 2^+ are observed exclusively. As described above, in many NRF experiments involving deformed, even-even nuclei, only transitions to the ground state and to the first excited state are observed. Since no states with $J^\pi=2^+$ were observed in the current work (see Chapter 6), the reduced transition probabilities for dipole strengths are the only ones of consequence. For even-even nuclei ($J_0 = 0$) and $L = 1$, these γ-ray strengths can be found through

$$B(\Pi 1, E) \uparrow = (3!!)^2 \frac{3}{16\pi} \lambda\!\!\!^{-3} \Gamma_0 \quad . \tag{2.33}$$

Numerically, Eq. (2.33) is evaluated to be (with Γ_0 in meV and E in MeV)

$$B(E1, E) \uparrow = 2.866 \times 10^{-3} \frac{\Gamma_0}{E^3} \quad [e^2 fm^2] \tag{2.34}$$

for electric dipole transitions and

$$B(M1, E) \uparrow = 0.2598 \frac{\Gamma_0}{E^3} \quad [\mu_N^2] \tag{2.35}$$

for magnetic dipole transitions. The ratio of $B(\Pi L, E) \uparrow$ to $B(\Pi L, E) \downarrow$ is g, where the

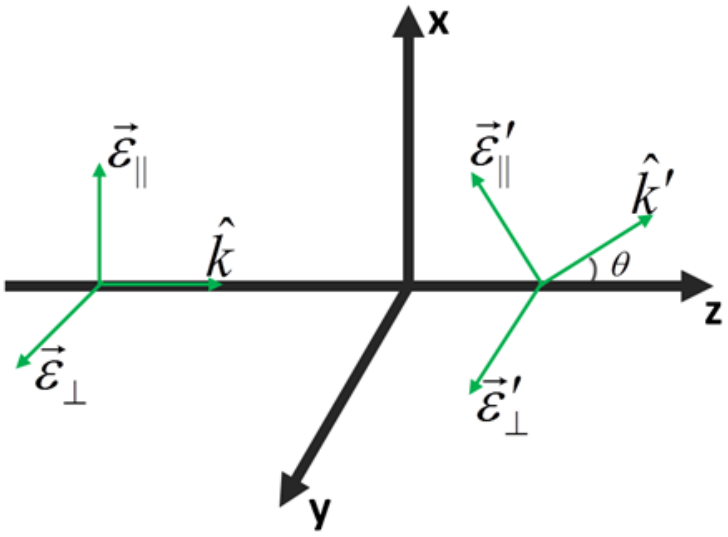

Figure 2.5: Schematic of the polarization of the γ rays. Modified from Ref. [21].

arrow denotes the interaction of the γ ray with the nucleus, whether through absorption ($\uparrow$) or through emission ($\downarrow$). The mean excitation energy ω_{M1} can be deduced experimentally through

$$\omega_{\Pi 1} = \frac{\sum_i B(\Pi 1, E)_i E_i}{\sum_{i=1} B(\Pi 1, E)_i} \quad , \tag{2.36}$$

where $B(\Pi 1, E)_i$ is the i^{th} transition probability and E_i is the i^{th} excitation energy.

2.2 Coherent Scattering

The polarization of the incident photon must be mentioned before discussing the coherent-scattering processes in any kind of detail. Let $\hat{k}$ be the momentum vector of the incident photon in the direction of the $\hat{z}$-axis (see Fig. 2.5). This photon can have linear-polarization vectors $\vec{e_{\parallel}}$ and $\vec{e_{\perp}}$, each perpendicular to $\hat{k}$. Since an incident photon ($(\vec{e})$) may also be unpolarized or circularly-polarized, combinations of $\vec{e_{\parallel}}$ and $\vec{e_{\perp}}$ can be made to form unpolarized

or helical polarization states. For the rest of this dissertation, the incident photon will have linear polarization of $\vec{e_{\|}}$ only.

The scattered photon of momentum vector $\hat{k}'$ is ejected into a new frame (the "scattering" plane) which is rotated by θ and ϕ from the original frame of the incident photon. This scattered photon ($\vec{e}'$) can have either parallel polarization ($\vec{e_{\|}}'$) within this scattering plane or perpendicular polarization ($\vec{e_{\perp}}'$) normal to the scattering plane. In general, any of these coherent cross sections σ_{coh} can be written in terms of an amplitude, A, such that,

$$\frac{\mathrm{d}\sigma_{coh}}{\mathrm{d}\Omega} = |A|^2 = \frac{1}{2}\left(|A_{\|}|^2 + |A_{\perp}|^2\right) \ , \tag{2.37}$$

where A is further reduced to its parallel and perpendicular parts. These components indicate the possible final paths of the scattered γ rays in reference to the scattering plane of the incident γ rays.

Note: The following coherent scattering processes are mostly insignificant in the energy ranges studied by this dissertation, yet a thorough examination of all possible scattering incidents within the detector need to be accounted. The primary source of coherently scattered γ rays in the energy range of 2 MeV¡E_γ¡S_n is Delbrück scattering as seen in Table 2.2.

2.2.1 Nuclear Thomson Scattering

Thomson scattering is the coherent process by which γ rays are elastically scattered from charged particles. The electric field of the incident γ ray accelerates the particle, causing it to emit γ rays of the same energy as the incident γ rays, and so, it is scattered. In

nuclear Thomson scattering, the nucleus is used as the charged-particle target from which the γ rays scatter. The Thomson amplitude T is equal to [21]

$$T = r_0 \frac{Z^2 m}{M_n} \, \vec{e} \cdot \vec{e}', \tag{2.38}$$

where r_0 is the electron radius, Z is the proton number, m is the electron rest mass, and M_n is the nuclear mass. The dot product $\vec{e} \cdot \vec{e}'$ demands that $\vec{e}$ and $\vec{e}'$ must be in the same plane otherwise it is zero. For $\vec{e} = e_{\parallel}$, only the choice of $e'_{\parallel}$ will produce a non-zero result of $\sin\theta \cos\phi$. Therefore, T can be written in its component form where

$$T_{\parallel} = r_0 \frac{Z^2 m}{M} \sin\theta \, \cos\phi \tag{2.39}$$

and

$$T_{\perp} = r_0 \frac{Z^2 m}{M} \quad . \tag{2.40}$$

The nuclear Thomson cross section for the present experiment's solid-angle geometry is as follows: 5.5μb for the horizontal detectors, 0.2μb for the vertical detectors, and zero for the backward detectors. See Chapter 5 for details on detector placement and orientation.

2.2.2 Rayleigh Scattering

Rayleigh scattering is the coherent process by which γ rays are elastically scattered from atoms or molecules. In nuclear Rayleigh scattering, this is redefined as the process by which γ rays are scattered by bound electrons which leave the target unchanged after

scattering has occurred. The Rayleigh amplitude R is [22]

$$R = r_0 \frac{1}{2} F_n(q)\, \vec{e} \cdot \vec{e}\,' \ , \tag{2.41}$$

where $F_n(q)$ is the form factor depending on the momentum transfer $q = 2|\hat{k}\,'|sin\theta/2$ and $\hat{k}\,'$ is the momentum vector of the outgoing γ ray. Writing R in component form gives

$$R_{\parallel} = r_0 \frac{1}{2} F_n(q) \sin\theta \, \cos\phi \tag{2.42}$$

and

$$R_{\perp} = r_0 \frac{1}{2} F_n(q) \ . \tag{2.43}$$

The form for $F_n(q)$ can be found for nuclei of $1< Z <92$ in the RTAB database [23]. The spherically-symmetric charge density $\rho(\vec{r})$ version of $F_n(q)$ can be found from first principles [24] to be

$$F_n(q) = \int \rho(\vec{r})\, e^{i\vec{q}\cdot\vec{r}} \mathrm{d}\vec{r} \ . \tag{2.44}$$

A modification was made to this in order to include corrections for electron binding ϵ and the electrostatic potential $V(r)$. This modified form factor $G_n(q)$, including the definition above of q, is [23]

$$G_n(q) = \sum_{electrons} 4\pi \int_0^{\infty} \rho(r) \left(\frac{\sin(qr)}{qr} \frac{1}{1 - \frac{\epsilon}{mc^2} - V(r)} \right) r^2 \mathrm{d}r \ , \tag{2.45}$$

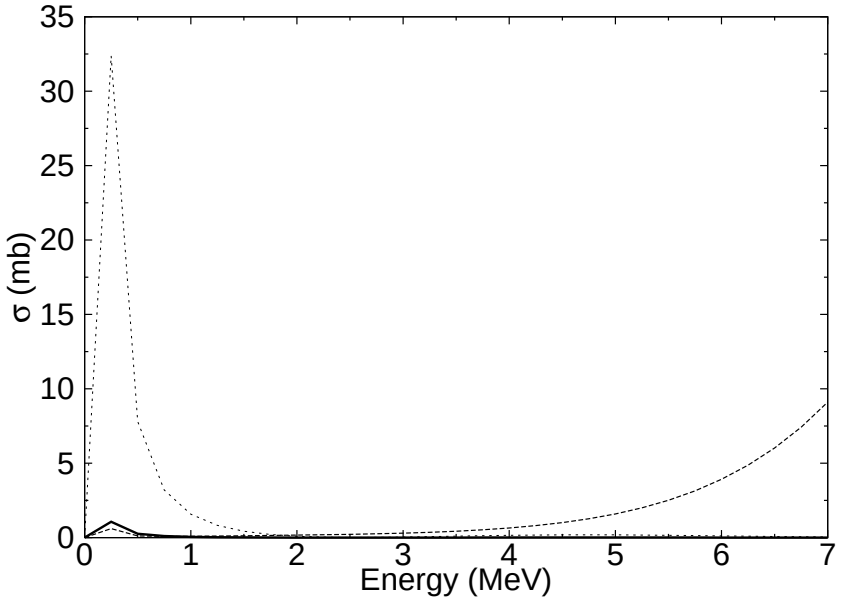

Figure 2.6: Nuclear Rayleigh cross section between 0-7 MeV for γ rays scattering within the parallel polarization plane (dotted curve), the perpendicular polarization plane (solid curve), or the parallel polarization plane at a backward-angle (dashed curve). Experimental solid-angle geometry is detailed in Chapter 5.

and can be substituted for $F_n(q)$ into Eq. (2.41). The nuclear Rayleigh cross section is shown for the summed horizontal, summed vertical and summed backward-angled detectors in Fig. 2.6. Solid-angle geometry is detailed in Chapter 5.

2.2.3 Delbrück Scattering

Delbrück scattering is the process by which γ rays are elastically scattered from the Coulomb field of heavy nuclei. However, in the presence of an electromagnetic field where the photons propagate in the direction perpendicular to the momentum $\hat{k}$, it can be an inelastic process [25]. Only the elastic case shall be considered here. The Delbrück amplitude D will take the following form [21]:

$$D = (\alpha Z)^2 r_0 \left[f(\vec{e} \cdot \vec{e}^{\,\prime *}) + g(\vec{e} \cdot \hat{k}^{\,\prime})(\vec{e}^{\,\prime *} \cdot \hat{k}) \right] \ , \tag{2.46}$$

where α is the fine structure constant and $\hat{k}$ is the momentum vector of the incoming γ ray. The "*" denotes complex conjugate. This amplitude can be provided in components such that

$$D_{\parallel} = r_0 f \cos\theta - g \sin^2\theta \tag{2.47}$$

and

$$D_{\perp} = r_0 f \quad . \tag{2.48}$$

The functions f and g, in units of $\left(32 \times 72m^2\right)^{-1}$, can be approximated by [26]

$$f = E_{\gamma}^2 (59 + 14\cos\theta) \tag{2.49}$$

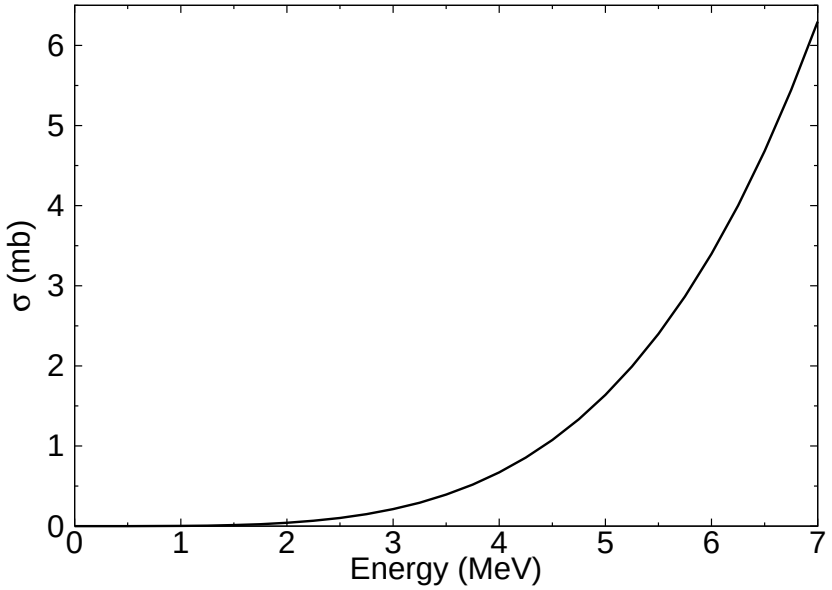

Figure 2.7: The Delbrück cross section between 0-7 MeV for γ rays scattering within the parallel polarization plane (dotted curve). The perpendicular polarization plane (solid curve) matches identically with the parallel polarization plane. Experimental solid-angle geometry is detailed in Chapter 5.

and

$$g = -14E_\gamma^2 \ . \tag{2.50}$$

The Delbrück cross section is shown for the summed horizontal detectors in Fig. 2.7 which is identical to the cross section for the summed vertical detectors. The cross section for the backward-angled detectors is zero.

2.2.4 Nuclear Resonance Scattering

Nuclear resonance scattering refers to the coherent process of γ rays elastically scattering from a nucleus as opposed to the NRF process which is considered an incoherent process. However, there is an additional incoherent contribution to the elastic scattering cross section which arises from nuclear scattering of γ rays from the GDR. It is relatively insignificant below 7 MeV [27] and will not be discussed. Therefore, the coherent part of the nuclear resonance amplitude N [27] is then

$$N = \frac{E^2}{4\hbar c r_0} \sum_{\nu=1}^{2} \sigma_\nu \Gamma_\nu \frac{E_\nu^2 - E^2 + iE\Gamma_\nu}{\left(E_\nu^2 - E^2\right)^2 + E^2\Gamma_\nu^2} \, \vec{e} \cdot \vec{e}' \ , \tag{2.51}$$

where ν stands for the number of resonances in the GDR (one for spherical and two for deformed). Parameters of the GDR are as follows: the energy, E_ν, the width, Γ_ν, and the amplitude σ_ν. The term $iE\Gamma_\nu$ is only significant above the neutron separation energy. Finally breaking down N into components produces

$$N_\parallel = \frac{E^2}{4\hbar c r_0} \sum_{\nu=1}^{2} \sigma_\nu \Gamma_\nu \frac{E_\nu^2 - E^2 + iE\Gamma_\nu}{\left(E_\nu^2 - E^2\right)^2 + E^2\Gamma_\nu^2} \, \sin\theta \, \cos\phi \tag{2.52}$$

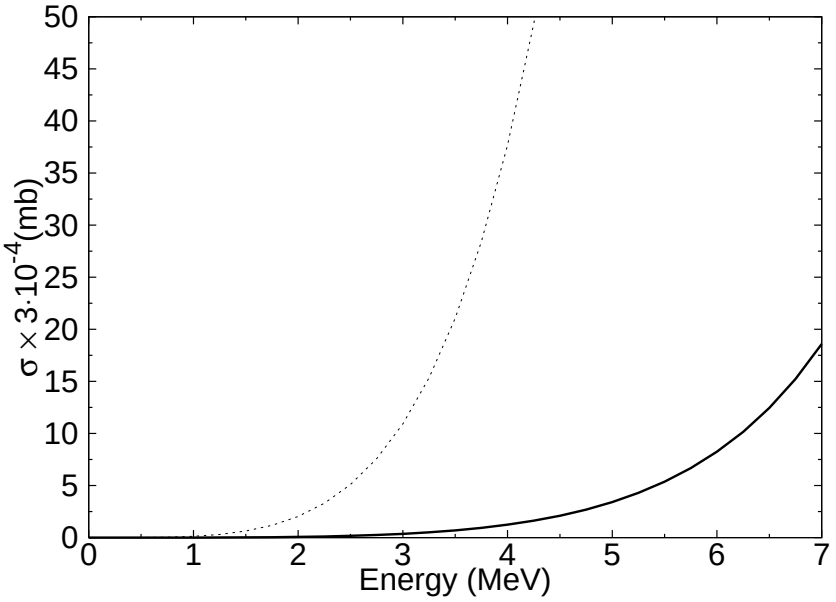

Figure 2.8: Nuclear resonance cross section between 0-7 MeV for γ rays scattering within the parallel polarization plane (dotted curve) and the perpendicular polarization plane (solid curve).

and

$$N_{\perp} = \frac{E^2}{4\hbar c r_0} \sum_{\nu=1}^{2} \sigma_\nu \Gamma_\nu \frac{E_\nu^2 - E^2 + iE\Gamma_\nu}{(E_\nu^2 - E^2)^2 + E^2\Gamma_\nu^2} \quad . \tag{2.53}$$

The nuclear resonance cross section is shown for the summed horizontal and summed vertical detector orientations in Fig. 2.8. The cross section for the horizontal detectors is about a factor of 30 larger than the one for the vertical detectors. For the summed backward-angled detectors, the cross section is zero.

2.2.5 Coherent Scattering Summary

The total coherent cross section is made up of the superposition of each of the four amplitudes T, R, D, and N, such that,

$$\frac{d\sigma_{coh}}{d\Omega} = |-T - R + D + N|^2 \quad . \tag{2.54}$$

Table 2.2: Coherent scattering contributions (listed in percentages) to the total photon interaction cross section at selected beam energies in the range between 2.0 and 6.2 MeV for the summed vertical detectors. The dominant contribution is from Delbrück scattering.

E (MeV)	T	R	D	N	Total Coherent	Total NRF
2.01	0.004	0.06	1	0	1	99
2.64	0.004	0.01	3	0	3	97
3.04	0.003	0.02	3	0	3	97
3.62	0.003	0.05	7	0	7	93
4.04	0.003	0.09	12	0.001	12	88
4.63	0.002	0.07	13	0.001	13	87
5.06	0.001	0.03	8	0.001	8	92
5.62	0.001	0.01	7	0.001	7	93
6.02	0.001	0.02	14	0.001	14	86
6.14	0.001	0.02	23	0.002	23	77

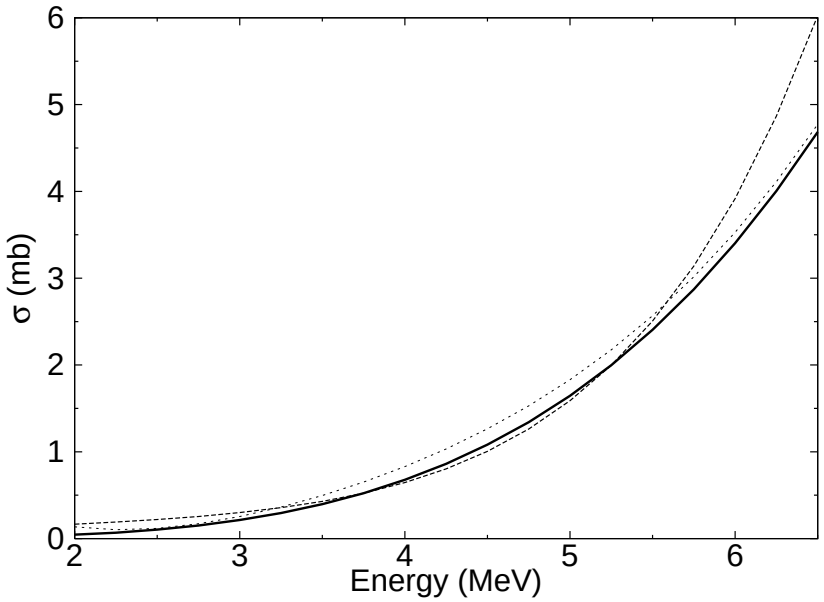

Figure 2.9: Total coherent-scattering cross section at energies between 2.0 and 6.2 MeV for γ rays scattering within the parallel polarization plane (dotted curve), the perpendicular polarization plane (solid curve), or the parallel polarization plane at a backward-angle (dashed curve).

This total coherent-scattering cross section is used in combination with the $E1$ γ-ray interaction cross section to find the total cross section in Section 7.3. Table 2.2 and Fig. 2.9 sum-

marize the contribution of each coherent-scattering process between 2.0 and 6.2 MeV. In this range, which is relevant to the present experiments, the overall contributing coherent-scattering process is Delbrück scattering.

2.3 Collective Excitations

The nucleus can be excited by a γ ray in various modes with the lowest multipoles for magnetic and electric radiation shown in Fig. 2.10. Through the NRF process in particular, photon interactions with nuclei will produce dipole excitations with the most probability since there is a low-momentum transfer involved. Furthermore, photons have a long wavelength in comparison to the size of the system under investigation (i.e. the nucleus); this choice of a photonic probe selectively excites dipole resonances only.

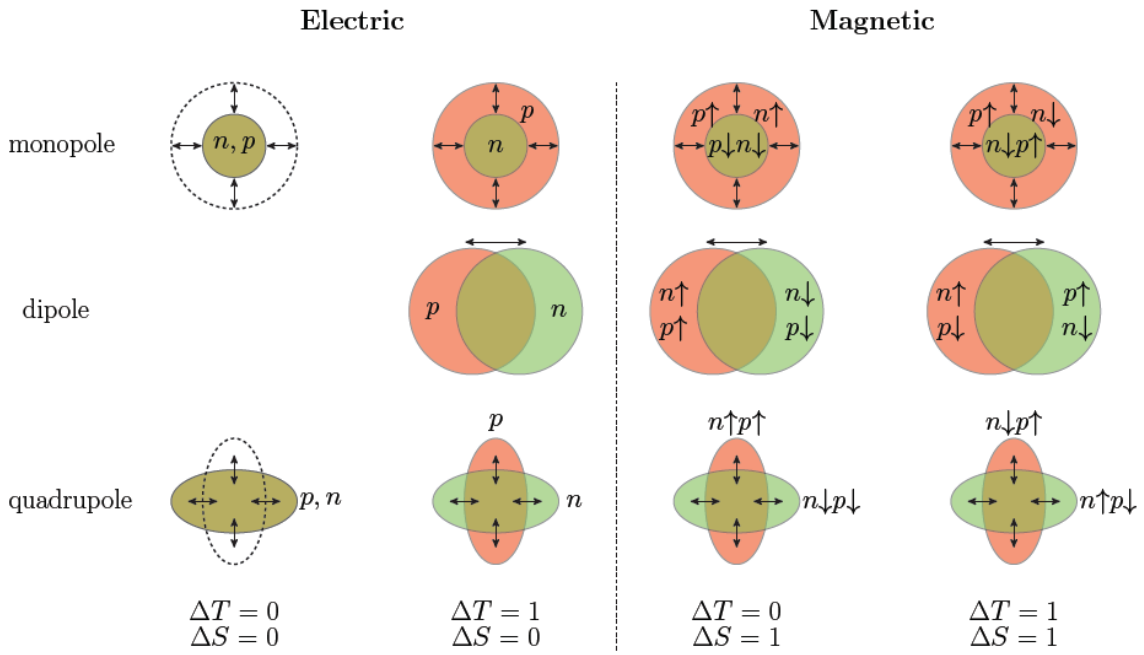

Figure 2.10: Nuclear excitations for which L≤2. Reproduced from Ref. [28].

Regardless, dipole excitations can characterize the collective structure of the excited nucleons [29] through various mechanisms such as the "scissors" mode, the spin-flip mode, pygmy dipole resonances (PDR), and giant dipole resonances (GDR). Theoretical calculations (see Chapter 3) suggest that substantial dipole strength should exist in the energy region between the "scissors" mode and the GDR from both magnetic ($M1$) and electric ($E1$) dipole excitations in neutron-rich, deformed nuclei [30, 31]. These calculations predict that, in general, the number of $M1$ states decreases as the excitation energy increases, while the number of $E1$ states increases with energy while approaching the GDR. Other mechanisms which can also propagate dipole excitations are octupole deformations and α-clusterings, as theorized by Iachello [32].

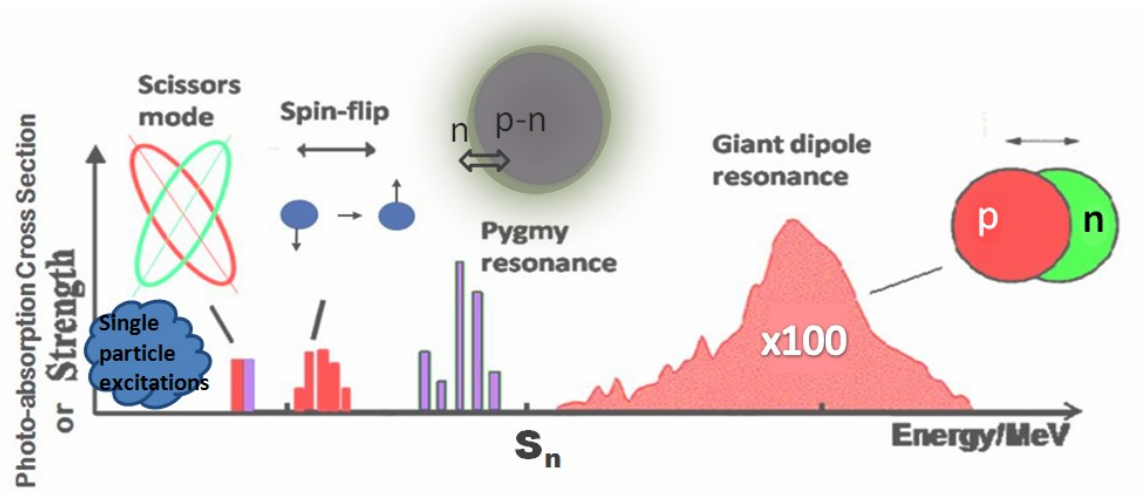

Figure 2.11: Most probable collective dipole excitations for a nucleus. Modified from Ref. [33].

In the following sections, $M1$ collective excitations including the scissors mode and the spin-flip mode as well as the $E1$ collective excitations including PDR, GDR, octupole, and α-scattering, will be described in detail. The landscape of the most probable collective

dipole excitations is shown in Fig. 2.11 as a function of excitation energy.

2.3.1 Magnetic Excitations

Collective $M1$ excitations are observed in highly-deformed nuclei, and are assigned to one of the following modes: an orbital scissors mode or a spin-flip mode. Schematics of the motions transcribed by a nucleus in order to emit magnetic radiation are shown in Fig. 2.12.

The $M1$ Scissors Mode

The orbital $M1$ "scissors" mode involves the motion of deformed bodies of protons and neutrons vibrating against each other [35] such that the generated motion from vibration is scissors-like, i.e. the $M1$ matrix element is proportional to the difference of $\vec{L}_p - \vec{L}_n$ where L is the orbital component of the total angular momentum. This is a low-lying $M1$ strength

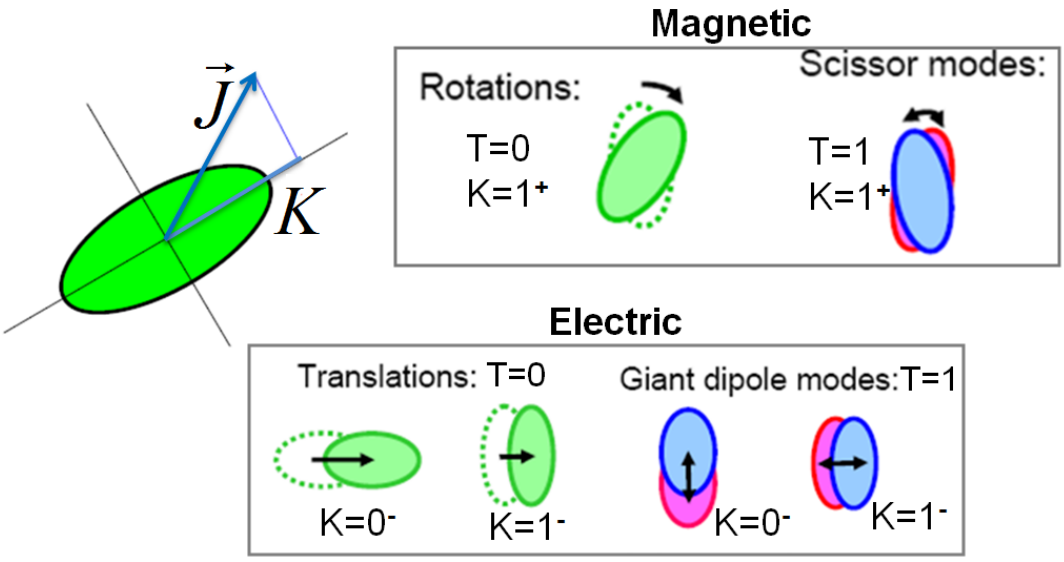

Figure 2.12: Dipole Excitations with their assigned K values for their isoscalar (T=0) and isovector (T=1) components. Reproduced from Ref. [34].

which exists primarily in deformed nuclei such that an increase in A, the mass number, will proportionally shift the $M1$ excitations down in energy by $61 \cdot \delta A^{-1/3}$ where δ is the ground-state quadrupole deformation parameter. Ground-state transition strength produced from the "scissors" mode is generally fragmented and concentrated in the energy region around 2-3 MeV, with a considerable dependence on deformation [36].

In previous $^{238}\mathrm{U}(\gamma, \gamma')$ experiments [1, 37], the scissors mode was observed to exist between 2.0-2.5 MeV and the summed $M1$ strength was measured to be $\Sigma B(M1) = 3.2(2)$ $\mu_{\mathrm{N}}{}^2$ with a mean excitation energy ω_{M1} of 2.3(2) MeV. This $\Sigma B(M1)$ is comparable to those determined for spherical and deformed rare-earth nuclei, whose scissors mode is shown to exist at energies between 2.4-3.7 MeV with ω_{M1} ~3.0 MeV and with $\Sigma B(M1)$ between 0.20(2)-3.7(6) $\mu_{\mathrm{N}}{}^2$, depending on the degree of deformation [38]. Enders *et al*. noted that ω_{M1} depended linearly on the square of the deformation parameter δ [38].

The $M1$ Spin-Flip Mode

The $M1$ spin-flip mode describes the change in spin for a collective number of nucleons and the subsequent motion of the spin-up nucleons oscillating against the spin-down nucleons whether it be through translations (isoscalar) or rotations (isovector). This mode is discussed within literature to a lesser extent than the scissors mode even though the spin-flip mode carries the majority of the $M1$ strength [3]. The spin-flip mode is $M1$ strength generally found at higher energies above the "scissors" mode.

The spin-flip mode has a "two peak" structure due to the separation of where the isoscalar and isovector parts of the strength lie. The isoscalar $B(M1)$ is proportional to $34A^{-1/3}$ whereas the isovector part is slightly higher, located at $44A^{-1/3}$. In some nuclei, the

two peak structure is less pronounced and only a weighted average of the strength proportional to $41A^{-1/3}$ is observed. See Fig. 4.8 for an illustration of this two-peak structure.

An inelastic proton-scattering experiment [39] estimated an upper limit for the $M1$ strength in ^{238}U to lie between 15-25 $\mu_N{}^2$ in the energy range of 4-10 MeV. $M1$ strength found at these energies are thought to be a part of the $M1$ spin-flip resonance [3]. However, investigations of this mode for actinide nuclei have been limited to measurements of the continuum only because of the higher density of states as excitation energy is increased. For comparison, $\Sigma B(M1)$ has been found in similarly deformed rare-earth nuclei to be between 10-15 $\mu_N{}^2$ in the energy range of 6-10 MeV [40].

2.3.2 Electric Excitations

Collective $E1$ excitations have been observed in both spherical and deformed nuclei alike. The majority of the total $E1$ strength in any given nucleus is produced by the giant dipole resonance (GDR) which corresponds to the large scale motion of all the protons collectively oscillating against all the neutrons in the nucleus [41]. It contains the resonant states above S_n, built by this coherent motion which involves many nucleons. The GDR has been observed in all stable nuclei between excitation energies E_x=820 MeV. A thorough investigation of the GDR in ^{238}U was completed by Caldwell *et al.* [42] (see Fig. 2.13). However, the strength produced from the GDR does not account for *all* of the observed strength in a given nuclei and other types of collective motions have been observed. These include the pygmy dipole resonance [43] as well as those caused by octupole deformation and by α-clustering [32]. Again, schematics of the possible motions transcribed by a nucleus in order to emit electric radiation are shown in Fig. 2.12.

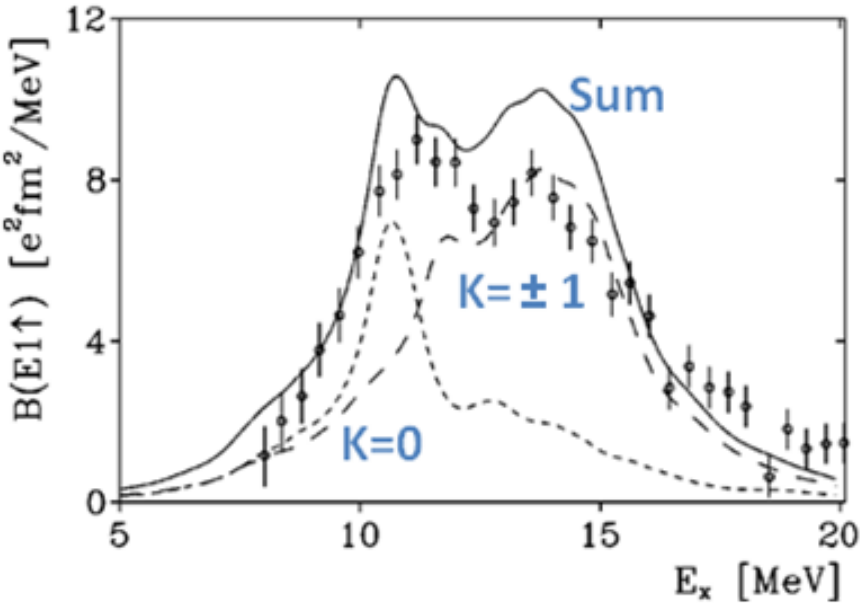

Figure 2.13: The giant dipole resonance in ^{238}U with the calculations shown as curves for the $K = 0$ axis and for the $K = \pm 1$ axis as well as their sum. Reproduced from Ref. [44].

Pygmy Dipole Resonances

There has been a large number of recent measurements [45–47] of the pygmy dipole resonance (PDR), which comprises of a concentration of low-lying electric dipole excitations in deformed nuclei with a substantial neutron excess [43]. The origin of this $E1$ excitation is described as a vibration of the excess neutrons ("neutron skin") against the inert (isospin-symmetric) core of the nucleus. It is expected that little to no PDR strength should exist in spherical nuclei and that as the neutron excess increases, so should the strength. Furthermore, it has been suggested that this strength, existing at lower energies below S_n and significantly above contributions from the low-energy tail of the GDR, must be produced from the deformation present in the nucleus itself [48, 49]. This requires complimentary measurements (photon scattering as well as photon dissociation) to be performed in order to verify existence. Additionally, existence of the PDR can play a

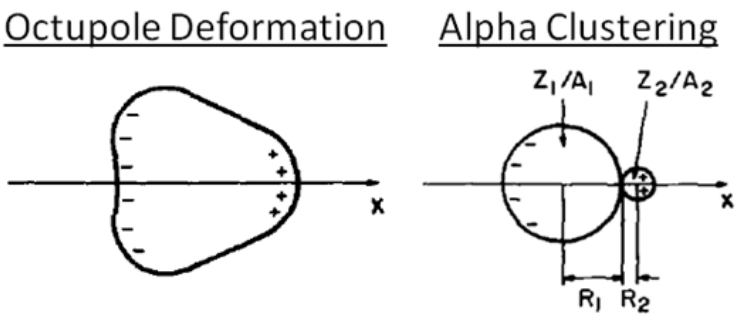

Figure 2.14: Schematics of octupole deformations and α-clustering of the nucleus. Reproduced from Ref. [32].

significant role in capture rates in p-process nucleosynthesis since its strength surrounds the region of excitation energies near S_n [50].

The existence of a PDR in ^{238}U ($\delta \approx 0.234$) has been suggested by the authors of Ref. [51] based on (γ, n) experiments but it was not quantitatively exploited (See Section 4.2 for details). For reference, the low-lying $E1$ states found in deformed, rare-earth nucleus ^{168}Er (Nilsson deformation parameter $\delta \approx 0.274$) has a summed strength of about $23(2)\times 10^{-3}$ e^2fm^2 within the energy range of 1.8-3.9 MeV [52]. It is unclear whether this measured $B(E1)$ is significantly greater than the strength produced by the low-energy tail of the GDR. In ^{138}Ba, a low-lying $E1$ strength was measured to be $0.96(18) \times 10^{-3}$ e^2fm^2 with a mean excitation energy of 6.7 MeV [45]. The experimental values were similar to theoretical calculations which predicted a strength of 1.22×10^{-3} e^2fm^2 with a mean excitation energy of 7.3 MeV for ^{138}Ba.

Octupole Deformations

The octupole deformation is typically thought to be the origin of $E1$ transitions existing in the energy range between 1-2 MeV when coupled to the GDR. This mechanism exists

when a nonuniform distribution of protons and neutrons is present due to electrostatic effects such that a vibration of the nucleus is produced around its reflection-asymmetric shape [32]. The octupole strength can be estimated for this mechanism by the following equation [53]:

$$B(E1)_{oct} = \frac{9}{4\pi} < {D_{oct}}^2 > \quad , \tag{2.55}$$

where D is the electric dipole moment given as

$$D_{oct} = 6.87 \times 10^{-4} AZ\beta_2\beta_3 \ \ [e \text{ fm}] \ , \tag{2.56}$$

and β_2 (β_3) is the quadrupole (octupole) deformation parameter (see Section 4.1 for details on these parameters). The authors of Ref. [53] measured a significant amount of low-lying $E1$ strength of 3.0(4), 3.1(5), and 5.0(4) $\times 10^{-3}$ e^2fm^2 in ^{150}Nd, ^{160}Gd, and ^{162}Dy, respectively, suggesting that the strength could be due to the octupole deformation of the nucleus. They measured $B(E1)_{oct}$ to be 2.9, 3.7, and 4.0 $\times 10^{-3}$ e^2fm^2, for ^{150}Nd, ^{160}Gd, and ^{162}Dy. Since the values for $B(E1)_{oct}$ do not exhaust the full measured strength, other mechanisms such as α-clustering, were considered. Schematics of the octopole deformations that would excite the nucleus into emitting electric radiation are shown in the left panel of Fig. 2.14.

α-Clustering

The $E1$ strength due to α-clustering is thought to be an origin of transitions in the energy range of 2-3 MeV. In this case, a nonuniform distribution of protons and neutrons is present such that the nucleus bunches into fragments with differing charge to mass ratios

[32]. This cluster configuration is most likely found in configurations other than the ground state one with only slight admixtures (of amplitude η) into it. Additionally, fragments may not be spherical in nature and a corresponding oscillation between clusters or bunches of fragments could occur. This α-clustering strength is estimated by the following equation [53]:

$$B(E1)_{\alpha} = \eta^2 \frac{9}{4\pi} \frac{< {D_{\alpha}}^2 >}{6} \quad , \tag{2.57}$$

where η is the clustering amplitude and D_{α} is given as

$$D_{\alpha} = 2e \frac{N-Z}{A} r_0 \left((A-4)^{1/3} + 4^{1/3} \right) \quad . \tag{2.58}$$

Again, the authors of Ref. [53], unsure of what mechanism was producing the entirety of the measured low-lying strength in their experiments, predicted that the strength could have been generated by α-clustering as well. They measured $B(E1)_{\alpha}$ to be 1.29, 1.34, and 1.15 $\times 10^{-3}$ e^2fm^2, for ^{150}Nd, ^{160}Gd, and ^{162}Dy, respectively. Small admixtures, $\eta = 10^{-3}$, were assumed in calculating out the strengths. Schematics of α-clusterings that would excite the nucleus into emitting electric radiation are shown in the right panel of Fig. 2.14.

Chapter 3

Theoretical Model Calculations

Mean-field models have been successful in describing the shell structure of the nucleus and the characteristics of single-particle excitations but they do not contain enough detailed features of the exact solutions to the Schrödinger equation for reproduction of collective excitations. However, random-phase approximation may be able to predict collective excitations since it includes important two-body interactions as well as strong particle-hole excitations. This forms the foundation for the quasiparticle random-phase approximation which provides a good interpretation of the nucleon interactions for predicting discrete levels in open-shell nuclei. The following chapter discusses some details of the formalism for both microscopic descriptions of nuclear motion.

3.1 Random-Phase Approximation

Mean-field theory provides the approximation that the nucleons interact with other nucleons through average potentials. The random-phase approximation (RPA) is a method of building upon this mean-field theory to describe collective excitations. The Hamiltonian $\hat{H}$

is written in terms of a particle-hole interaction potential V such that

$$\hat{H} = -\frac{\hbar^2}{2m}\sum_{i=1}^{N}\nabla_i{}^2 + \sum_{i<j=1}^{N} V_{ij} = \sum_{\alpha}\epsilon_\alpha a_\alpha{}^\dagger a_\alpha + {}^1\!/_2 \sum_{\alpha<\beta,\gamma<\delta} V_{\alpha\beta\gamma\delta} a_\alpha{}^\dagger a_\beta{}^\dagger a_\delta a_\gamma \ , \tag{3.1}$$

where i (j) is the number of particle (hole) states, ϵ_α is the single-particle energy, m is the electron mass, and $a^\dagger$ is the particle (hole) creation operator. Starting with the equation of motion,

$$\hat{H} \mid n\rangle = E_n \mid 0\rangle \ , \tag{3.2}$$

where E_n is the excitation energy, the many-body Schrödinger equation can be written as

$$\left[\hat{H}, \hat{\zeta}_n{}^\dagger\right] \mid 0\rangle = (E_n - E_0)\,\hat{\zeta}_n{}^\dagger \mid 0\rangle \ , \tag{3.3}$$

where E_0 is the ground-state energy and creation $\hat{\zeta}_n{}^\dagger$ and destruction $\hat{\zeta}_n$ operators are defined such that

$$\mid n\rangle = \hat{\zeta}_n{}^\dagger \mid 0\rangle \ , \tag{3.4}$$

and

$$\hat{\zeta}_n \mid 0\rangle = 0 \ . \tag{3.5}$$

where $\hat{\zeta}_n{}^\dagger$ spans the space of n-particles-n-holes and $\mid 0\rangle$ is the true ground-state wavefunction. Within the random-phase approximation, $\mid 0\rangle$ is approximated by the ground-state wavefunction of the RPA calculation, $\mid RPA\rangle$, such that

$$\hat{\zeta}_n \mid RPA\rangle = 0 \ . \tag{3.6}$$

The quantity $\hat{\zeta_n}^\dagger$ is approximated as

$$\hat{\zeta_n}^\dagger = \sum_{i,j} \left\{ {X_{ij}}^n {a_i}^\dagger a_j - {Y_{ij}}^n {a_j}^\dagger a_i \right\} \quad . \tag{3.7}$$

with the following quasiboson approximation:

$$\langle RPA \mid \left[\hat{\zeta_n}, \hat{\zeta_{n'}}^\dagger \right] \mid RPA \rangle \simeq \langle HF \mid \left[\hat{\zeta_n}, \hat{\zeta_{n'}}^\dagger \right] \mid HF \rangle = \delta_{nn'} \quad , \tag{3.8}$$

where $\mid HF \rangle$ is the Hartree Fock ground state. The RPA equations are now a set of linear equations with normalized amplitudes ${X_{kl}}^n$ and ${Y_{kl}}^n$,

$$\left[E_n \begin{pmatrix} 1 & 0 \\ 0 & -1 \end{pmatrix} - \begin{pmatrix} A_{ijkl} & B_{ijkl} \\ B{*}_{ijkl} & A{*}_{ijkl} \end{pmatrix} \right] \begin{pmatrix} {X_{kl}}^n \\ {Y_{kl}}^n \end{pmatrix} = 0 \tag{3.9}$$

with coefficients A_{ijkl} and B_{ijkl} defined as

$$\begin{aligned} A_{ijkl} &= (\epsilon_i - \epsilon_j)\delta_{ik}\delta_{jl} + V_{iljk} \\ B_{ijkl} &= V_{ikjl} \quad . \end{aligned} \tag{3.10}$$

From the solutions to the RPA equations, the energies and amplitudes are obtained. A general one-body external field $\hat{f}$ can be defined as

$$\hat{f} = \sum_{\alpha\beta} f_{\alpha\beta} {a_\alpha}^\dagger a_\beta \quad . \tag{3.11}$$

The random-phase approximation approximates the transition matrix element of the field operator as

$$\langle n \mid \hat{f} \mid RPA \rangle = \sum_{ij} \left\{ X_{ij}{}^{*n} f_{ij}{}^{*} + Y_{ij}{}^{*n} f_{ji} \right\} \quad . \tag{3.12}$$

The strength function $S(E)$ is defined by

$$S(E) = \sum_{n} |\langle n \mid \hat{f} \mid RPA \rangle|^2 \delta(E - E_n) \quad . \tag{3.13}$$

The partial width as well as the cross section can be written in terms of $S(E)$.

3.2 Quasiparticle Random-Phase Approximation

RPA assumes a discontinuity at the Fermi energy within the occupational probabilities, which means that there is either a particle returning below the Fermi surface or a particle promoted above the Fermi surface. However this is not generally true for open-shell nuclei, in particular for deformed rare-earth and actinide nuclei. There could be a mixture of these states, part-particle and part-hole, for which are not accounted within the RPA. The occupation probability of these quasiparticles is continuous at the Fermi energy, which means that they can include the possibility of p-p, p-h, and h-h combinations. Quasiparticles are therefore defined as linear combinations of normalized particle- and hole-states, such that

$$\alpha_{\lambda}{}^{\dagger} = c1_{\lambda} a_{\lambda}{}^{\dagger} - c2_{\lambda} a_{-\lambda} \quad , \tag{3.14}$$

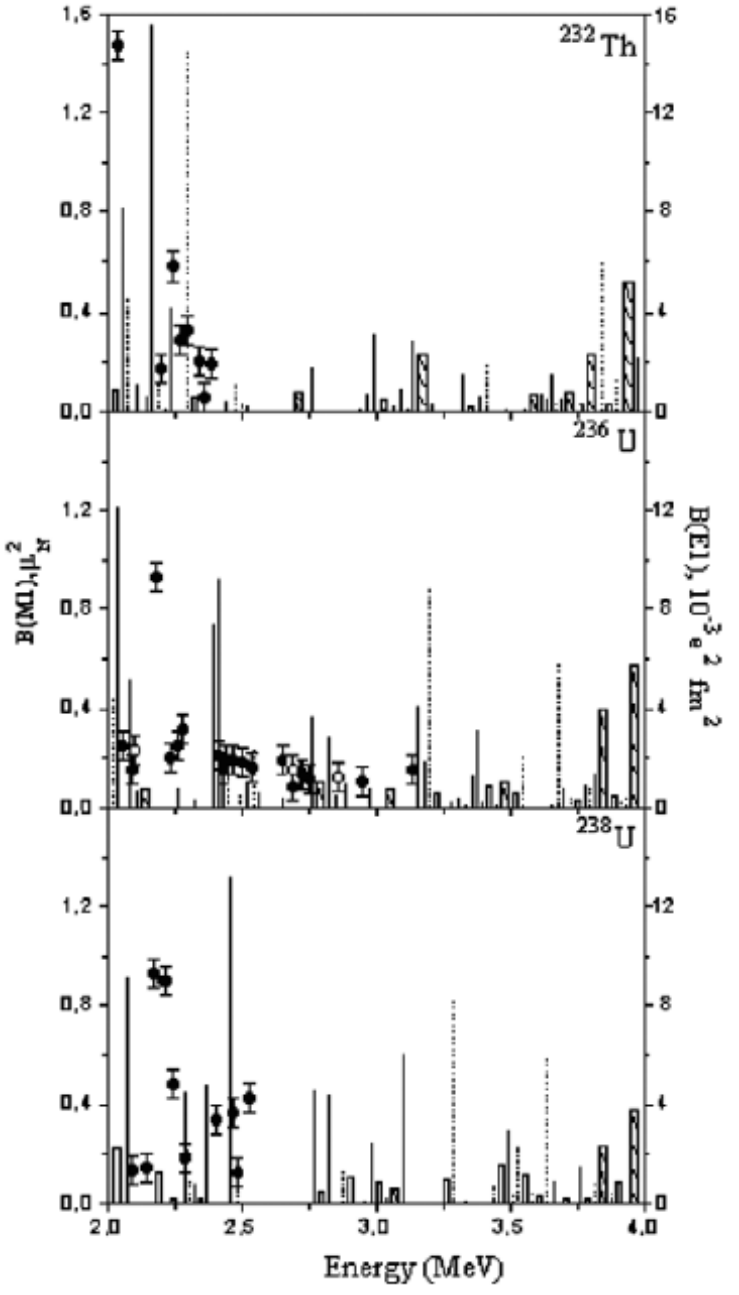

Figure 3.1: QRPA calculation by Ref. [30] for $M1$ and $E1$ states in (a)^{232}Th, (b) ^{236}U, and (c) ^{238}U, with the experimentally observed $M1$ excitations with $\Delta K = 1$ in (•) and $E1$ excitations with $\Delta K = 0$ in (◦) [1, 54]. In the QRPA results, $M1$ excitations with $\Delta K = 1$ are shown as a solid line and $E1$ excitations as a dashed line, whereas $E1$ and $M1$ excitations with $\Delta K = 0$ are shown as open and hatched bars, respectively.

Table 3.1: Magnetic and electric dipole strengths as calculated by QRPA [30] and QPNM [31] for actinide nuclei.

	Magnetic Dipole			
	^{232}Th [30]	^{236}U [30]	^{238}U [30]	^{238}U [31]
ω (MeV)	2.6	2.6	3.2	-
$\sum B$ ($\mu_N{}^2$)	5.0	6.1	8.3	6.0
$\sum B/\Delta E$ ($\mu_N{}^2$/MeV)	2.5	3.1	2.3	1.5
Range (MeV)	2 - 4	2 - 4	2 - 5.6	2.6 - 6.6
	Electric Dipole			
	^{232}Th [30]	^{236}U [30]]	^{238}U [30]	^{238}U [31]
ω (MeV)	2.7	3.0	4.6	-
$\sum B$ ($\times 10^{-3} e^2$fm^2)	35	40	120	308
$\sum B/\Delta E$ ($\times 10^{-3}$ e^2fm^2/MeV)	18	20	33	77
Range (MeV)	2 - 4	2 - 4	2 - 5.6	2.6 - 6.6

where $c1$ and $c2$ are normalization coefficients. In order to create an excited state using the quasiparticle operator and ground state, $\hat{\zeta}_n{}^\dagger$ needs to be redefined,

$$\hat{\zeta}_n{}^\dagger = \sum_{\alpha>\beta} \left\{ X_{\alpha\beta}{}^n \alpha_\alpha{}^\dagger \alpha_\beta{}^\dagger - Y_{\alpha\beta}{}^n \alpha_\beta \alpha_\alpha \right\} \quad . \tag{3.15}$$

The quantity $\hat{\zeta}_n{}^\dagger$ is more or less a quasiboson creation operator which builds excited states through a superposition of two-quasiparticle excitations of a quasiparticle ground state. Also, pairs of the fermion operators, $\alpha_\beta \alpha_\alpha$, are treated as quasibosons within QRPA. Finally, within the quasiparticle random-phase approximation, the true ground-state is approximated by the ground-state wavefunction of the QRPA calculation, $| \, QRPA \rangle$, such that

$$\hat{\zeta}_n \, | \, QRPA \rangle = 0 \quad , \tag{3.16}$$

which is much like the prescriptions laid out within the previous section on RPA.

Published examples of QRPA calculations are those done by Kuliev *et al*. [30, 55] for ^{232}Th, ^{236}U, and ^{238}U (see Fig. 3.1) as well as by Soloviev *et al*. [31] for ^{154}Sm, ^{168}Er, ^{178}Hf, and ^{238}U. Table 3.1 highlights the quantitative description of the calculations for summed $M1$ and $E1$ strength of the actinides. Both calculations use axial symmetric Woods-Saxon potentials to find single-particle energies. A separable form of $\hat{H}$ is used such that the two-body interaction potential is further subdivided multiple interaction terms. The $\hat{H}$ used by Kuliev *et al*. [30] is as follows:

$$\hat{H} = \hat{H}_{sqp} + \hat{h}_0 + \hat{h}_1 + \hat{V}_{\sigma\tau} \tag{3.17}$$

for $M1$ transitions and

$$\hat{H} = \hat{H}_{sqp} + \hat{h}_0 + \hat{h}_\delta + \hat{W}_1 \tag{3.18}$$

for $E1$ transitions, where $\hat{H}_{sqp}$ is the Hamiltonian of the single-quasiparticle motion, $\hat{h}_0$ and $\hat{h}_1$ describe the isoscalar and isovector restoring interactions, $\hat{V}_{\sigma\tau}$ is the spin-isospin interaction, $\hat{h}_\delta$ are the interactions for transitional and Galilean symmetries, and $\hat{W}_1$ are the coherent isovector dipole vibrations of protons and neutrons. The $\hat{H}$ of Soloviev *et al*. [31] is defined as

$$\hat{H} = \hat{H}_{sp} + \hat{V}_{pair} + \hat{V}_{ph} + \hat{V}_{pp} \tag{3.19}$$

where H_{sp} is the one-body Hamiltonian, $\hat{V}_{pair}$ is the monopole pairing interactions, and $\hat{V}_{ph}$ ($\hat{V}_{pp}$ is the particle-hole (particle-particle) interactions. Soloviev *et al.* [31] take the QRPA model a step further by using a quasiparticle -phonon nuclear model in which energies and strengths were calculated within a space spanned by up to two RPA phonon states which

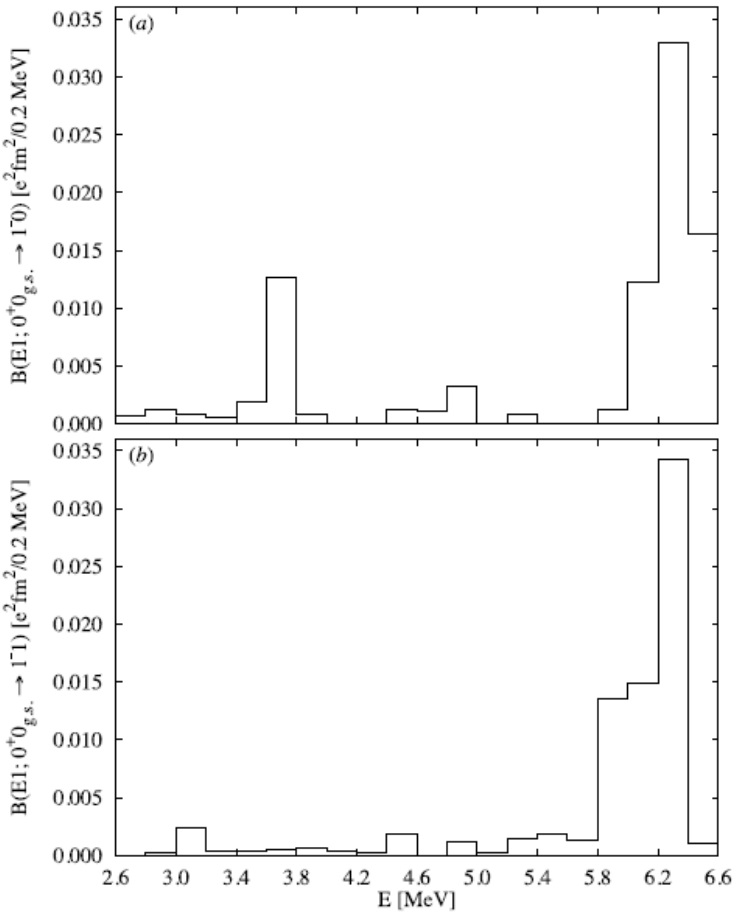

Figure 3.2: QPNM calculation by Ref. [31] for (a) K=0 and (b) K=1 $E1$ strength distributions in ^{238}U.

produce the right order of magnitude. The strength is fragmented over several states instead of all of the strength carried by only a couple states. An example of $B(E1)$ calculations for ^{238}U is shown in Fig. 3.2.

In Chapter 7, a comparison of these calculations are made with the present experiment to which good agreement is found for the $M1$ strength but not for the $E1$ strength in ^{238}U.

Chapter 4

Experimental Information on ^{238}U and Other Deformed Nuclei

---

In order to put the measurements of this dissertation in proper perspective, a summary of the previous experimental data from excitation of ^{238}U using probes of photons, electrons, and protons below the neutron separation energy, S_n, is provided. The energy region above S_n is not the focus of this dissertation, however, a thorough investigation of the giant dipole resonance was completed by Caldwell *et al.* in Ref. [42].

4.1 Collective Excitations in $140 < A < 180$ Nuclei

There are an overwhelming number of experiments performed on rare-earth nuclei as well as other nuclei with $140 < A < 180$. It would be beneficial if these experiments could provide insight into the actinide nuclei which are much like heavier-massed versions of these nuclei. In Fig. 4.1, a NRF spectrum of ^{154}Sm shows how peaks can be easily identified at higher energies when the nucleus has a small density of states. A NRF spectrum from a heavy-mass nuclei at a similar energy would be relatively harder to identify discrete

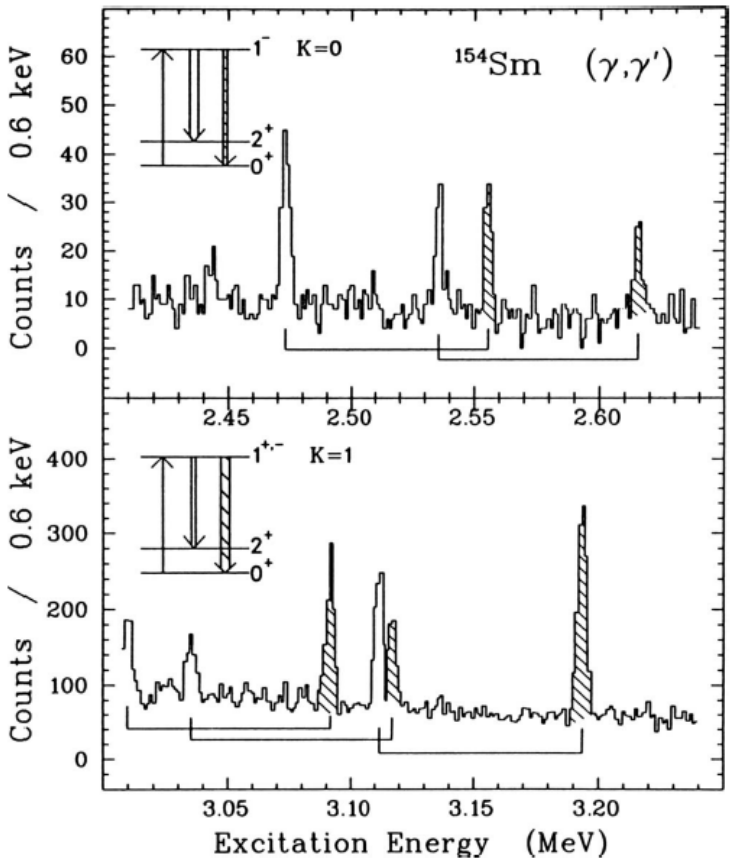

Figure 4.1: NRF spectra from ^{154}Sm from Ref. [56]. Transitions to the ground state (hatched peak areas) and to the first excited (unhatched peak areas) state are connected by a bracket for a particular level. Top panel shows $K = 0$ states while the bottom panel shows $K = 1$ states.

transitions than nuclei with $140 < A < 180$ since there is a larger density of states present. Some questions arise when looking at the two different types of nuclei: Does size matter enough to produce different excitation modes between similar $140 < A < 180$ nuclei and actinide nuclei? Do collective excitation modes for similarly deformed nuclei, regardless of mass, behave in the same way or are there other factors that contribute to the distribution and intensity of the observed strength?

The strength and location of each collective mode of interest to this dissertation was investigated for nuclei with $140 < A < 180$, in particular, the rare-earth nuclei [38, 40,

52, 57, 58]. The scissors mode has been observed at energies between 2.4-3.7 MeV with a mean excitation energy ω_{M1} ~3.0 MeV and with the total strength $\Sigma B(M1)$ between 0.20(2)-3.7(6) $\mu_N{}^2$, depending on the degree of deformation [38] (see below for details on the sum rule used to calculate the strength). The total strength for the scissors mode is observed to be $\sim$ 3 $\mu_N{}^2$ while the maximum strength of any one individual state is never greater than 1.5 $\mu_N{}^2$.

The spin-flip excitation mode is presumed to be located in the energy range between 4 and 10 MeV, and is well separated from the scissors mode. In Fig. 4.2, the effect of a heavier-mass nuclei is clear. The centroids of the isoscalar and the isovector parts of the spin-flip mode are pushed to lower energies in the actinide nuclei than for the rare-earth nuclei. As for the quantitative aspect of the spin-flip mode, $\Sigma B(M1)$ has been found to be between 10-15 $\mu_N{}^2$ in the energy range of 6-10 MeV for nuclei with a similar deformation as in ^{238}U ($\delta = 0.234$) [40].

On the other hand, experimental data on low-lying $E1$ strength in $140 < A < 180$ nuclei are currently being investigated. One example of an experiment looking for a possible PDR is that of Ref. [52] which looked for low-lying $E1$ strength in deformed, rare-earth nucleus ^{168}Er (deformation parameter $\delta \approx 0.274$). The authors of Ref. [52] found a total $E1$ strength of about 23(2)$\times 10^3$ e^2fm^2 within the energy range of 1.8-3.9 MeV. It is unclear whether this measured $B(E1)$ is significantly greater than the strength produced by the low-energy tail of the GDR.

There have also been some theoretical predictions of the strength from the rare-earth nuclei [31, 38]. Table 4.1 provides an example of a comparison of experimental values

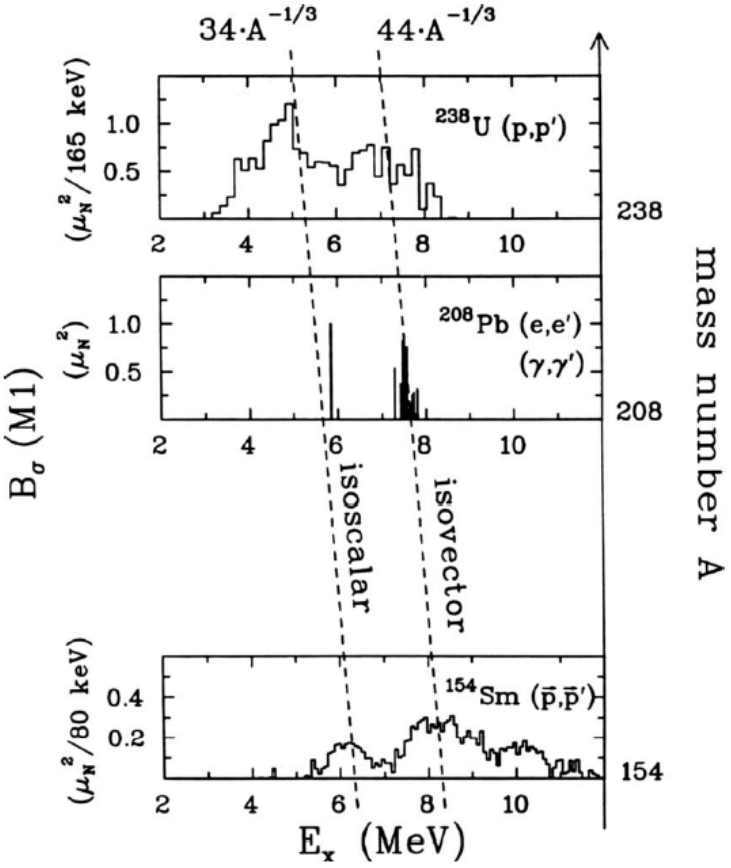

Figure 4.2: NRF and proton-scattering spectra for various nuclei showing the separation of the scissors and spin-flip modes. Reproduced from Ref. [3].

with the predicted values for ^{154}Sm, ^{160}Gd, and ^{178}Hf. The sum-rule prediction of Ref. [38] agrees well with the experimental scissors mode strength. For example, the sum rule predicts $B(M1)$ for ^{178}Hf to be 2.14 $\mu_N{}^2$ where as the measured value is between 2.04-2.40 $\mu_N{}^2$. However, it is uncertain whether the predictions from the theoretical calculations from Ref. [31] on the $E1$ strength are well-justified and more experimental data on the low-lying $E1$ strength of rare-earth nuclei are needed.

Enders *et al.* [38] compiled the existing data on scissors mode for nuclei with $140 < A < 180$ as well as actinide nuclei to compare with a parameter-free sum-rule prediction. Under this description of the sum rule, the strength function S can be calculated from the

Table 4.1: Experimental and theoretical values for the $M1$ (in units of ${\mu_N}^2$) and $E1$ strengths (in units of $\times 10^{-3}$ $e^2\text{fm}^2$) of ^{154}Sm, ^{160}Gd, and ^{178}Hf. Energies are in units of MeV.

Magnetic Dipole						
	Experiment			*Theory*		
	^{154}Sm [57]	^{160}Gd [53]	^{178}Hf [58]	^{154}Sm [31]	^{160}Gd [59]	^{178}Hf [31]
ω	3.26	3.06(4)	3.21	–	–	–
$\sum B$	2.4(4)	3.6(4)	2.4(4)	5.7	3.54	7.1
$\sum B/\Delta E$	1.6	1.8	1.6	1.4	1.8	1.8
Range	2.5-4	2-4	2.5-4	3.6-7.6	2-4	3.6-7.6
Electric Dipole						
	Experiment			*Theory*		
	^{154}Sm [57]	^{160}Gd [53]	^{178}Hf [58]	^{154}Sm [31]	^{160}Gd [59]	^{178}Hf [31]
ω	2.81	2.9(1)	–	–	–	–
$\sum B$	24(4)	16(2)	>4	217	21	271
$\sum B/\Delta E$	13	8	>2	54	11	68
Range	2-4	2-4	1.2-4	3.6-7.6	2-4	3.6-7.6

ground-state expectation values, separately for $J^\pi = 1^+$ and for $J^\pi = 1^-$ such that the mean excitation energy ω_{M1} is written as [38]

$$\omega = \sqrt{\frac{S(J^\pi = 1^+)}{S(J^\pi = 1^-)}} \ , \tag{4.1}$$

while the total strength $\sum B(M1)$ is written as [38]

$$\sum B(M1) = \sqrt{S(J^\pi = 1^+)S(J^\pi = 1^-)} \ . \tag{4.2}$$

From Lipparini and Stringari [38, 60], these quantities can be rewritten in terms of familiar components. The final results are shown:

$$\sum B(M1) = \frac{3}{\pi}\sqrt{\frac{3}{20}} r_0 A^{5/6} \sqrt{\frac{4NZ}{A^2}} \omega_D \sqrt{\frac{m_N \xi}{\omega_{E2}}} \delta g_{IS}^2 \tag{4.3}$$

$$\omega_{M1} = \frac{2}{\sqrt{15}} r_0 A^{5/6} \sqrt{\frac{A^2}{4NZ}} \omega_D \sqrt{m_N \omega_{E2} \xi} \delta \ , \tag{4.4}$$

where Z, N, A are the proton, neutron, and mass number of the nucleus, r_0 is the radius of the nucleus (~1.15 fm), ξ describes the contribution from isovector giant quadrupole resonance (IVGQR), ω_D describes the centroid energy of the isovector giant dipole resonance (IVGDR), δ is the Nilsson deformation parameter, m_N is the nucleon mass, ω_{E2} describes mean $E2$ excitation energy, and g_{IS} is the isoscalar orbital gyromagnetic factor of the ground state rotational band which is dependent on g_π and g_ν, the gyromagnetic factor for protons and neutrons, respectively.

The quantity δ can be written in terms of the quadrupole deformation parameter, β_2, such that

$$\delta = \frac{3}{4} \sqrt{\frac{5}{\pi}} \beta_2 + \frac{125}{32\pi^2} {\beta_2}^4 - \frac{175}{64\pi^2} \sqrt{\frac{5}{\pi}} {\beta_2}^5 + \ldots \tag{4.5}$$

and

$$\beta_2 = \frac{4\pi}{3Z{r_0}^2} \sqrt{\frac{B(E2)}{e^2}} = \frac{4\pi}{3Z{r_0}^2} \sqrt{\frac{5}{16\pi}} Q_0 \tag{4.6}$$

where $B(E2)$ is the reduced transition probability and Q_0 is the quadrupole moment. Enders *et al.* [38] predicted ω_{M1} and the $M1$ strength for the scissors mode of many $140 < A < 180$ nuclei using these results. In Fig. 4.3, the upper panel shows a comparison of ω_{M1} while the bottom panel shows the comparison of $\Sigma B(M1)$ observed for nuclei with different deformations. From this compilation, ω_{M1} seems to be fairly independent of deformation, although as the mass of the nuclei increases significantly, ω_{M1} decreases. The strength $\Sigma B(M1)$ however is strongly dependent on the deformation of the nucleus, and was deduced as a quadratic dependence. This was shown experimentally for rare-earth nuclei in Ref. [36]

such that the quantity ξ

$$\xi = \sum B(M1)A^{2/3}Z^{-2} \tag{4.7}$$

was found to depend linearly on the square of the deformation such that $\xi \approx 0.27\delta^2$. As for the sum rule, it seems to predict $\Sigma B(M1)$ of the least and most deformed nuclei of the group but not those that are somewhere in between.

The deformation-dependent strength is illustrated in Fig. 4.3 for both nuclei with $140 < A < 180$ and the actinides. The mean excitation energy is also provided and is shown not to vary with the square of the deformation, but with the change in mass region between rare-earth and actinide nuclei. There are discrepancies between the measurements and the sum-rule predictions in Fig. 4.3 which seem to suggest either missing $M1$ strength within the experimental value of $\Sigma B(M1)$ or an invalid phenomenological description of the scissors mode as provided by this sum-rule prediction. Only a remeasurement of the energy range relevant to the scissors mode would clear up any doubt to which was the accurate description of the data. Finally, experimental information on deformed nuclei within $140 < A < 180$ may provide insight into the nuclear structure of the actinides by comparing and contrasting features of the distributions of the dipole strengths, the frequencies of similar R_{exp} values, as well as other characteristics discussed in Chapter 7.

4.2 Actinide Data

In 1972 and 1973, Bergére *et al.* [41] as well as Knowles and Mafra [61], performed experiments above S_n with high-intensity γ rays on ^{238}U. Specifically, Knowles and Mafra

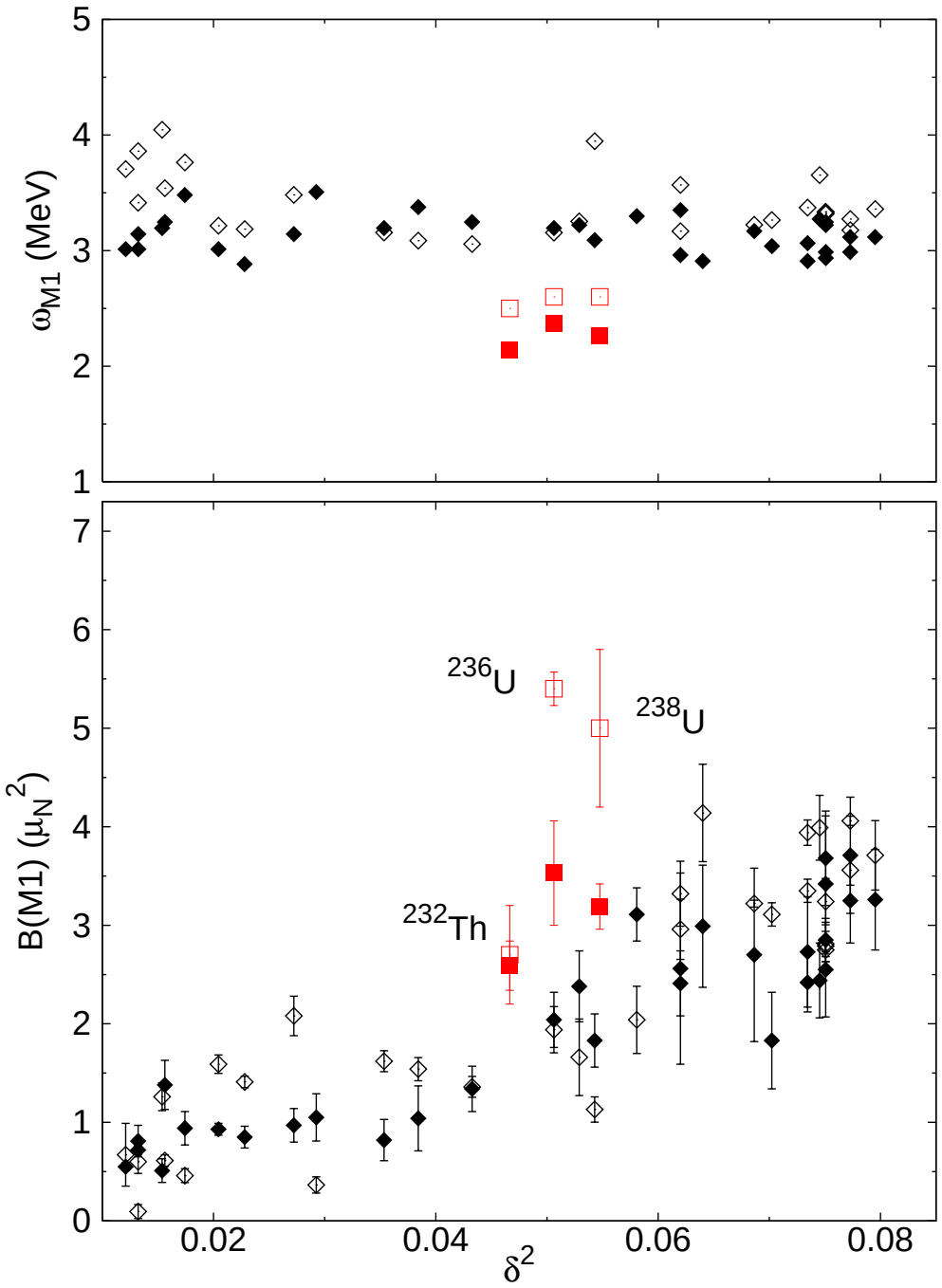

Figure 4.3: The experimental mean excitation energy and $M1$ transition strength as well as its sum-rule prediction as it depends on the deformation parameter δ squared for $140 < A < 180$ nuclei and actinide nuclei. The sum-rule prediction of Ref. [38]is in (◊) while the experimental data is in (◆) for $140 < A < 180$ nuclei. For the actinides, the sum-rule prediction is in (□) while the experimental data [1, 54] is in (■). There is a large discrepancy between experiment and prediction for ^{238}U. Reproduced from Ref. [38].

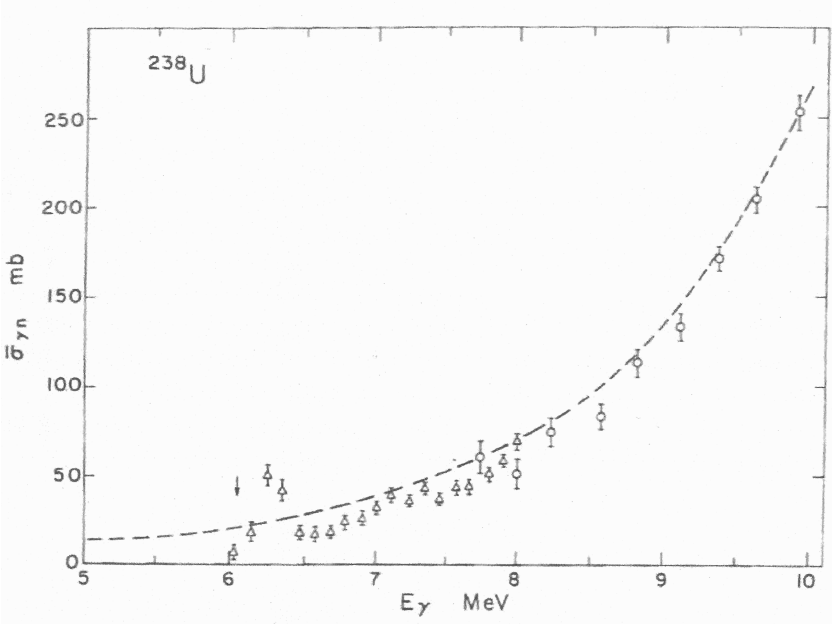

Figure 4.4: The photoabsorption cross section of ^{238}U shown as points with error bars. The low-energy tail of the GDR is also shown as the dashed curve. Reproduced from Ref. [51].

used a Compton-monochromator facility to produce variable γ-ray beams between 3 and 8.3 MeV with an energy spread of about 3% [51]. Their results are shown in Fig. 4.4.

In 1980, Schumacher *et al.* [27] used the Grenoble high-flux reactor to irradiate 25 g of cerium oxide to create a large flux of collimated neutron-capture γ rays at energies of 4.291 and 4.767 MeV. The reactor data was supplemented by lower-energy measurements [62] using radioactive sources as the origin of the incident γ rays with the following energies: 0.279, 0.412, 0.662, 0.889, 1.121, 1.173, and 1.332 MeV. The differential elastic-scattering cross section at 120° for ^{238}U was measured and compared with predictions from Rayleigh and Delbrück theory (shown in Fig. 4.5).

A year later, Mückenheim *et al.* [63], with a moving ^{56}Co source in a high speed centrifuge, stimulated the excitation of the 3.254 MeV level in ^{238}U. Differential cross-section measurements were made using a Ge(Li) detector placed about 30 cm from a block

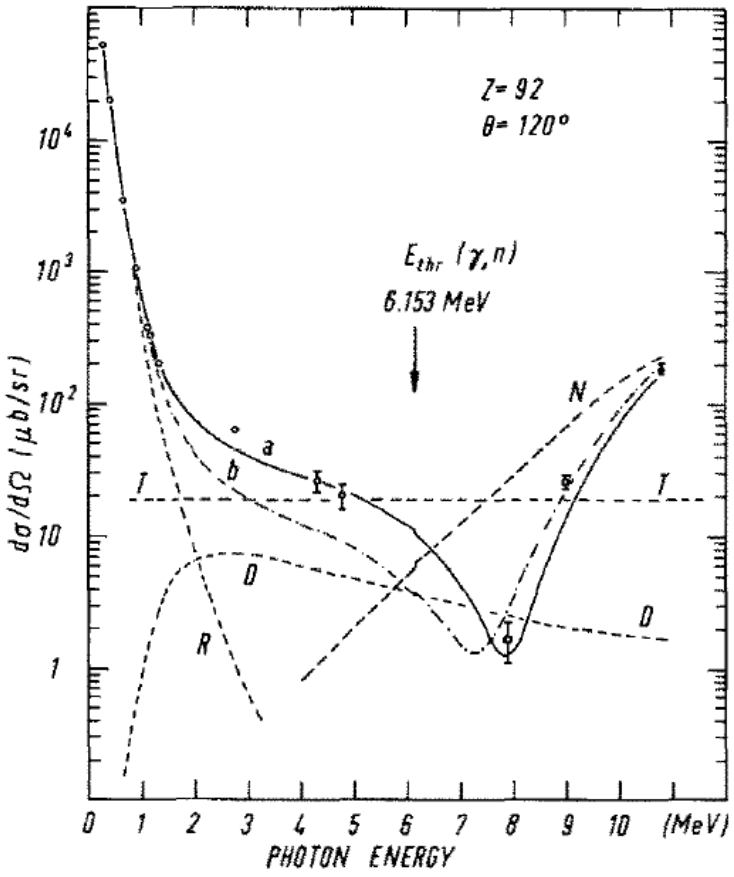

Figure 4.5: Differential elastic scattering cross sections for ^{238}U (◆) showing the contributions from coherent scattering processes of Raleigh (R), Delbrück (D), Thomson (T), and nuclear resonance (N). Theoretical calculations including all four processes (a) and without D (b) are shown as well. Reproduced from Ref. [27].

of metallic uranium and at various angles between 56° and 120°.

In 1982, Rullhusen *et al.* [64] studied the elastic-scattering of high-intensity photons between 2-10 MeV produced either by the neutron-capture reaction (created within a reactor) or with strong radioactive sources (such as ^{24}Na, ^{56}Co, and ^{66}Ga). Transitions were observed at 2.754, 3.809, 4.495, 4.592, 4.807, 5.140, 5.206, 5.666, and 5.843 MeV, but the authors of Ref. [64] were unable to assign definite parity and spin for most of these levels.

Again in 1983, the Grenoble reactor setup was used by Zurmühl *et al.* [65] to create neutron-capture γ rays for exploring NRF in ^{238}U between 4 and 7 MeV. The scattering

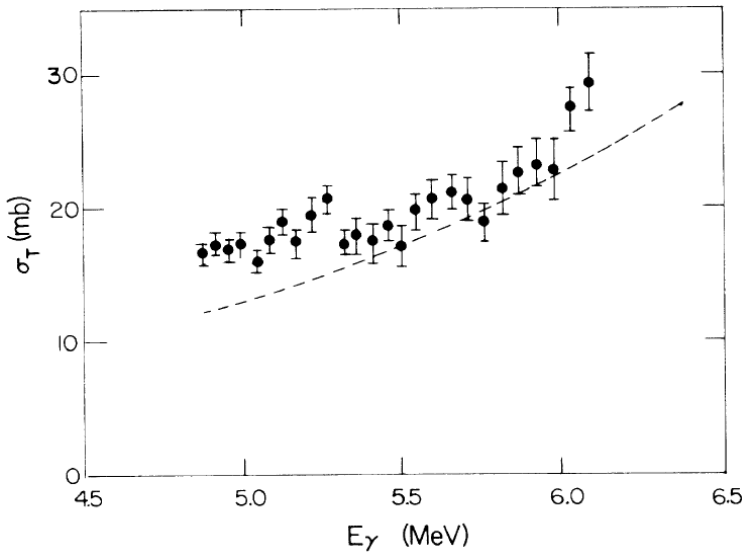

Figure 4.6: The photoabsorption cross section for ^{238}U as derived from the elastic-scattering cross section and compared with the Lorentzian extrapolation of the low-energy tail of the GDR (dashed curve). Reproduced from Ref. [66].

target was made of 1.8 g of metallic uranium. Two Ge(Li) detectors were positioned at distances of 20 cm from the target at angles of 90° and 130°. Fifteen NRF lines were observed at the following energies: 4.220, 4.414, 4.536, 4.566, 4.618, 4.692, 4.739, 5.090, 5.165, 5.246, 5.343, 5.747, 5.949, 5.965, and 6.128 MeV. The differential NRF cross sections were measured.

In 1987, Birenbaum *et al.* [66] measured the photon elastic scattering cross section on ^{238}U between 4.8 and 6.4 MeV. A continuous γ-ray beam was created at the University of Illinois using their tagged-photon facility and the target-scattered photons were collected in a large volume NaI detector while post-Bremsstrahlung electrons were collected in coincidence in an array of thirty-two plastic scintillators. Final results from Birenbaum *et al.* in terms of the photoabsorption cross section are inconclusive on whether or not a PDR exists in ^{238}U (see Fig. 4.6).

At the advent of the discovery of the collective excitation mode known as the $M1$ scis-

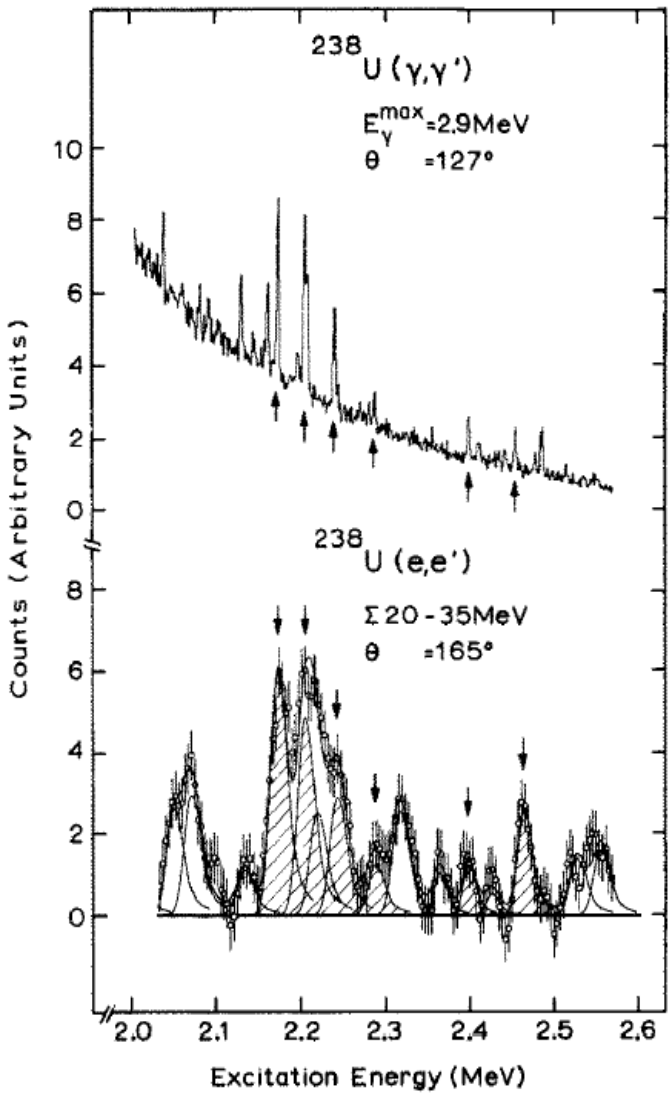

Figure 4.7: A comparison of the levels in ^{238}U from NRF and electron-scattering experiments. Reproduced from Ref. [1]. The arrows point to six ground-state $M1$ transitions, found at the same energies using NRF and electron scattering.

sors mode, different rare-earth and actinide nuclei were tested in order to explore the physical nature of this mode. One such set of measurements was done in 1988 on ^{232}Th and ^{238}U by Heil *et al.* at the University of Stuttgart at the 4 MeV Dynamitron [1]. They used a continuous γ-ray beam created through Bremsstrahlung with end point energies varying between 2.9 and 4.1 MeV. Three Germanium detectors were placed at 90°, 127°, and

150° within the scattering plane of the γ rays in order to determine the parity. The targets consisted of foils which had a total density of 10 $^{mg}/_{cm^2}$ for both thorium and uranium. Corresponding electron scattering experiments were performed for comparison with these NRF experiments in order to identify $M1$ states propagated through the scissors mode excitation (shown in Fig. 4.7) by only considering transitions found in both experiments. Spectroscopic information was found for the magnetic dipole transitions at 2.043, 2.248, 2.274 and 2.296 MeV in ^{232}Th and at 2.176, 2.209, 2.245, 2.299, 2.410 and 2.468 MeV in ^{238}U. Specifically for ^{238}U, the scissors mode was observed to exist between 2.0-2.5 MeV and the summed $M1$ strength was measured to be $\Sigma B(M1) = 3.2(2)\ \mu_N{}^2$ with a mean excitation energy ω_{M1} of 2.3(2) MeV. For ^{232}Th, the strength $\Sigma B(M1)$ was measured to be $2.6(3)\ \mu_N{}^2$ with ω_{M1} of 2.1 MeV. As seen in Fig. 4.3, there are large discrepancies between the measurement [1, 54] and the sum-rule prediction [38] for the uranium isotopes (see also Table 4.2). However, the experimental and predicted strength values for ^{232}Th seem to

Table 4.2: $M1$ strengths previous experiments [1, 54] compared with "sum rule" predictions [38] for actinide nuclei.

	Experiment		
	^{232}Th [1]	^{236}U [54]	^{238}U [1]
ω (MeV)	2.1	2.3	2.3
$\sum B$ ($\mu_N{}^2$)	2.6(3)	4.1(6)	3.2(2)
$\sum B/\Delta E$ ($\mu_N{}^2$/MeV)	5.2	2.9	5.3
Range (MeV)	1.9 - 2.4	1.8 - 3.2	2 - 2.6
	Sum Rule [38]		
	^{232}Th	^{236}U	^{238}U
ω (MeV)	2.5	2.6	2.6
$\sum B$ ($\mu_N{}^2$)	2.7(5)	5.4(2)	5.0(8)
$\sum B/\Delta E$ ($\mu_N{}^2$/MeV)	2.7	5.4	5.0
Range (MeV)	2 - 3	2 - 3	2 - 3

agree fairly well.

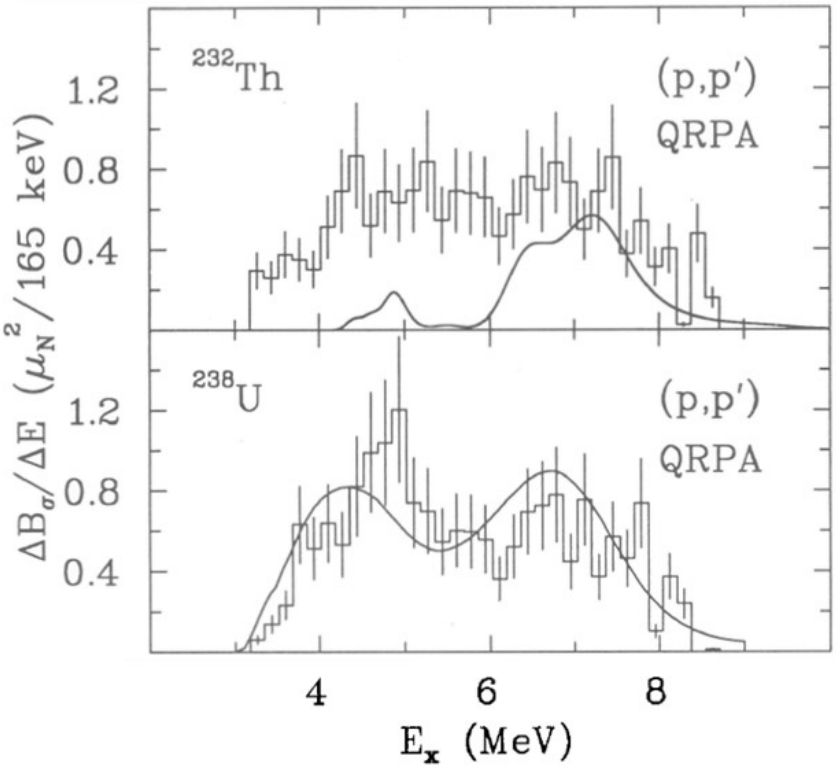

Figure 4.8: The spin-flip distribution in ^{232}Th and ^{238}U with open error bars as compared to a QRPA model prediction with a spin gyromagnetic factor quenched by 30% (solid curve). Reproduced from Ref. [39].

In 1994, Wörtche *et al.* [39] performed a set of inelastic-proton-scattering experiments using a 200 MeV polarized proton beam and actinide targets of ^{232}Th and ^{238}U to examine the $M1$ spin-flip excitation mode at TRIUMF. Proton polarization was measured using a spectrometer with a polarimeter in the focal plane. The total $M1$ spin-flip strength in ^{238}U was measured to be $18(5)\mu_N{}^2$ with a mean excitation energy of about 5.7 MeV (See Fig. 4.8). A similar result was found in ^{232}Th for the total strength and it's distribution. Discrete $M1$ transitions to lower-lying states (below 3.5 MeV) were not a part of the objective of these experiments.

Later in 1995, another set of ^{238}U measurements, using the same methods as Heil *et*

al. [1], were done by Zilges *et al.* at the University of Stuttgart at the 4 MeV Dynamitron, this time a Bremsstrahlung beam with an end point energy at 2.5 MeV was used to look at possible transitions below 2 MeV [37]. Three more magnetic dipole transitions were observed in ^{238}U at 1.782, 1.793, and 1.847 MeV and are shown in Fig. 4.9.

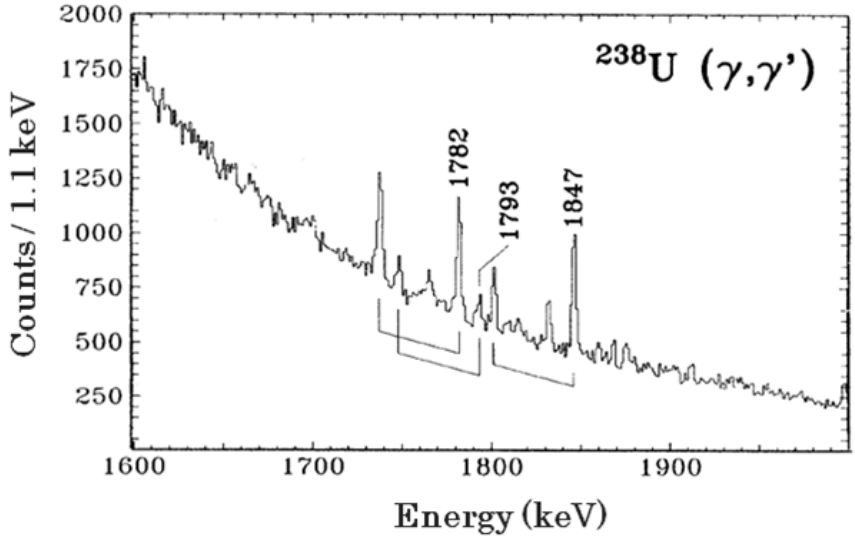

Figure 4.9: The levels in ^{238}U from a NRF experiment. Reproduced from Ref. [37].

More recently in 2010, Warren *et al.* [67] reports of measurements done on ^{238}U using the S-DALINAC at the Technical University Darmstadt to create collimated Bremsstrahlung γ rays with end-point energies of 8.3 and 10.0 MeV. Two high-purity Germanium detectors, with BGO Compton suppression shielding, were positioned around the target, one at 90° and the other at 130°. The target consisted of approximately 90 g of depleted uranium material. No new NRF signatures between the energies of 5 and 9 MeV were observed. The spectra from the measurements with an end-point energy of 10 MeV is shown in Fig. 4.10.

Finally, in 2011, Quiter *et al.* [68] in a series of NRF transmission experiments, reprised the measurements of Heil *et al.* [1] with a fresh look at the states below 2.5 MeV. These new

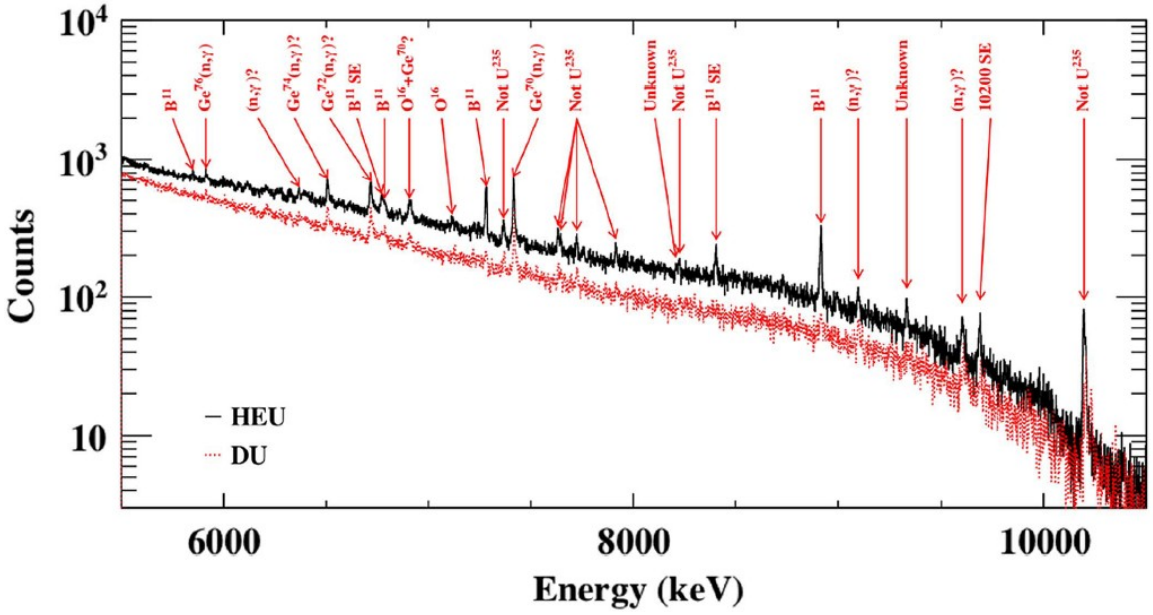

Figure 4.10: NRF spectra from 10 MeV end-point energy measurements where ^{235}U is shown as the black, solid histograms while ^{238}U is shown as the red, dashed histograms. Reproduced from Ref. [67].

experiments were conducted at the High Voltage Research Laboratory at Massachusetts Institute of Technology where a lead-collimated Bremsstrahlung beam with an end-point energy of 2.6 MeV was created. Several targets were used with varying purposes. Depleted uranium (DU) and lead assay targets were positioned after collimation to "remove" γ rays from the beam. Farther down the beam axis, a second target is positioned to fill the "notches" made from the first target within the NRF spectra. Two high-purity Germanium detectors housed within steel shields were located on either side of the second DU target at an angle of 62°. These experiments resulted in a remeasurement of the states in Ref. [1] while also providing newly observed γ-ray lines at 1996.6(3), 2035.0(2), 2080.0(2), 2146.0(3), 2241(1), and 2287.4(6) keV. Two new states at 2080 and 2287 keV were measured with the potential of a third state at 2101 keV. All new and remeasured states are assumed to be $M1$ transitions by Ref. [1] and Ref. [68]. The assumption that transitions

between 2-2.5 MeV should be a $M1$ transition seems to be a fair assessment based on prior experiments. However, it does not hold true; the present work claims one of the states measured by Ref. [68] is actually a transition to the first excited state from an $E1$ transition to the ground-state. See Fig. 4.11 for their transmission spectra from ^{238}U.

As a summary of the previous experiments on ^{238}U, the known states of ^{238}U prior to this dissertation are given in Table 4.3. As described in Chapter 6, more than 100 new states were observed in the course of the present experiment and well as the remeasurement of most of the states provided in the table. The large number of observed states in the

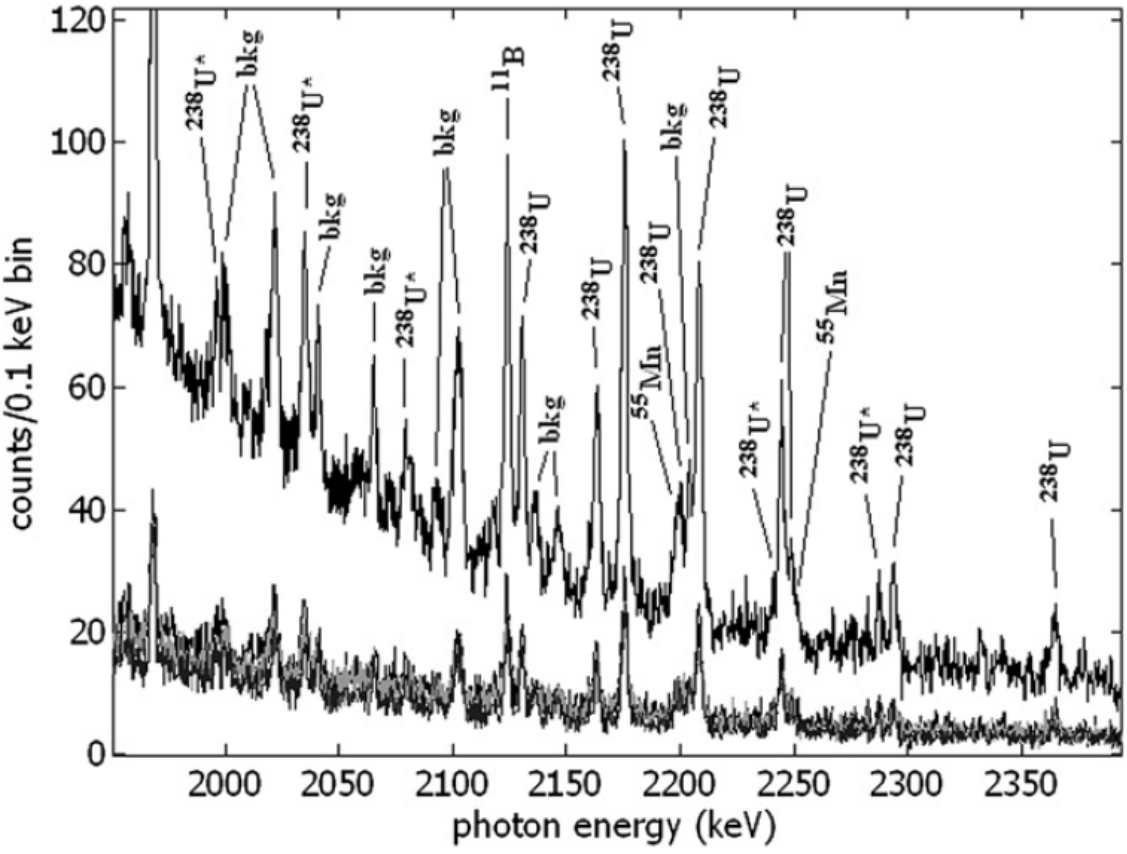

Figure 4.11: NRF transmission spectra from all detectors for a single run. Lower spectra are pre-summed while the upper spectrum is post-summing of the the lower spectra. Reproduced from Ref. [68].

present experiment demonstrates the distinct advantage monoenergetic γ-ray beams have over the continuous γ-ray beams of the previous measurements as a tool for investigating low-energy nuclear structure. Comparisons to these previously measured states will be discussed in Chapter 7.

Table 4.3: Previously known states in ^{238}U.

Energy (keV)	Γ_0 (meV)	J^π	Reference
2080	5(5)	1	[68]
2176	58(5)	1^+	[1]
	31(5)	1	[68]
2209	58(6)	1^+	[1]
	31(6)	1	[68]
2245	31(3)	1^+	[1]
	23(7)	1	[68]
2295	14(2)	1^+	[1]
	7(11)	1	[68]
2410	28(1)	1^+	[1]
	11(14)	1	[68]
2468	32(4)	1^+	[1]
	24(23)	1	[68]
2754	0.084	1	[64]
3253	0.52(19)		[62]
3809	1.6	$(1, 2^+)$	[64]
4495	0.047	$(1, 2^+)$	[64]
4592	0.28	$(1, 2^+)$	[64]
4807	0.25(1)	1	[64]
5140	0.41		[64]
5206	0.41	$(1, 2^+)$	[64]

4.2.1 National-Security Motivated Experiments

In the past five years, there has been a push for measurements of SNM within the context of shipment container interrogation. Using basic-science techniques such as NRF, hidden nuclear materials could be detected and identified inside shielded materials using

high-intensity γ rays. Since the NRF technique has been well-established in characterizing different nuclei with unique signatures, much effort has been put towards developing new detector technologies required.

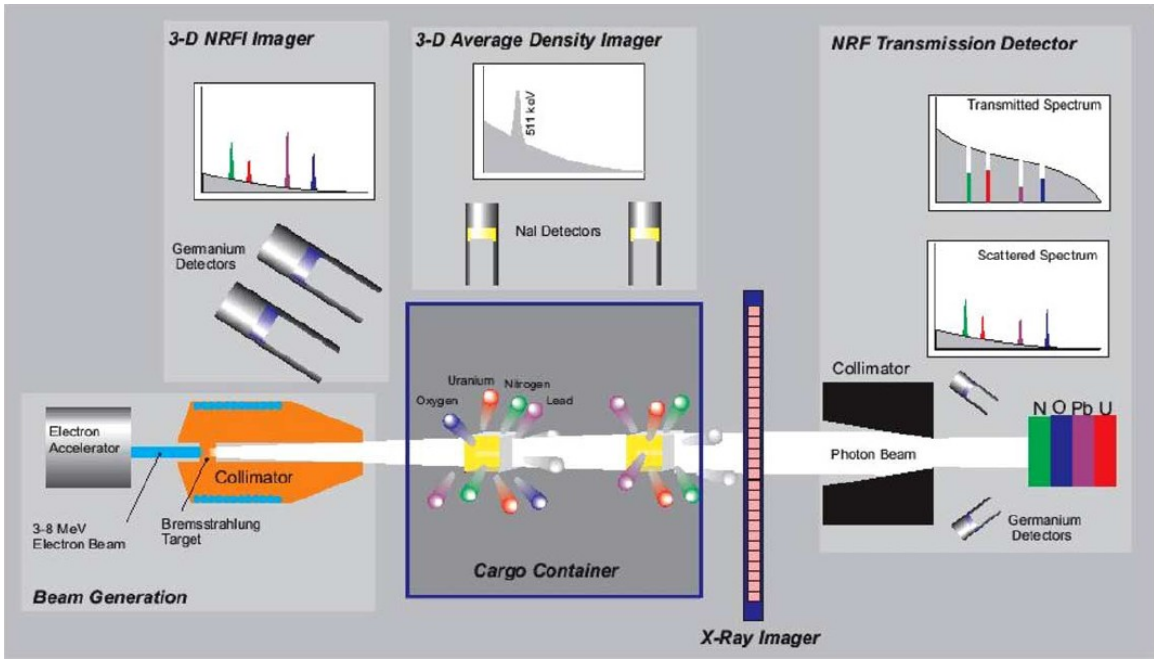

Figure 4.12: Schematic of NRF imaging.

These detectors must have good energy resolution as well as a robust design. Bertozzi *et al.* [69, 70] have produced outlines for systems which meet these specifications as shown in the schematic of Fig. 4.12. Their systems are built upon the basis of a Bremsstrahlung beam and observations of scattered γ rays in backward-angled detectors. High-intensity photon beams that are continuously distributed in energy would allow for the determination of all possible nuclei present. For example, detection of NRF signatures can differentiate signals of lead and of lead-encased uranium as in Fig. 4.13. However this depends on whether the γ rays are intense enough to penetrate the steel shipping container and the emitted NRF γ rays are intense enough to be registered in the detectors above the background of scattering

γ rays.

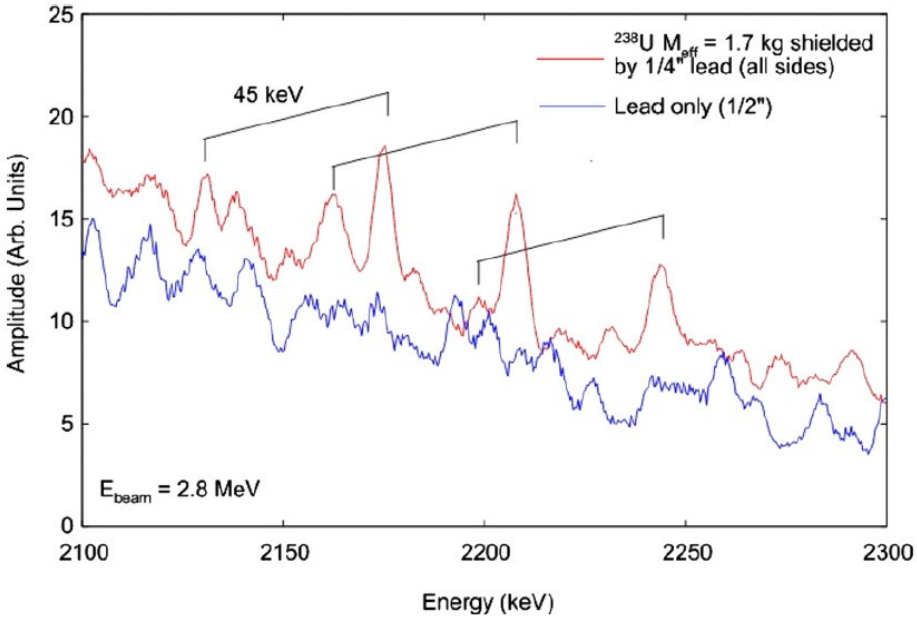

Figure 4.13: Lower NRF spectrum is of lead only while upper NRF spectrum includes both lead and uranium. Associated transitions to ground state and to the first excited state are marked. Reproduced from Ref. [69].

In order to verify the feasibility of a detection system using NRF, transmission experiments have been performed in 2009 by Hagmann *et al.* [9]. These transmission experiments (see Fig. 2.2) use an absorber which is made up of a thick SNM target to create a deficit of excited γ rays at a particular energy from the detected spectra thereby creating a "notch". This notch develops because of the preferential attenuation of γ rays near the resonant state. The width of this notch should match the width of the absorbed state. Secondary experiments were also performed, placing a scatterer target of the same SNM farther downstream in order to attempt refill of this notch. A null result of this measurement was produced in Ref. [9].

Chapter 5

Facility and Experimental Setup

5.1 The HIγS Facility

NRF measurements of deexcitations in ^{238}U were performed at the High-Intensity γ-ray Source (HIγS) facility [71] at the Triangle Universities National Laboratory (see Fig. 5.1) over the course of seven experiments totalling a little over 200 hours of useable beam time (see Table 5.1 for details).

Bunches of electrons are linearly accelerated by a 270 MeV LINAC into an 0.2-1.1 GeV electron storage ring which has a length of about 107 m and a radio frequency (RF) of about 2.79 MHz. These electron bunches go through a series of alternating electric and magnetic fields in a system called "the wigglers". The fields can be set to produce γ rays of either 100% linear or circular polarization which is important for identification of ground-state and first-excited-state transition pairs in actinide nuclei. One-hundred percent linearly-polarized photon beams were chosen for these experiments.

The electron bunch releases photons as it travels through the wigglers. This photon bunch is trapped in the optical klystron by mirrors (190-1000 nm) placed on either end

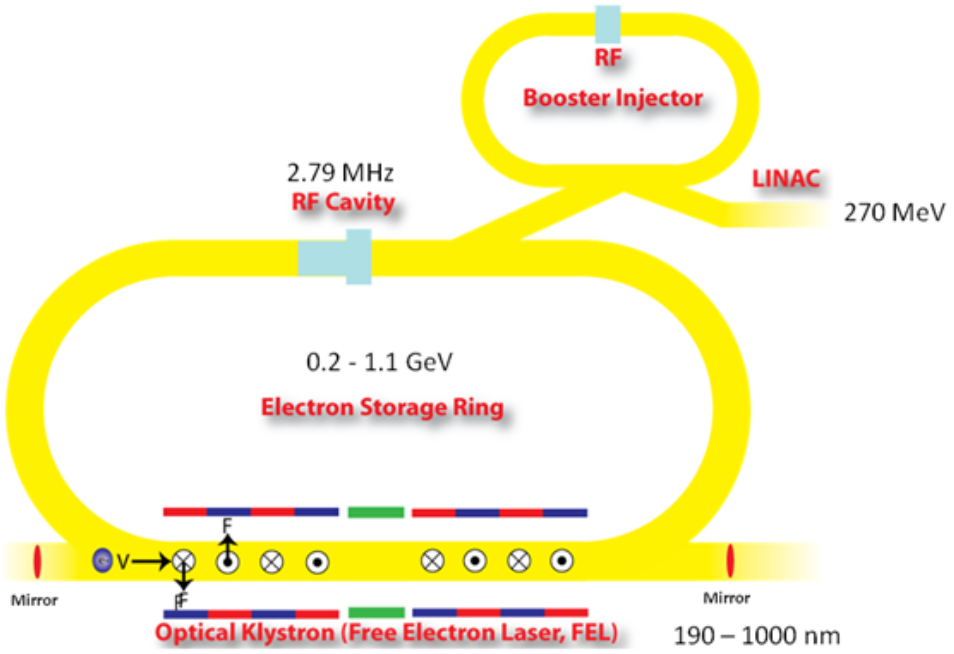

Figure 5.1: Schematic of the HIγS facility. The electron storage ring is about 107 m across its longest axis.

of the cavity. This cavity with mirrors is also known as the free-electron-laser (FEL). The length of the optical cavity is selected in such a way that the amount of time it takes the electron bunch to travel back through the wigglers a second time, it will coherently interfere with the photon bunch already in the optical cavity created in its first pass through the wigglers. The Compton backscattering of the FEL photons with electrons produces an energetic photon beam directed towards the detector setup 60 m downstream. To maintain the photon beam at the selected energy, new electron bunches are injected into the storage ring from the booster ring. Thirty γ-ray energies in the range of 2.0-6.2 MeV were used in the current experiment.

Table 5.1: Parameters of the Present Experiments. (*Note:* "H,V,B" is the number of detectors in the *horizontal*, *vertical*, and *backward-angled* orientations.) Target labels are detailed in Table 5.2.

Experiment	E_{beam} (keV)	FWHM (keV)	Unfolded E_γ (keV)	Coll. Diam. (cm)	H,V,B	Detectors	Targets	Time (h)	Beam Flux ($\times 10^6 \gamma$/s)
March 2008	2940	116	2939.0(3)	1.91	2,2,0	60%	3.1,3.2	6	2.87(9)
	3020	133	3022.2(6)	1.91	2,2,0	60%	3.1,3.2	8	2.5(1)
	3100	132	3109.3(5)	1.91	2,2,0	60%	3.1,3.2	8	2.80(9)
	3180	133	3176.1(4)	1.91	2,2,0	60%	3.1,3.2	7	3.2(1)
	3308	124	3311.1(3)	1.91	2,2,0	60%	3.1,3.2	12	2.9(1)
	3414	144	3419.7(4)	1.91	2,2,0	60%	3.1,3.2,3.3	12	2.74(5)
	3485	139	3488.0(4)	1.91	2,2,0	60%	3.1,3.2,3.3	8	2.60(7)
	4008	148	4014.4(4)	1.91	2,2,0	60%	3.1,3.2,3.3	12	6.0(2)
	4111	142	4113.0(3)	1.91	2,2,0	60%	3.1,3.2,3.3	11	6.1(2)
	4210	152	4219.7(4)	1.91	2,2,0	60%	3.1,3.2,3.3	7	3.9(1)
December 2008	2000	94	1990.5(4)	1.27	2,1,2	60%,20%	3.1,3.2	8	18.3(4)
	2125	115	2125.5(3)	1.27	2,1,2	60%,20%	3.1,3.2	4	22.6(4)
	2260	106	2254.6(2)	1.27	2,1,2	60%,20%	3.1,3.2	4	27.8(5)
	2359	121	2357.0(3)	1.27	2,1,2	60%,20%	3.1	6	29.7(7)
	2500	130	2491.5(3)	1.27	2,1,2	60%,20%	3.1	5	32.8(6)
	2616	141	2611.9(4)	1.27	2,1,2	60%,20%	3.1	6	28.4(5)
January 2009	2840	128	2836.8(2)	1.91	2,2,2	clovers,60%,20%	4.3(#1);3.2,3.3(#2)	3	11(1)
	2941	132	2934.4(2)	1.91	2,2,2	clovers,60%,20%	4.3(#1);3.2,3.3(#2)	2	8(1)
	3021	142	3022.4(2)	1.91	2,2,2	clovers,60%,20%	4.3(#1);3.2,3.3(#2)	2	9(1)
	3177	144	3177.6(2)	1.91	2,2,2	clovers,60%,20%	4.3(#1);3.2,3.3(#2)	2	10.2(2)
	3453	160	3454.5(3)	1.91	2,2,2	clovers,60%,20%	4.3(#1);3.2,3.3(#2)	3	10(1)
	3592	161	3595.8(3)	1.91	2,2,2	clovers,60%,20%	4.3(#1);3.2,3.3(#2)	5	11(1)
	3775	172	3777.6(3)	1.91	2,2,2	clovers,60%,20%	4.3(#1);3.2,3.3(#2)	5	12(2)
May 2009	4100	167	4108.9(3)	1.91	1,1,2	60%	3.2,3.3,4.3	5	6.7(4)
	4445	187	4446.0(1)	1.91	1,1,2	60%	3.3,4.3	4	14.6(8)
	4600	193	4591.6(2)	1.91	1,1,2	60%	3.3,4.3	8	2.3(2)
	4769	203	4787.6(2)	1.91	1,1,2	60%	3.3,4.3	4	1.23(6)
	4997	227	5010.2(2)	1.91	1,1,2	60%	3.3,4.3	7	1.18(6)
	5243	220	5253.3(2)	1.91	1,1,2	60%	3.3,4.3	6	1.51(9)
	5500	228	5513.4(1)	1.91	1,1,2	60%	3.3,4.3	5	1.35(7)
April 2011	5250	256	5223.1(9)	1.91	2,2,2	60%,20%	3.3,4.3	4	11.5(7)
	5450	230	5422.7(1)	1.91	2,2,2	60%,20%	3.3,4.3	4	11.3(8)
	5600	246	5566.7(9)	1.91	2,2,2	60%,20%	3.3,4.3	4	4.4(5)
	5850	246	5820.4(2)	1.91	2,2,2	60%,20%	3.3,4.3	4	9.4(8)
	6000	245	5967.8(1)	1.91	2,2,2	60%,20%	3.3,4.3	4	8.1(7)
	6150	264	6085.1(4)	1.91	2,2,2	60%,20%	3.3,4.3	5	13(2)

5.1.1 Importance of Polarized Monoenergetic Beams

As mentioned in Chapter 2, using a polarized beam is important to the study of the structure of the nuclei. With the orientation of the incident γ rays known, the target-emitted γ rays will directly produce the angular distribution of radiation without any complicated procedure involved. Just by observation alone, assignments can be made such that the state decaying by emission of γ rays in the plane parallel to the polarization plane will be assigned $J^\pi = 1^+$ (a $M1$ transition), and those decaying by emission of γ rays in the plane perpendicular to the polarization plane will be assigned $J^\pi = 1^-$ (an $E1$ transition). The selected polarization of the beam will also choose where the detectors should be oriented for the easiest method of parity assignment.

Another important feature of the present experiment is the use of monoenergetic beams which provide the ability to distinguish between ground-state and branching transitions. The width of these beams can be chosen through the selection of the size of the collimator.

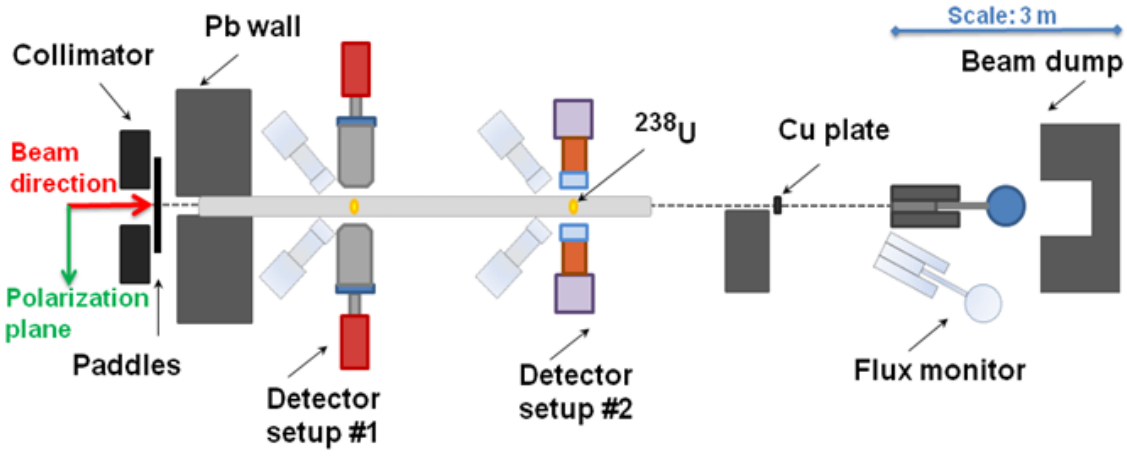

Figure 5.2: The setup for (γ, γ') experiments at HIγS (top view). Not all detectors were used during data collection at each energy. The flux monitor is shown at the Compton scattering position of 11.2°. The figure is not drawn to scale.

About 60 m from the collision point of the electrons with the FEL photons, the photon beam is shaped by an aluminum or a lead collimator. The openings of 1.27 or 1.91 cm in diameter were used in the present experiment. Collimation determines the profile. Additionally, the size of the electron bunch shapes the beam, although this is not an adjustable parameter. Collimated beams have an energy spread $\Delta E/E$ between 3 and 5%, where ΔE is the full-width half-maximum (FWHM) of the beam full energy peak. Very narrow energy distributions can be produced to probe a target thereby eliminating any doubt to whether a transition is to the ground state or to a low-lying excited state. In contrast, such characterization is more challenging in NRF spectra measured using continuous Bremsstrahlung beams, since the observed spectrum would contain all deexcitations (i.e. ground-state transitions together with feeding and branching transitions) from many different states.

Many of the previous basic-science experiments on ^{238}U, described in Chapter 4, used Bremsstrahlung beams, where characterization of transitions was certainly a problem. In heavy-mass nuclei, the significance of using monoenergetic γ-ray beams is even greater, since the density of states increases drastically with energy. Not only will the survey presented in this work extend the energy range investigated, but it will also verify the existing data on the transitions between states in the ^{238}U nucleus.

5.2 Polarimetry Detector Systems

As shown in Fig. 5.2, two detector arrays were used throughout the experiments, although most runs used only one array. The first detector array consists of four clover detectors (each with four segmented high-purity germanium (HPGe) crystals, where each

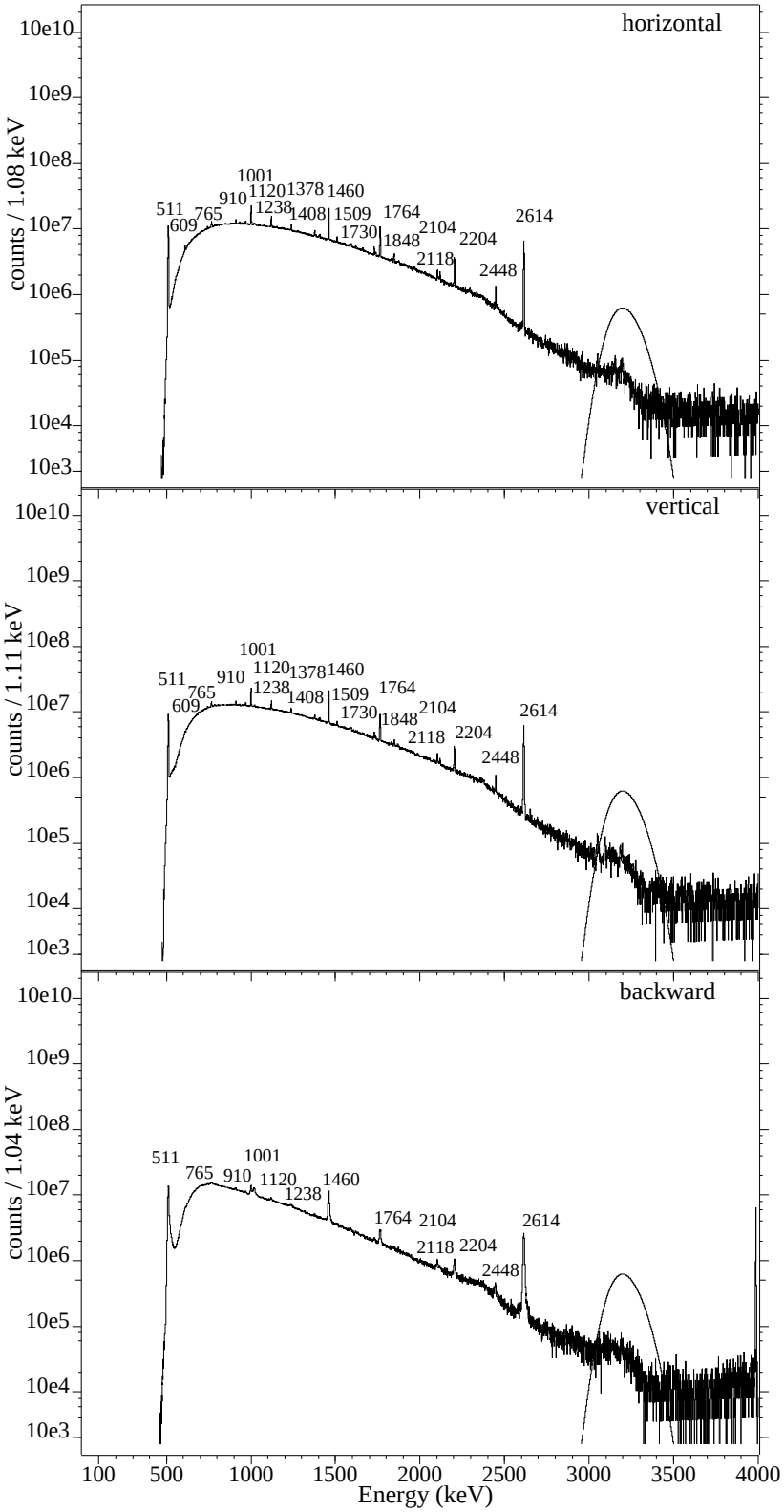

Figure 5.3: The NRF spectra from the ^{238}U target at a beam energy of 3177 keV. Spectra are shown in log scale with energy range from 100 to 4000 keV with summed data from the horizontal detectors in (a), from the vertical detectors in (b), and from the backward-angled detectors in (c). The beam profile is overlayed (solid curve) in all.

segment has ~25% efficiency relative to a 7.6 cm × 7.6 cm NaI detector). The second array consists of four HPGe detectors (each with ~60% relative efficiency). A fifth and sixth ~25% relative efficiency HPGe detectors were arranged with these two arrays as well.

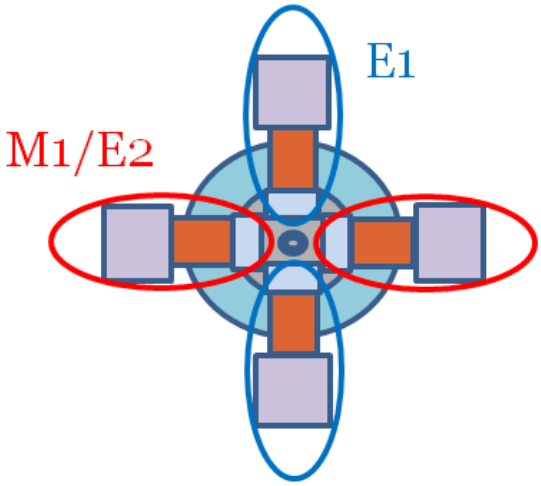

Figure 5.4: Schematic of the angular distribution of γ rays with the horizontal detectors circled in red and the vertical detectors circled in blue.

In five separate experiments, detectors were configured at six different spacial positions to measure γ rays - $(\theta, \phi) = (0, \pi/2)$, $(\pi/2, \pi/2)$, $(\pi, \pi/2)$, $(3\pi/2, \pi/2)$, $(0, \pi/4)$, and $(0, -\pi/4)$, where θ is the azimuthal angle measured from the scattering plane and ϕ is the polar angle of the outgoing radiation with respect to the linearly-polarized beam (downstream is $+\hat{z}$ axis). The detector arrays were placed downstream from the collimator and positioned around ^{238}U targets. The targets were placed inside of an evacuated plastic pipe to reduce the amount of background from small-angle scattering from the air. The clover detectors (detector setup #1) and the 60% HPGe detectors (detector setup #2) were separated by about 1.5 m. Example summed spectra spanning the entire energy range from 0 to 4000 keV are shown for each detector orientation in Fig. 5.3.

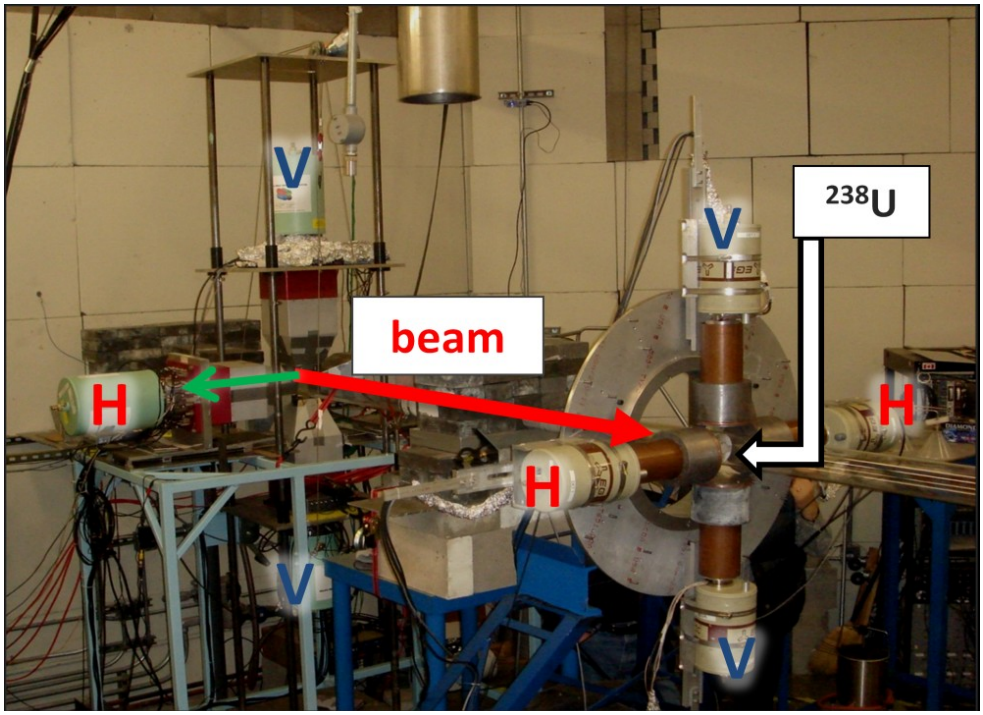

Figure 5.5: Photograph of the two HPGe detector arrays located at HIγS with horizontal (H) and vertical (V) detectors labeled. Beam direction, polarization plane, and ^{238}U target position are specified.

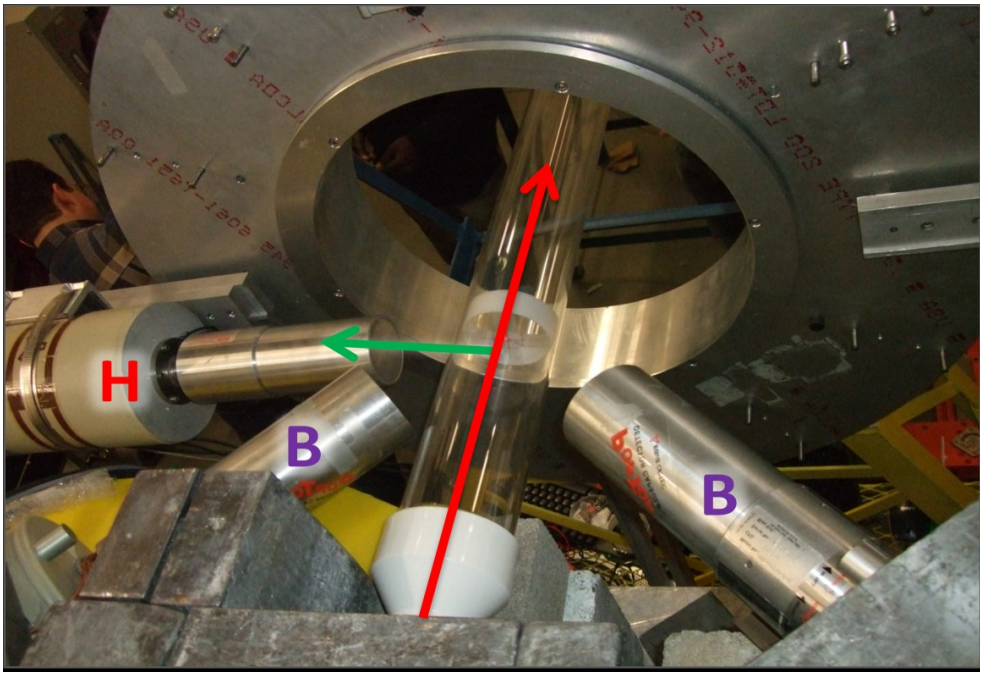

Figure 5.6: Photograph of the backward-angled HPGe detectors (B) and one horizontal HPGe detector (H) with evacuated plastic pipe and ^{238}U target shown. Beam direction and polarization plane are specified.

Unambiguous assignment of observed states is an important feature of experiments involving linearly-polarized beams since beam polarization allows for straight-forward assignment of J^{π} for excitations in even-even nuclei [72]. In the present work, γ rays corresponding to $M1$ transitions are observed predominately in the detectors placed at angles of $(0, \pi/2)$ and $(\pi, \pi/2)$ (horizontal detectors) and those corresponding to $E1$ transitions are observed in the detectors placed at angles of $(\pi/2, \pi/2)$ and $(3\pi/2, \pi/2)$ (vertical detectors). Backward detectors placed at the angles of $(0, \pi/4)$, and $(0, -\pi/4)$ were used to distinguish between $M1$ and $E2$ transitions. See the schematic of the angular γ-ray distribution for the horizontal and the vertical detectors in Fig. 5.4. Photographs of the detector arrays as well as the backward-angled detectors are shown in Fig. 5.5 and Fig. 5.6.

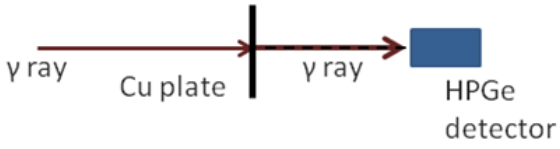

Figure 5.7: Schematic of the 110% HPGe detector for measuring the beam energy.

5.3 Flux Monitor

A large volume (110% relative efficiency) HPGe monitor detector was placed in the beam axis prior to NRF data collection to measure the energy of the photon beam (see Fig. 5.7). During the beam-energy measurement, copper-block attenuators were placed 40 m upstream from the detector setup #2 to decrease the γ-ray intensity on the detector. The spectra from these measurements were unfolded using GEANT3 [73] simulations to correct for the detector response in order to determine the beam-energy profile (see Fig. 5.8).

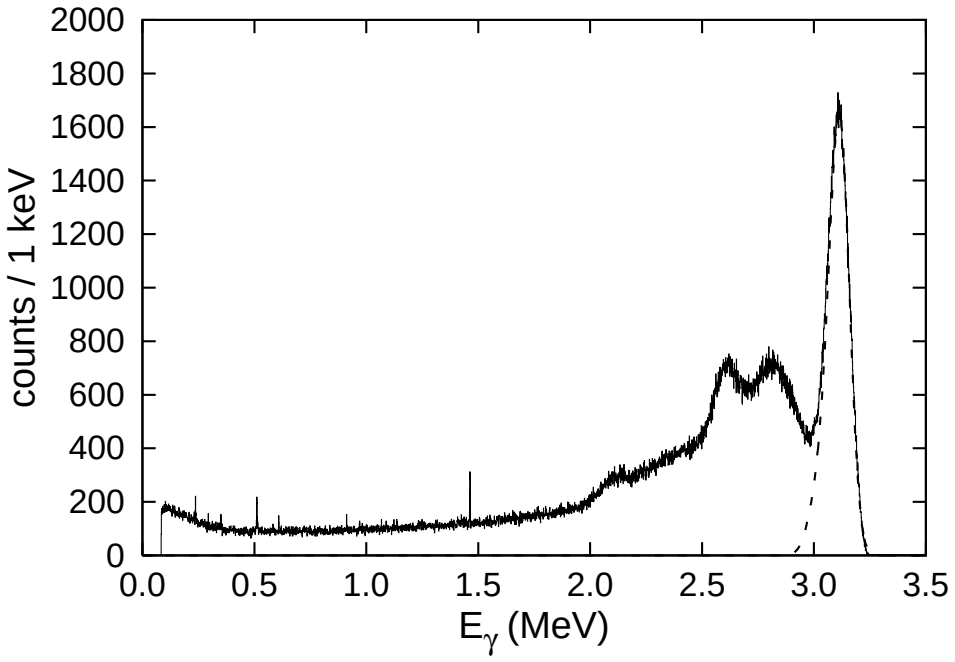

Figure 5.8: Beam-energy measurement (in histograms) with detector-response corrected beam profile overlaid (in dotted curve) for E_γ = 3.1 MeV.

After the beam-energy measurement was completed, this monitor detector was moved out of the beam path and set to an angle of either 6.2(1)° or 11.2(4)° (with respect to the beam axis) for an absolute measurement of the photon flux (see Fig. 5.9 and Fig. 5.10)). A 1.1-mm-thick copper plate was positioned directly in the beam path, about 100 cm downstream from detector setup #2 and about 151, 161, or 181 cm upstream from this flux monitor, depending on the experiment. Thus, the absolute beam flux on target was established during data acquisition for each energy using observed Compton-scattered γ rays. See Section 6.3 for details on quantitative analysis of the beam flux using this procedure.

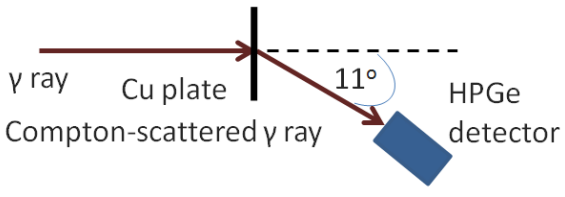

Figure 5.9: Schematic of the flux monitor for measuring Compton scattering.

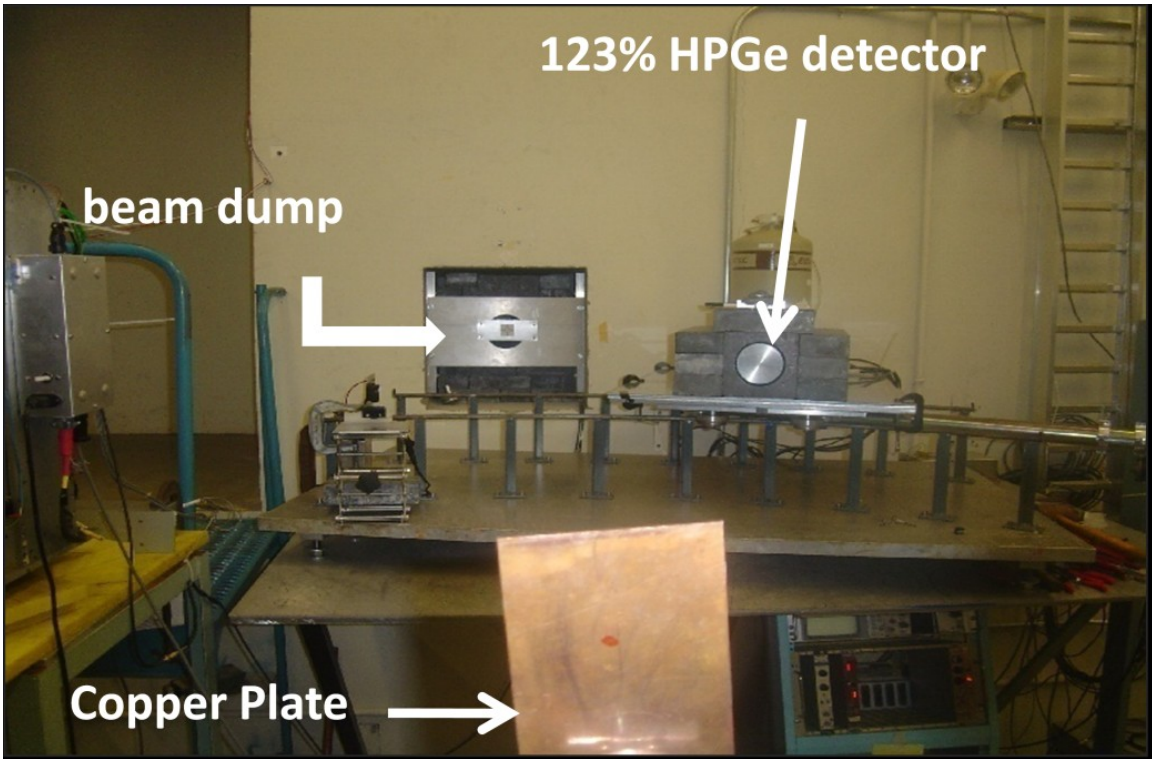

Figure 5.10: Photograph of the HPGe detector used as a flux monitor during measurements with copper plate, beam dump, and detector identified.

5.4 Target

The targets consisted of depleted uranium disks, which were about 2.50(5) cm in diameter and were enveloped within a thin, plastic sealant. One such disk is shown in Fig. 5.11. Attenuation through the plastic sealant was negligible. Each disk of uranium has a mass between 6-7 g with a thickness of about 0.16 cm (see Table 5.2 for exact values).

A target was assembled with 1, 2, or 3 disks (2.54-cm diameter) stacked together de-

Table 5.2: Masses of the ^{238}U targets.

disk label	3.1	3.2	3.3	4.1	4.2	4.3
mass (g)	6.58	6.60	6.81	6.27	6.75	6.58

pending on the flux of the photon beam and the detector dead time. This collection of sealed ^{238}U disks was housed within an evacuated plastic tube that extended ~1 m past detector setup #2. In each measurement, the photon beam spot size was smaller than the cross-sectional area of the target. The front faces of the detectors were ~10 cm away from the center of the target for both detector setup #1 and detector setup #2.

5.5 Monte Carlo N-Particle X

Monte Carlo N-Particle X (MCNPX) [74] is a particle transport code in which geometries and sources can be inputted with a selection of tallies outputted. It uses the theory of particle transport as well as a knowledge of nuclear structure and nuclear reactions to generate the requested output. It is written in Fortran and access to it is restricted by the US government. It is an extension of an earlier code MCNP by allowing all particles and energies within the simulations, provided that data exists for them within the internal reference libraries.

Figure 5.11: One slice of depleted uranium in its plastic sealant. Target diameter is 2.54 cm.

The MCNPX input file describes the geometry of the problem being assessed, defines the materials as well as the source particles, and designates what results to output from the calculation. The input file has four major sections: title, cell, surface, and data. The title section is self explanatory. The cell and surface sections define the geometry for the calculation. The data section includes commands for material, source, and tally in which cells are assigned to a particular material, source particles are defined and positioned, physical quantities are identified for tracking throughout the entire simulation, respectively. Newly compiled versions of MCNPX offer some flexibility in nuclear model and parameter selections although most of the physics implemented within the code is not available for manipulation or redefinition.

The MCNPX transport code was used to simulate the efficiencies for the summed detectors, the Compton-scattered spectra from the flux monitor, the γ-ray attenuation in the depleted uranium targets. MCNPX simulations of the efficiency are given in Chapter 6. Example input files are given in Appendix B.

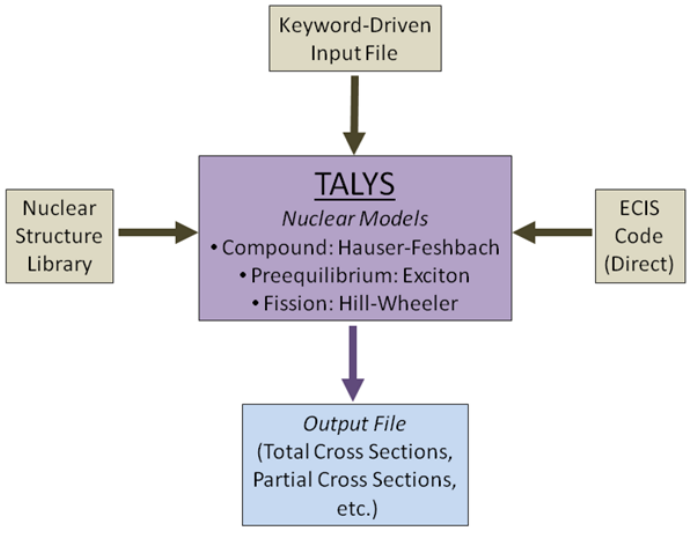

Figure 5.12: Flowchart of the TALYS model code.

5.6 Statistical Code TALYS

TALYS is a nuclear reaction program that uses a compilation of nuclear reaction models through subroutines from one source code [75]. This stand-alone statistical code assumes that paired reactions occur linearly and calculations, which abide by conservation laws, are made at each step of the reaction process. It can calculate nuclear reactions involving multiple particle types at a variety of incident energies. Nuclear structure and model parameters are executed through a built-in reference library that closely resembles the Reference Input Parameter Library (RIPL) [76]. See Fig. 5.12 for more details.

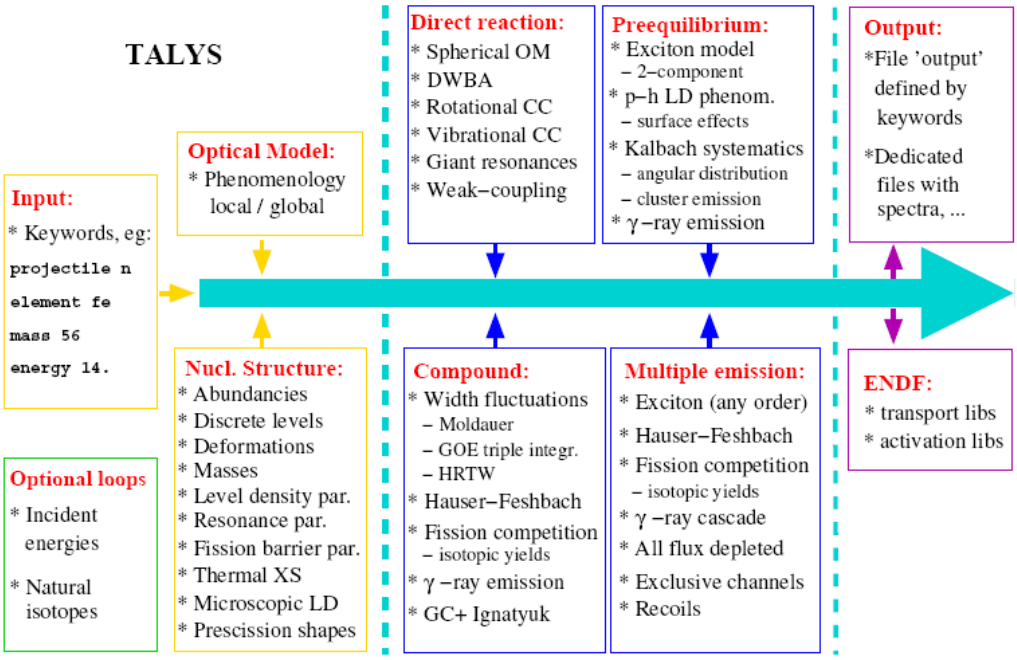

Figure 5.13: All the default assumptions of the TALYS code.

Calculating cross sections within the TALYS code framework takes a minimum input file of four parameters: target element, target mass, incident projectile energy, and pro-

jectile type. However, specific keywords can be included in this input file to exchange included nuclear models, to redefine parameter values, or to control generated output values. Adjusting these calculations with specific nuclear models or parameters can be helpful for comparisons with experimental data. For this project, compound reaction cross sections are calculated using Hauser-Feshbach formulism with a Moldauer width correction model, while γ-ray transmission coefficients follow a Brink-Axel prescription [75]. All of these choices are the default assumptions of the TALYS code as seen in Fig. 5.13.

The TALYS code was used to calculate level densities and total photoabsorption cross sections. Example input files are given in Appendix C. TALYS calculation results are compared with experimental data in Chapter 7.

Chapter 6

Data Analysis and Results

6.1 Details of the γ-Ray Spectra Measurement

Peaks in the collected γ-ray spectra were identified at first by those that had a significant number of counts above background that were distinguishable by eye. Next those that were not clearly visible by eye were only considered a peak if the peak area was above the set condition for detection limit (Discussion of the detection limit is in Section 6.4). Once peaks were identified either by primary or secondary discernment, they were fitted by the Tv code [77] using a Gaussian function with an energy-dependent width and the background was subtracted. Quantitatively, the area was determined by brute force integration from a region of interest window and also by integration of the fitted peak. Calculating both areas to be the same value within the uncertainty allows for a cross-check for the Gaussian fit as the correct function to describe the peak shape.

The summed spectra from the $^{238}\mathrm{U}(\gamma,\gamma')$ measurements in the horizontal, vertical, and backward-angled detectors are plotted in Fig. 6.1 for E_γ=2359 keV, in Fig. 6.2 for E_γ=4210 keV, and in Fig. 6.3 for E_γ=5600 keV with the respective beam profile overlayed.

It can be seen that the ground-state transitions are present within the beam-profile window while transitions to the first-excited-state can be found inside and outside of it.

Background in the observed γ-ray spectra can originate from one of the following: (1) room background, (2) radioactive decay of the target material, (3) atomic scattering, (4) coherent-scattering processes, and (5) small-angle scattering of the γ-ray beam from the collimator. These backgrounds need to be subtracted in order to determine the NRF cross sections. Room and target background can be easily identified and subtracted if they lie within the window of where NRF peaks should be located. These background lines are detailed in Table 6.1. The atomic-scattering background, which has the distribution form of a decaying exponential, as well as the "bump" produced by coherently-scattered and inelastic γ rays, upon which the NRF peaks sit, was fitted using a n^{th} order polynomial, usually with $n \leq 2$, and subtracted. Small-angle scattering of the γ-ray beam from the collimator is minimized by placing lead walls around the detectors and the collimator. Therefore, this background is considered negligible since it is on the order of the uncertainty in the counting statistics.

Natural room background peaks which were statistically significant in every spectra, namely 1460.8 keV γ-ray line (from the ^{40}K daughter) and 2614.5 keV γ-ray line (from the ^{208}Tl daughter), along with calibration sources, were used to calibrate the γ-ray energy in Tv [77] by producing a linear fit to the source peaks in order to obtain a global calibration for all of the detectors. Due to the small variations in amplifier gain between runs, individual calibrations were made to compensate for these shifts between each incident γ-ray energy.

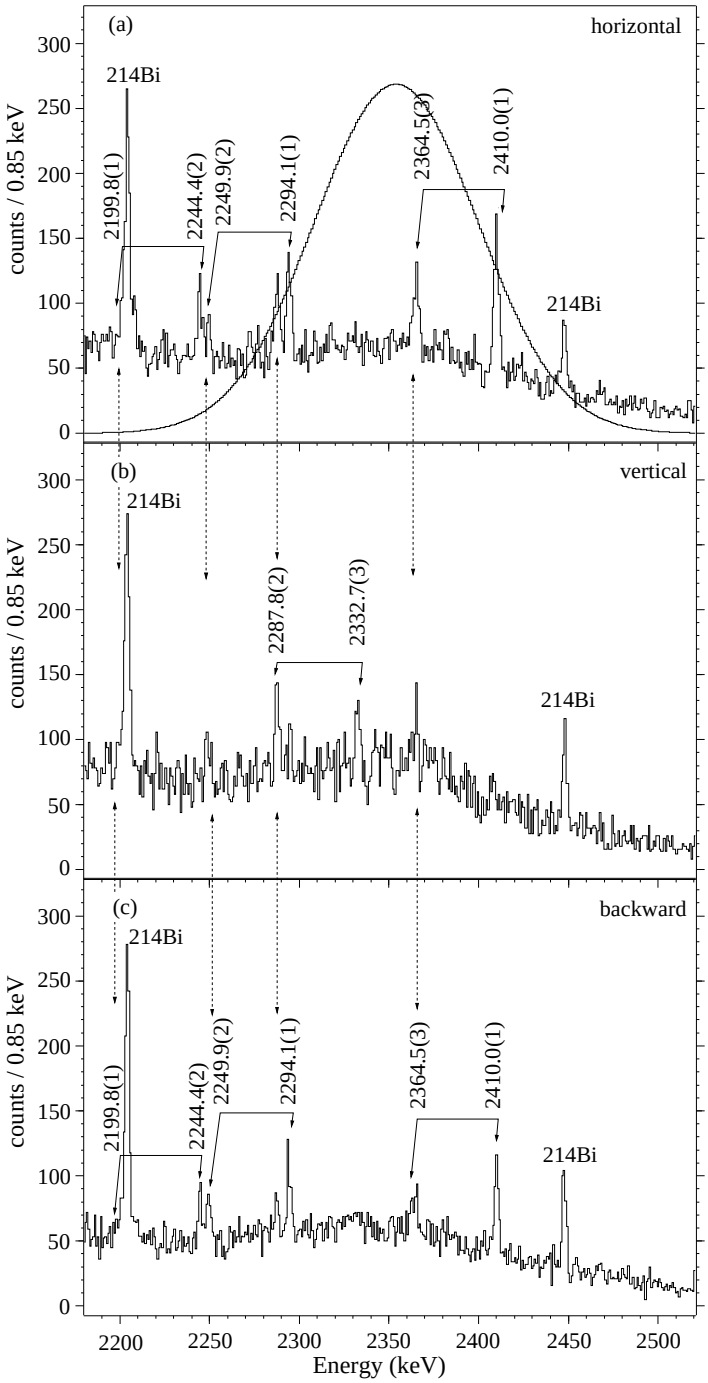

Figure 6.1: NRF spectra from a ^{238}U target using E_γ = 2359 ± 103 keV. (a) The spectrum in the horizontal detectors with the beam profile (solid curve) overlayed. (b) The spectrum in the vertical detectors. (c) The spectrum in the backward-angled detectors. Transitions to the ground state and to the first excited state are labeled with solid arrowed lines. Branchings to the first excited state are observed in multiple detectors which are denoted by a dotted line.

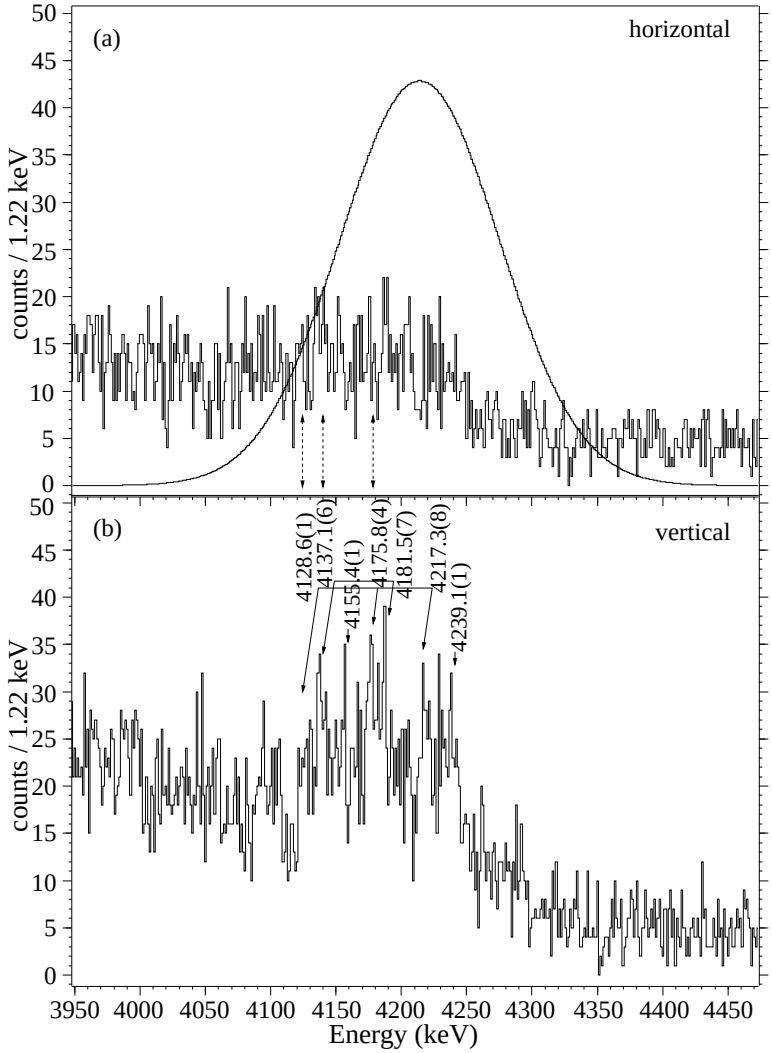

Figure 6.2: NRF spectra from the ^{238}U target at a beam energy of 4210 keV. The histograms in (a) and (b) are the same as in Fig. 6.1.

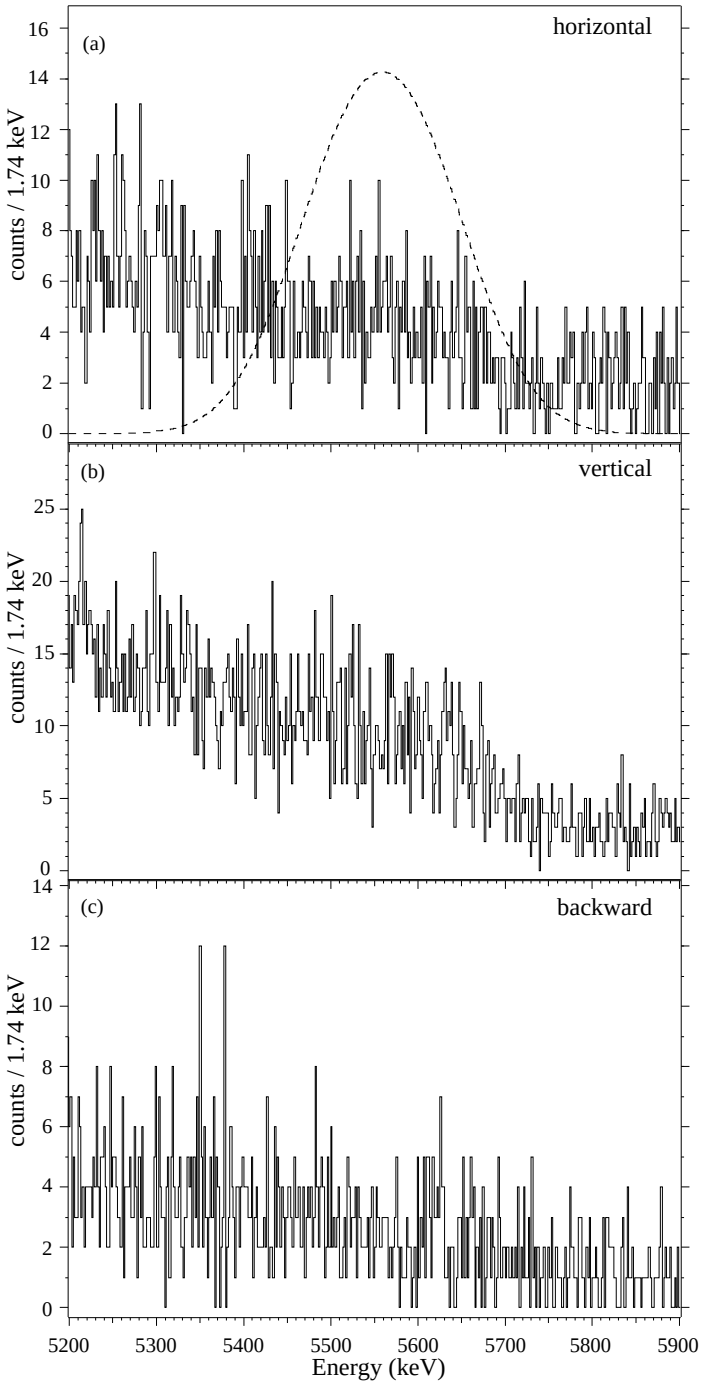

Figure 6.3: NRF spectra from the ^{238}U target at a beam energy of 5600 keV. The histograms in (a), (b), and (c) are the same as in Fig. 6.1.

Table 6.1: The room and target background observed in all detectors. SE (DE) denotes single (double) escape lines.

Energy (keV)	Origin of Line	Energy (keV)	Origin of Line	Energy (keV)	Origin of Line
75	^{212,214}Pb or ^{208}Tl *X* ray	969	^{228}Ac(β,γ)^{228}Th	1639	^{228}Ac(β,γ)^{228}Th
84	^{208}Tl *X* ray	1001	^{234m}Pa(β,γ)^{234}U	1651	^{201}Bi(ϵ,γ)^{201}Pb
92	^{234}Th(β,γ)^{234m}Pa	1063	^{207}Pb(n,n')	1654	^{234}Pa(β,γ)^{234}U
186	^{226}Ra(α,γ)^{222}Rn; ^{235}U(α,γ)^{231}Th	1120	^{214}Bi(β,γ)^{214}Po	1661	^{214}Bi(β,γ)^{214}Po
238	^{212}Pb(β,γ)^{212}Bi	1125	^{208}Tl(β,γ)^{208}Pb	1667	^{228}Ac(β,γ)^{228}Th
242	^{214}Pb(β,γ)^{214}Bi	1135	^{228}Ac(β,γ)^{228}Th	1684	^{214}Bi(β,γ)^{214}Po
295	^{214}Pb(β,γ)^{214}Bi	1138	^{201}Bi(ϵ,γ)^{201}Pb	1694	^{234}Pa(β,γ)^{234}U
338	^{228}Ac(β,γ)^{228}Th	1142	^{228}Ac(β,γ)^{228}Th	1719	^{234}Pa(β,γ)^{234}U
352	^{214}Pb(β,γ)^{214}Bi	1148	^{228}Ac(β,γ)^{228}Th	1729	^{214}Bi(β,γ)^{214}Po
463	^{228}Ac(β,γ)^{228}Th	1155	^{214}Bi(β,γ)^{214}Po	1738	^{234}Pa(β,γ)^{234}U
511	e^+e^- annihilation	1194	^{206}Pb γ ray; ^{234}Pa(β,γ)^{234}U	1751	^{214}Bi(β,γ)^{214}Po
570	^{212}Po(α,γ)^{208}Pb; ^{207}Pb(n,n')	1238	^{214}Bi(β,γ)^{214}Po	1765	^{214}Bi(β,γ)^{214}Po
583	^{208}Tl(β,γ)^{208}Pb	1246	^{228}Ac(β,γ)^{228}Th	1809	^{234}Pa(β,γ)^{234}U
609	^{214}Bi(β,γ)^{214}Po	1283	^{208}Tl(β,γ)^{208}Pb	1831	^{234}Pa(β,γ)^{234}U
691	^{234}Pa(β,γ)^{234}U	1287	^{228}Ac(β,γ)^{228}Th	1838	^{214}Bi(β,γ) ***SE***
699	^{228}Ac(β,γ)^{228}Th	1293	^{41}Ar(β,γ)^{41}K	1847	^{214}Bi(β,γ)^{214}Po
703	^{214}Bi(β,γ)^{214}Po	1353	^{234}Pa(β,γ) - ***SE***	1853	^{64}Mn(β,γ)^{64}Fe
707	^{228}Ac(β,γ)^{228}Th	1378	^{214}Bi(β,γ)^{214}Po	1863	^{234}Pa(β,γ)^{234}U
727	^{212}Bi(β,γ)^{212}Po	1385	^{214}Bi(β,γ)^{214}Po	1868	^{234}Pa(β,γ)^{234}U
733	^{234}Pa(β,γ)^{234}U	1393	^{234}Pa(β,γ)^{234}U	1875	^{234}Pa(β,γ)^{234}U
742	^{214}Bi(β,γ)^{214}Po	1401	^{228}Ac(β,γ)^{228}Th	1887	^{228}Ac(β,γ)^{228}Th
766	^{214}Pb(β,γ)^{214}Bi	1408	^{214}Bi(β,γ)^{214}Po	1894	^{234}Pa(β,γ)^{234}U
782	^{228}Ac(β,γ)^{228}Th	1414	^{228}Ac(β,γ)^{228}Th	1897	^{214}Bi(β,γ)^{214}Po
786	^{214}Pb(β,γ)^{214}Bi; ^{214}Bi(β,γ)^{214}Po	1434	^{234}Pa(β,γ)^{234}U	1906	^{228}Ac(β,γ)^{228}Th
795	^{228}Ac(β,γ)^{228}Th	1461	^{40}K(β,γ)^{40}Ar	1911	^{234}Pa(β,γ)^{234}U
806	^{214}Bi(β,γ)^{214}Po	1496	^{228}Ac(β,γ)^{228}Th	1916	^{234}Pa(β,γ)^{234}U

Table 6.1 – Continued

Energy (keV)	Origin of Line	Energy (keV)	Origin of Line	Energy (keV)	Origin of Line
817	^{228}Ac(β,γ)^{228}Th	1501	^{228}Ac(β,γ)^{228}Th	1928	^{228}Ac(β,γ)^{228}Th
826	^{214}Bi(β,γ)^{214}Po	1510	^{234}Pa(β,γ)^{234}U	1937	^{234}Pa(β,γ)^{234}U
832	^{211}Pb(β,γ)^{211}Bi	1527	^{234}Pa(β,γ)^{234}U	1970	^{36}Ar(γ,γ)^{36}Ar
852	^{234}Pa(β,γ)^{234}U	1538	^{228}Ac(β,γ)^{228}Th	2104	^{208}Tl(β,γ) - ***SE***
860	^{208,210}Tl(β,γ)^{208,210}Pb	1548	^{228}Ac(β,γ)^{228}Th	2110	^{214}Bi(β,γ)^{214}Po
881	^{206}Pb γ ray	1554	^{234}Pa(β,γ)^{234}U	2113	^{56}Mn(β,γ)^{56}Fe
883	^{208}Tl(β,γ)^{208}Pb	1558	^{228}Ac(β,γ)^{228}Th	2119	^{214}Bi(β,γ)^{214}Po
887	^{228}Ac(β,γ)^{228}Th	1571	^{228}Ac(β,γ)^{228}Th	2159	^{60}Co(β,γ)^{60}Ni
899	^{204}Pb γ ray	1580	^{228}Ac(β,γ)^{228}Th	2204	^{214}Bi(β,γ)^{214}Po
911	^{228}Ac(β,γ)^{228}Th	1583	^{214}Bi(β,γ)^{214}Po	2294	^{214}Bi(β,γ)^{214}Po
922	^{234}Pa(β,γ)^{234}U; ^{228}Ac(β,γ)^{228}Th	1588	^{228}Ac(β,γ)^{228}Th	2312	^{14}N(γ,γ)^{14}N
927	^{208}Tl(β,γ)^{208}Pb	1594	^{208}Tl(β,γ) - ***DE***	2348	^{214}Bi(β,γ)^{214}Po
934	^{214}Bi(β,γ)^{214}Po	1621	^{212}Bi(β,γ)^{212}Po	2360	^{210}Tl(β,γ)^{210}Pb
946	^{234}Pa(β,γ)^{234}U; ^{228}Ac(β,γ)^{228}Th	1625	^{228}Ac(β,γ)^{228}Th	2448	^{214}Bi(β,γ)^{214}Po
965	^{228}Ac(β,γ)^{228}Th	1631	^{228}Ac(β,γ)^{228}Th	2614	^{208}Tl(β,γ)^{208}Pb

6.2 Efficiency Calibration and Simulation

Standard calibration sources (see Table 6.2) were used to establish the absolute efficiency $\epsilon(E)$ for all the HPGe detectors up to E_γ =3.4 MeV. For the γ-ray collecting detectors, the sources were placed in the target position which was about 10 cm from any detector in this setup. The efficiency of the flux monitor was measured by attaching a calibrated ^{56}Co source to the copper plate with the flux monitor, positioned 147 cm from the source at its Compton angle [78], as described in Section 5.3.

The geometries of the detectors as well as their spacial orientations were written into MCNPX simulations [74] (see Appendix B for sample input files) which extended each efficiency curve above E_γ =3.4 MeV for all detectors. The experimental and simulated relative efficiencies of the detectors were fitted using the following exponential function,

$$\epsilon(E) = c_0\left(c_1 + \left(c_3E + \frac{c_4}{E}\right)e^{\left(c_5E+\frac{c_6}{E}\right)}\right) \tag{6.1}$$

while the clover detectors were fitted using the following,

$$\epsilon(E) = c_0\left(\left(c_1 + \frac{c_2}{E}\right) + \left(c_3E + \frac{c_4}{E}\right)e^{\left(c_5E+\frac{c_6}{E}\right)} + e^{\left(c_7E+\frac{c_8}{E}\right)}\right) \tag{6.2}$$

where c_i are fitting coefficients determined for each detector and for each experiment (see Tables 6.3 and 6.4 for experimental values). The efficiency calibration curves are shown in Fig. 6.4 for the 60% relative efficiency detectors, in Fig. 6.5 for the clover detectors, and in Fig. 6.6 for the flux monitor.

Table 6.2: Energy and intensities of the calibration sources used for efficiency measurements [79].

Source	Energy (keV)	Intensity (%)
^{22}Na	1274.5	99.9(1)
^{56}Co	846.8	99.933(7)
	1037.8	14.13(5)
	1175.1	2.24(1)
	1238.3	66.1(2)
	1360.2	4.26(2)
	1771.3	15.49(5)
	2015.2	3.03(1)
	2034.8	7.77(3)
	2113.1	0.366(6)
	2212.9	0.39(1)
	2598.4	16.96(6)
	3009.6	1.00(2)
	3201.9	3.13(9)
	3253.4	7.6(2)
	3273.0	1.78(6)
	3451.1	0.93(4)
	3548.3	0.18(1)
^{60}Co	1173.2	99.85(3)
	1332.5	99.983(1)
^{88}Y	898.0	93.7(3)
	1836.1	99.2(3)
	2734.0	0.71(7)
^{133}Ba	223.2	0.450(4)
	276.4	7.16(2)
	302.9	18.33(6)
	356.0	62.1(2)
	383.9	8.94(3)

Table 6.3: Fitting coefficients c_i for each detector type - 20 and 60% relative efficiency detectors, the clover detectors, and the flux monitor detector. Note: the distance between the source and the flux monitor is about 147 cm.

Coefficient	60% detectors	Clovers	20% detectors	Flux monitor
c_1	7.7×10^{-4}	-9.9×10^{-1}	1.7×10^{-4}	4.68×10^{-5}
c_2	0	-3.8×10^{-6}	0	0
c_3	-2.2×10^{-7}	8.1	-3.6×10^{-8}	1.02×10^{-8}
c_4	3.8	-4.9×10^{-4}	9.4×10^{1}	2.5×10^{-2}
c_5	-1.1×10^{-4}	-5.7×10^{1}	-1.3×10^{-4}	8.61×10^{-5}
c_6	-9.6×10^{2}	-3.4	-3.5×10^{2}	7.68×10^{2}
c_7	0	-8.3×10^{-7}	0	0
c_8	0	2.8	0	0

Table 6.4: Fitting coefficient c_0 for each experiment and for each orientation of the 60% detector (horizontal, vertical, and backward) as well as for the flux monitor detector.

Experiment	Horizontal	Vertical	Backward	Flux monitor
March 2008	1.15(1)	1.15(2)		0.65
December 2008	0.97(3)	1.02(4)	0.52(4)	0.65
January 2009	0.34(5)	0.32(3)	0.47(4)	0.65
May 2009	0.83(2)	0.93(1)	0.42(2)	0.95
April 2011	0.80(1)	0.85(1)	1	0.65

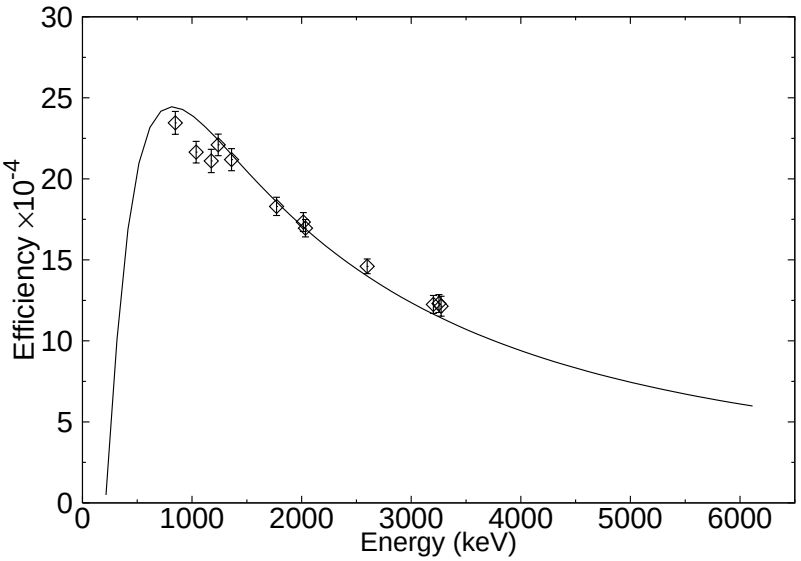

Figure 6.4: Relative efficiency measurements of the horizontal (⋄) and vertical (◆) 60% detectors at 10 cm from calibrated sources as well as the MCNPX simulated efficiency shown as the solid curve.

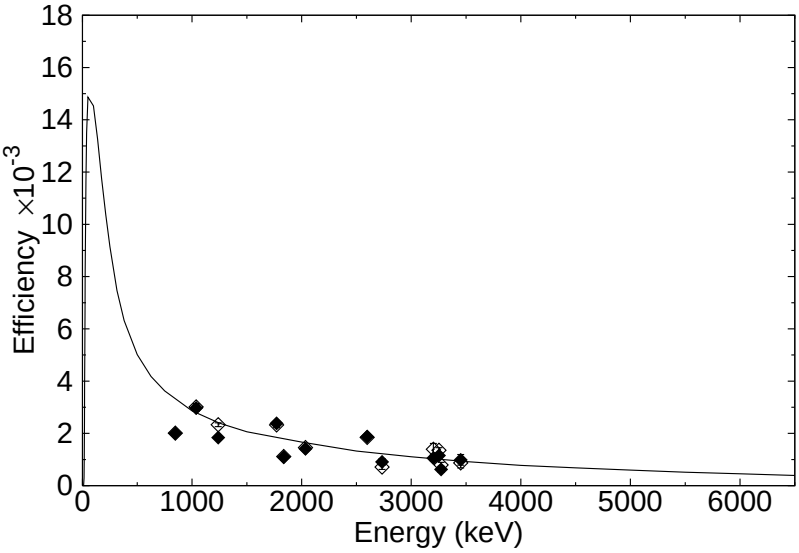

Figure 6.5: Relative efficiency measurements of the horizontal (⋄) and vertical (◆) clover detectors at 10 cm from calibrated sources as well as the MCNPX simulated efficiency shown as the solid curve.

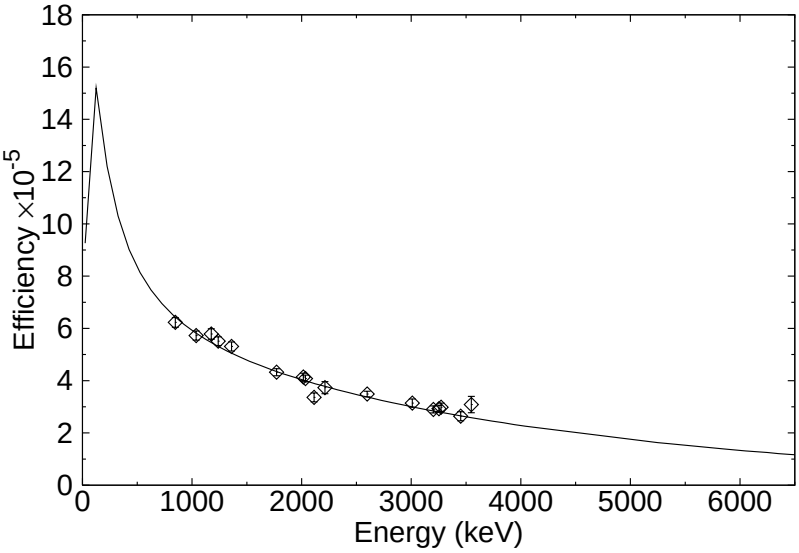

Figure 6.6: Relative efficiency of the flux detector at 147 cm from calibrated sources where the measurements are shown as (⋄) and the MCNPX simulated efficiency as the solid curve.

6.3 Beam Flux Analysis

The absolute γ-ray beam flux on target was established for each of the thirty γ-ray energies using the Compton scattered spectra collected during the measurement. To obtain the number of incident γ rays $N(E)$, the number of counts in the scattered peak N_c is normalized by the Compton-scattering cross section,

$$N(E) = \frac{N_c}{\epsilon(E)\sigma_c(E,\theta_c)n_{Cu}}, \tag{6.3}$$

where $\sigma_c(E,\theta_c)$ is the Compton-scattering cross section, θ_c is the Compton-scattering angle and n_{Cu} is the areal density of the copper atoms (see (2.25) for definition). The Klein-Nishina differential cross section for linearly-polarized γ rays is defined as follows [80, 81]:

$$\frac{\mathrm{d}\sigma_c}{\mathrm{d}\Omega} = 4\pi Z \frac{1}{2} {r_0}^2 \left(\frac{E_c}{E}\right)^2 \left(\frac{E_c}{E} + \frac{E}{E_c} - 2\sin^2\theta\cos^2\phi\right) \ . \tag{6.4}$$

The addition of the mass number Z in (6.4) accounts for use of copper as the scattering material and has a value of 29. Integration proceeds over the solid-angle geometry of the detector, with polar and azimuthal angles θ and ϕ, thereby deducing a value for σ_c. The ratio of the Compton-scattered energy E_c to the initial energy E is defined as [80, 81]

$$\frac{E_c}{E} = \frac{1}{1 + \frac{E}{mc^2}(1-\cos\theta)} \ , \tag{6.5}$$

where mc^2 is the electron rest energy, 0.511 MeV, and r_0 is the electron radius, ~2.8 fm.

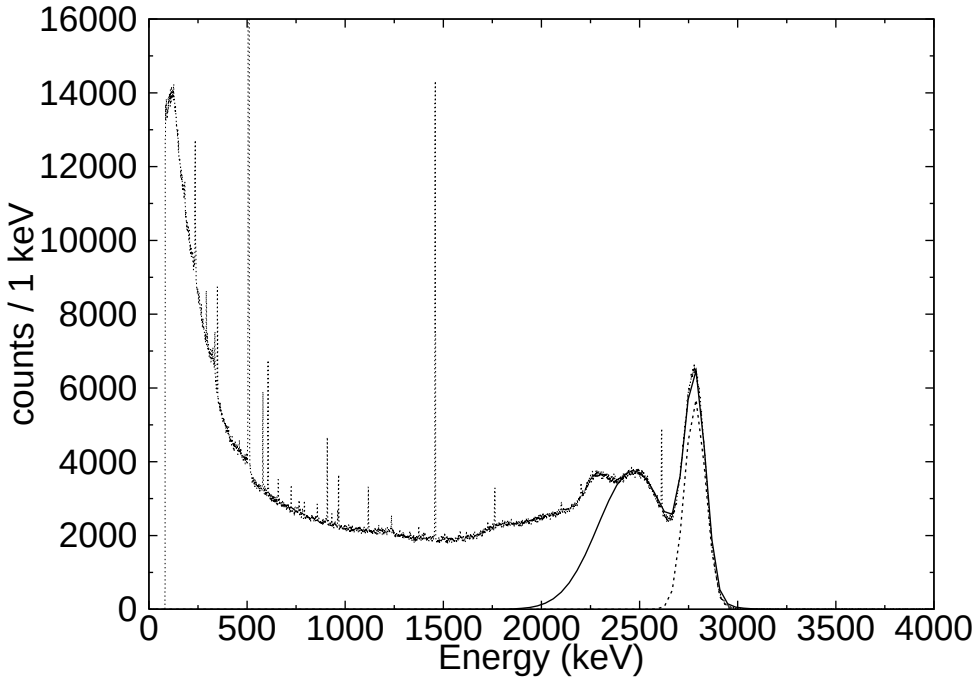

Figure 6.7: The Compton-scattered spectrum at E_γ=3100 keV is shown in the dotted histogram. Double Gaussian fits to the Compton-scattered peak and the Compton edge are shown as a solid curve. The Compton-scattered full-energy peak is extracted from this fit shown in the dashed curve.

Furthermore, the beam profile is incorporated into the calculation of $N(E)$ such that only flux exciting the specific level out of the total flux produced in the window of the beam profile is taken into account. The beam profile is fitted with a double Gaussian distribution in order to obtain the total flux in the beam-profile window, Φ_A. Next, the centroid energy and the value of the full-width half-maximum of a single transition is used to calculate the energy-weighted average flux at the center of the transition,Φ_B. A ratio of Φ_B to Φ_A gives the percentage of γ rays from the total incident beam flux that were used to excite a particular transition. Double Gaussian fits to the Compton-scattered peak and the Compton edge were also used to find N_c (see Fig. 6.7).

The intensity of the γ-rays varied between runs from $\approx$ 1.18(6)$\times 10^6$ to 3.28(6)$\times 10^7$ γ/s. The error on the beam flux is due to the counting efficiency of the detectors as well

as inaccuracy of the Gaussian fits to the Compton-scattered peak and Compton edge. To check the values of flux, resonances in ^{11}B were measured at 2.1 and 4.4 MeV. At these energies, the NRF cross sections are well known [48]. The flux value was obtained in these experiments agreed within the uncertainty with the value obtained using the Compton-scattering cross section described above.

After the flux and the detector setup have been characterized, various observables can be extracted from the data such as the integrated cross section, reduced width, branching ratio, and γ-ray strength.

6.4 Detection Limit

The recommended condition that all observed states must either be at or above a 2σ detection limit DL was used in order to assess the existence of NRF states measured in this experiment. Assuming 5% errors of both the first kind and the second kind, the detection limit is quantitatively defined as [82, 83]:

$$DL \simeq 5.4 + 3.3\sqrt{2N_B}, \tag{6.6}$$

where N_B is the integral over the background with length of 2σ such that σ is the dispersion of a Gaussian fit of the peaks observed at the same energy.

One example of the minimal detectable I_s (solid line) is shown in Fig. 6.8 as compared to the measured I_s (solid points) for E_γ = 3.1 MeV. The detection limit varies with incident beam energy, intensity, and duration of the measurement. Although a detection limit of 2σ

was chosen, many peaks that were reported from the present experiment were at or above a 3σ limit, particularly 30 out of 34 $M1$ transitions and 78 out of 90 $E1$ transitions to the ground state. Using the definition of statistical significance α_s in terms of the error function is [84]

$$\alpha_s = 1 - \mathrm{erf}\left(\frac{n}{\sqrt{2}}\right) \ , \tag{6.7}$$

where n is the number of standard deviations above the 2σ detection limit. Assuming that the likelihood of a result obtained by coincidence is $\alpha_s \leq 10\%$ and said result is thus described as ”very likely”, about seventy-one and seventy-seven percent of the observed $M1$ and $E1$ transitions, respectively, meet this criteria.

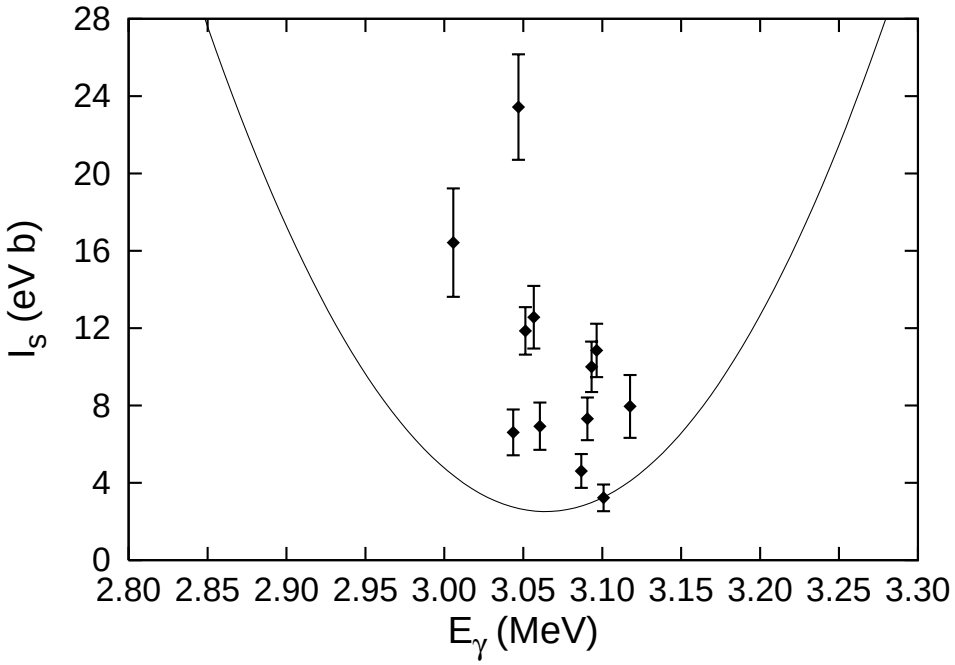

Figure 6.8: The comparison of the minimal detectable I_s with the experimental values for I_s at E_γ = 3.1 MeV. The detection limit varies with energy.

6.5 Corrections

In addition to the standard peak intensity analysis of nuclear resonance fluorescence data, there are a few corrections that need to be made for (1) the attenuation of the beam through the target either to the flux monitor or the γ-ray collecting detectors, (2) the time the detectors were not actively collecting counts (dead time), and (3) the absorption of the NRF γ rays within the ^{238}U target itself.

6.5.1 Beam Attenuation in the Target

As a beam of γ rays travels through the target a certain percentage of those γ rays will be absorbed by the target material thereby "attenuating" the beam. This is mathematically defined through the following equation,

$$N = N_0 e^{-C_{att}\rho d} = N_0 e^{-\mu d} \quad , \tag{6.8}$$

where N is the attenuated number of γ rays, N_0 is the unattenuated number of γ rays, C_{att} is the attenuation coefficient which has been tabulated in Ref. [85], ρ is the density of the target, and d is the thickness of the target. Using MCNPX (see Appendix Section B.4 for sample input file), beams of monoenergetic γ rays were simulated to interact with and without a ^{238}U target before it is counted in a γ-ray collecting HPGe detector, $\approx$10 cm away. The γ rays traveled through the target up to a maximum of the radius of the target, 1.27 cm. A second simulation calculated the interaction of a γ-ray beam as it interacts with and without a ^{238}U target as well as a copper plate before it is counted in the flux monitor detector,

≈150 cm away. Attenuation values N were determined from these MCNPX simulations for all detectors to be between 2-10%.

6.5.2 Dead Time

Natural room background peaks at 1460.8 keV and 2614.5 keV, which were present in every spectra, were also used to calculate the dead time for all of the detectors. Dead time of the data-acquisition systems for the detectors was found by comparing the rate of γ rays generating the 1460.8 keV lines in the spectra with and without beam. From this method, the extendable dead time [86] was determined to first order for detector setup #1 to be about 15-40% and for detector setup #2, the dead time varied from 10-50%. Finally, for the flux monitor the dead time was about 1-3%.

6.5.3 Self Absorption

Relative self absorption, S_a, is a correction to I_s, which depends on the Z of the target material, the photon energy, and the Doppler-broadened width of the transition. Not to be confused with the correction for attenuation of the beam through the target, the self-absorption correction adjusts the integrated cross section for the percent of NRF γ rays that are re-absorbed in the ^{238}U target before they have a chance to exit the target.

As photon energy increases, self absorption decreases. It is defined as [18]

$$S_a(d) = \frac{R(0) - R(d)}{R(0)} \tag{6.9}$$

where $R(x)$ is the count rate with ($x = d$) and without ($x = 0$) the absorbing material. For an

in depth discussion of this correction, see Appendix A. In terms of experimental parameters $S_a(d)$ reduces to

$$S_a(d) = \frac{(n_{tot}\sigma_e) + \dfrac{n_t I_s}{aE_r\sqrt{2\pi}}}{\dfrac{n_{tot}}{n_t}\dfrac{\sigma_e}{\pi^2\lambda\!\!\!^{-2}g} + b} \quad , \tag{6.10}$$

where $n_t = \frac{\chi_i}{100} n_{tot}$ (i indicates the resonant isotope) which is the number of resonant target nuclei per area, n_{tot} is the total number of nuclei per area, I_s is the integrated elastic photon scattering cross section, and b is the branching ratio Γ_0/Γ, σ_e is the total effective electronic absorption cross section, and aE_r is the resonant Doppler width.

Some assumptions were made to get Eq. (6.10) into it's final form. First, σ_e is assumed to be approximately constant or slowly varying with energy over the selected energy region which means that it is independent of E. Also, $N(E)$ is assumed to be either slow-varying or linear in E, since $N(E)$ is nearly constant over the width of the transitions described in this dissertation which are on the order of 10^{-3} eV. Finally, a first order approximation of the exponential terms is assumed.

$S_a(d)$ will have values between 0 and 1 where values closer to 0 indicate low self-absorption within the target material and values closer to 1 indicate high self-absorption. The integrated cross section I_s has to be corrected for $S_a(d)$ in any target with a finite thickness d. The extent of this S_a correction is dependent on the individual transition being assessed; The self-absorption correction $1 - S_a$ in terms of the unabsorbed NRF γ rays was between 0.43-0.20 for $M1$ transitions and 0.20-0.94 for $E1$ transitions.

Table 6.5: Systematic errors

Error Source	Error Value (%)
Detector Efficiency	3-5
Detector Geometry	1-2
Target Thickness	1-2
Beam Flux	7-10

6.6 Results

The experimental observables for NRF γ-ray transitions are presented in the following figures: integrated cross section (Eq. (2.24)) - Fig. 6.9, reduced ground-state width (Eq. (2.26)) - Fig. 6.10, experimental branching ratio (Eq. (2.27)) - Fig. 6.11, branching ratio (Eq. (2.30)) - Fig. 6.12, ground-state width (Eq. (2.31)) - Fig. 6.13, and finally, the transition strength (Eq. (2.33)) - Fig. 6.14. The systematic errors for the observed transitions are shown in Table 6.5. See Chapter 2 for details on the calculation of these values.

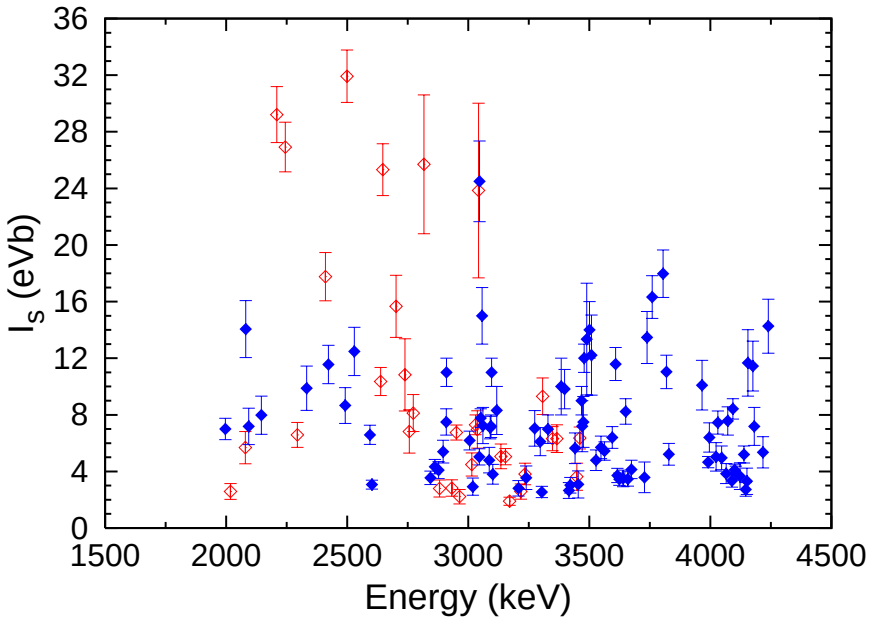

Figure 6.9: Integrated cross sections of discrete $M1$ (red ◆) and $E1$ (blue ◆) transitions.

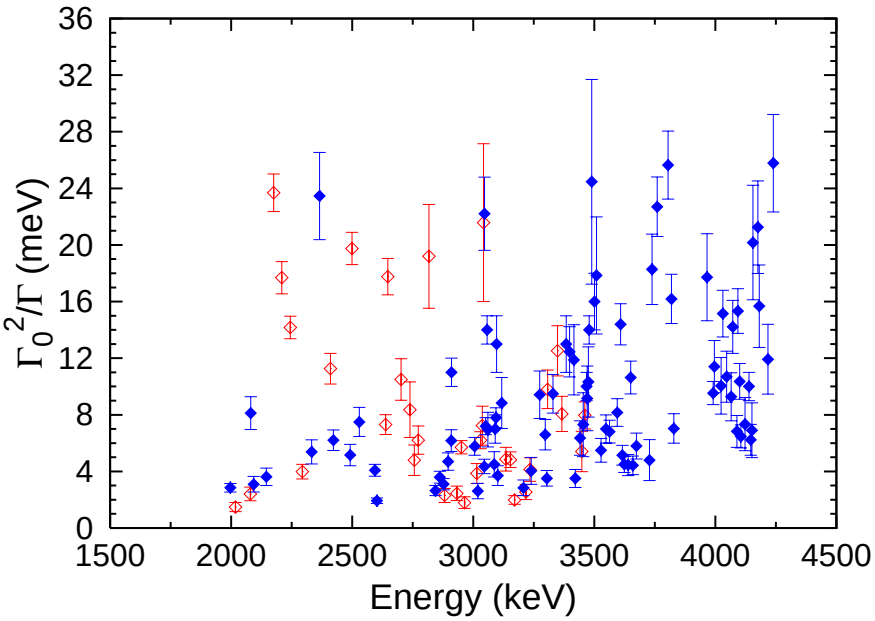

Figure 6.10: The reduced widths of discrete $M1$ (⋄) and $E1$ (◆) transitions.

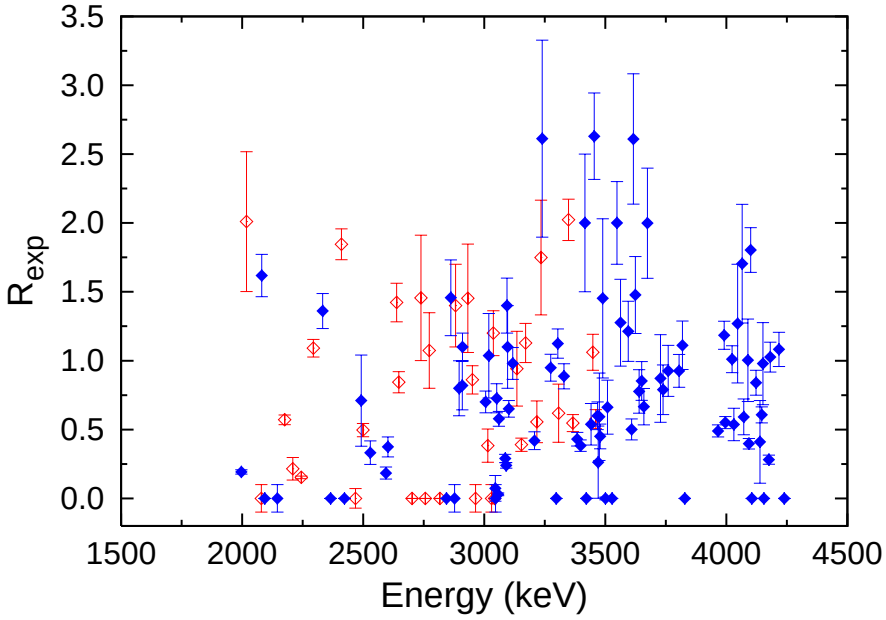

Figure 6.11: The experimental branching ratios of discrete $M1$ (⋄) and $E1$ (◆) transitions.

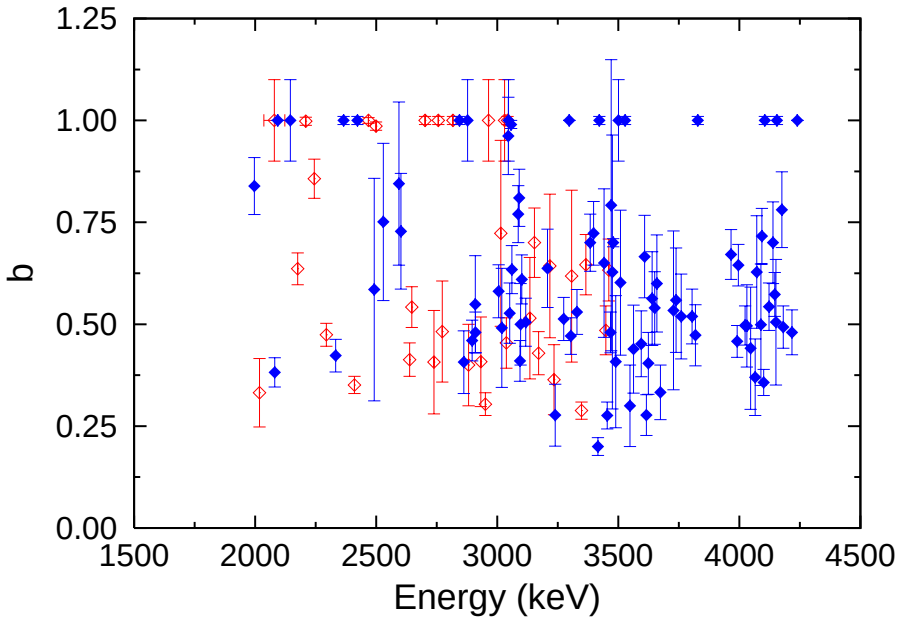

Figure 6.12: The branching ratios of discrete $M1$ (⋄) and $E1$ (◆) transitions.

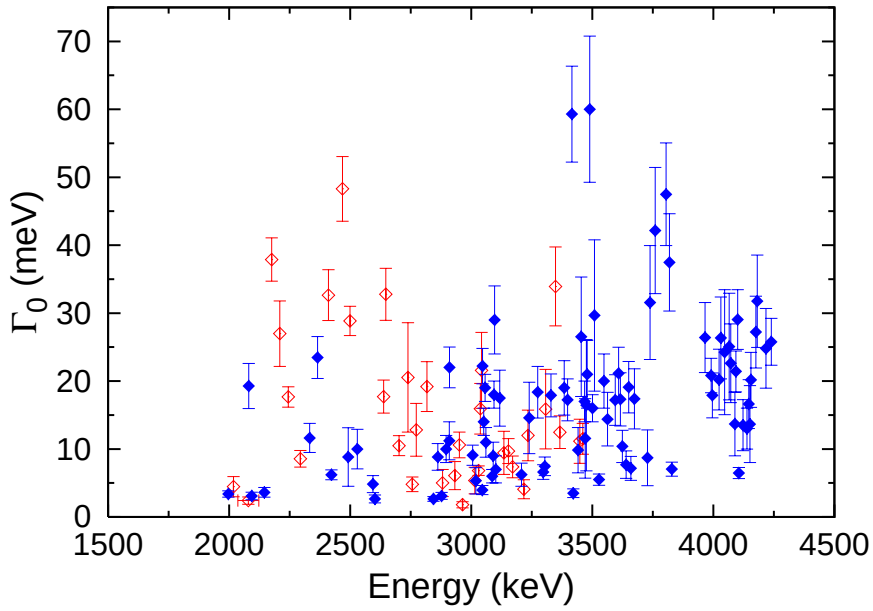

Figure 6.13: The ground-state widths of discrete $M1$ (⋄) and $E1$ (◆) transitions.

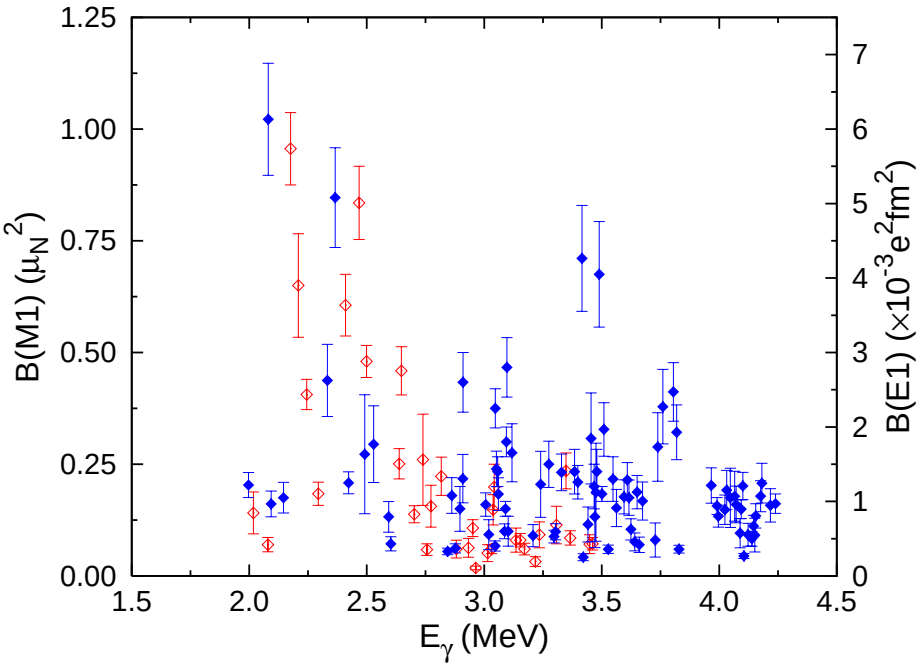

Figure 6.14: The $M1$ (⋄) and $E1$ (◆) transition strengths of discrete states.

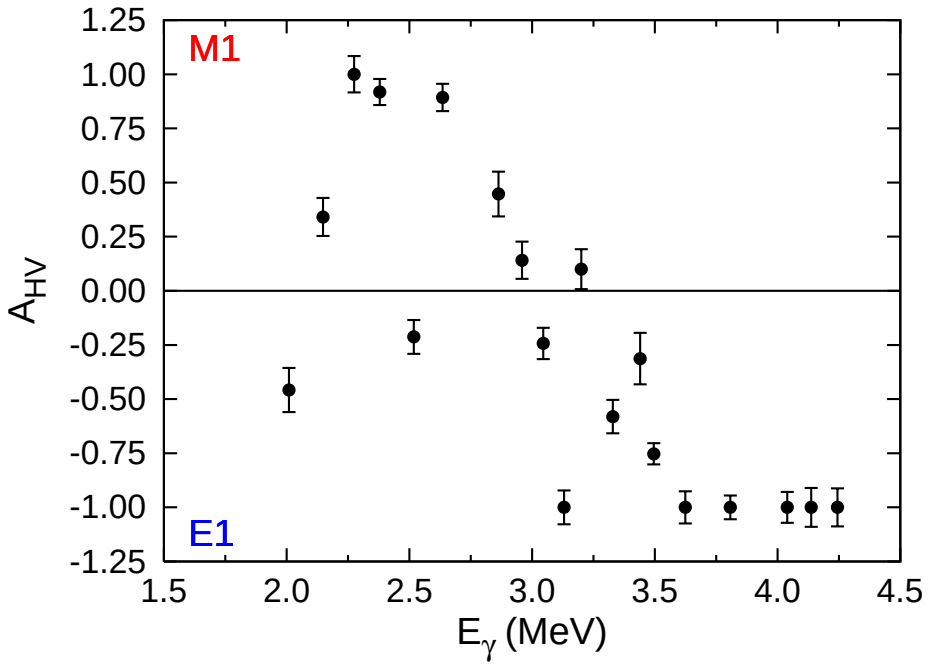

Figure 6.15: The asymmetry A_{HV} for the discrete transitions in the energy range E_γ=2.0-4.2 MeV. Each point indicates the ratio of $M1$ to $E1$ yields as a function of beam energy.

Many new discrete $M1$ and $E1$ transitions to the ground state were observed in the present experiment between 2.0 and 4.2 MeV. The ratio of the $M1$ and $E1$ transitions for each beam energy is shown as A_{HV} for discrete transitions in Fig. 6.15. Listed in Tables 6.6 and 6.7 are the measured γ-ray energies and transition strengths of 113 newly observed transitions (27 are $M1$ and 86 are $E1$) along with eight previously measured transitions (seven $M1$ [1, 68] and one $E1$ [64]). All values are shown with their statistical uncertainties.

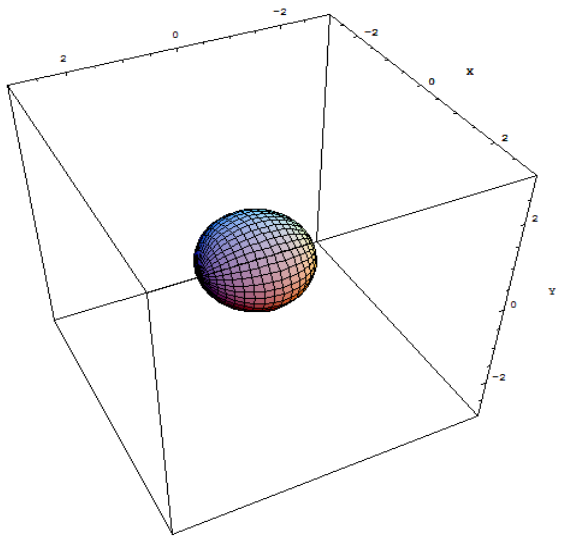

Figure 6.16: The angular distribution of a γ ray emitted through $0^+ \rightarrow 1^\pm \rightarrow 2^+$.

Most of the transitions to the ground state are accompanied by transitions to the first excited state. These transitions to the first-excited state were denoted by an almost isotropic distribution of γ rays (see Fig. 6.16) as well as an energy difference of 45 keV between transitions to the ground-state and to the first excited state (see Fig. 2.1 for level diagram). These observations provide enough evidence that they are indeed NRF from ^{238}U. However, for twenty-three of the measured states (eight $M1$ and fifteen $E1$), no accompanying transition to the first excited state is observed above the detection limit.

Table 6.6: The energy, integrated cross section, ground-state width, experimental branching ratio, γ-ray strength, and the number of standard deviations above the 2σ detection limit of the observed magnetic dipole transitions from $J^\pi = 1^+$ states in ^{238}U. Statistical errors are shown with the values.

E_γ (keV)	I_s (eVb)	Γ_0^2/Γ (meV)	R_{exp}	$B(M1)$ ($\mu_N{}^2$)	n	E_γ (keV)	I_s (eVb)	Γ_0^2/Γ (meV)	R_{exp}	$B(M1)$ ($\mu_N{}^2$)	n
2017.7(4)	2.6(6)	1.5(3)	2.0(5)	0.14(5)	1.6	2932.6(6)	2.8(6)	2.5(5)	1.5(4)	0.06(2)	1.0
2079.3(4)[a,b]	6(1)	2.4(5)	0.0(1)	0.07(2)	2.0	2951.2(3)	6.8(5)	5.7(5)	0.9(1)	0.12(2)	2.4
2175.8(3)[b]	40(2)	24(1)	0.57(3)	0.96(8)	17.3	2963.9(8)[a]	2.2(5)	1.8(4)	0.0(1)	0.02(1)	0.5
2208.8(3)[b]	29(2)	18(1)	0.22(8)	0.7(1)	4.0	3014.5(3)	4.5(8)	3.9(7)	0.4(1)	0.05(2)	1.8
2244.4(3)[b]	27(2)	14.2(8)	0.15(1)	0.41(3)	6.8	3030.6(3)[a]	7.3(7)	6.2(6)	0.0(1)	0.06(1)	5.3
2294.1(3)[b]	6.6(9)	4.0(5)	1.09(6)	0.18(3)	2.7	3037.7(3)	7(1)	7(1)	1.2(2)	0.15(3)	2.5
2410.0(3)[b]	18(2)	11(1)	1.8(1)	0.61(7)	4.0	3042.5(6)[a]	24(6)	22(6)	0.0(1)	0.20(4)	0.4
2467.8(5)[a,b]	80(8)	48(5)	0.0(1)	0.83(8)	5.1	3135.0(3)	5.1(9)	4.9(8)	0.9(3)	0.08(3)	2.2
2499.4(3)	32(2)	20(1)	0.50(5)	0.48(4)	8.8	3153.7(3)	5.0(6)	4.8(6)	0.39(5)	0.08(2)	3.6
2638.3(3)	10(1)	7.3(7)	1.4(1)	0.25(3)	10.3	3171.0(3)	1.9(3)	2.0(3)	1.1(1)	0.06(1)	2.0
2647.3(8)	25(2)	18(1)	0.84(8)	0.46(5)	20.4	3217.6(6)	2.6(5)	2.5(5)	0.6(2)	0.03(1)	0.9
2702.2(3)[a]	16(2)	10(1)	0.0(1)	0.14(2)	5.4	3234.5(7)	3.8(8)	4.1(8)	1.7(4)	0.09(3)	2.1
2738.9(9)	11(3)	8(2)	1.5(5)	0.3(1)	1.2	3307.3(3)	9(1)	10(1)	0.6(2)	0.11(4)	5.4
2756.4(3)[a,c]	7(2)	5(1)	0.0(1)	0.06(1)	1.5	3348.3(3)	6.3(8)	13(2)	2.0(2)	0.23(4)	2.9
2773.0(3)	8(1)	6(1)	1.1(3)	0.16(5)	3.6	3366.0(5)	6(1)	8(1)	0.55(6)	0.08(2)	4.0
2816.8(4)[a]	26(5)	19(4)	0.0(1)	0.22(4)	1.6	3448.3(6)	4(1)	5(1)	1.1(1)	0.07(2)	0.6
2881.4(5)	2.8(6)	2.3(5)	1.4(3)	0.06(2)	2.0	3460.7(3)	6.4(8)	8(1)	0.58(7)	0.07(1)	4.3

[a] No observed transition to first excited state.

[b] Remeasurements of previously known states.

[c] New parity assignment for previously known state.

Table 6.7: The energy, integrated cross section, ground-state width, experimental branching ratio, γ-ray strength, and the number of standard deviations above the 2σ detection limit of the observed electric dipole transitions from $J^\pi = 1^-$ states in ^{238}U. Statistical errors are shown with the values.

E_γ (keV)	I_s (eVb)	Γ_0^2/Γ (meV)	R_{exp}	$B(E1)\times10^{-3}$ (e^2fm^2)	n	E_γ (keV)	I_s (eVb)	Γ_0^2/Γ (meV)	R_{exp}	$B(E1)\times10^{-3}$ (e^2fm^2)	n
1996.7(3)	7.0(8)	2.8(3)	0.19(2)	1.2(2)	7.9	3470.7(3)	7(2)	9(2)	0.3(3)	0.8(8)	0.1
2080.7(4)	14(2)	8(1)	1.6(2)	6(1)	4.7	3475.2(3)	7(2)	10(2)	0.6(3)	1.1(7)	0.3
2093.3(4)[a,b]	7(1)	3.1(6)	0.0(1)	1.0(2)	2.8	3479.0(3)	12(1)	14(1)	0.45(9)	1.4(3)	3.1
2145.6(3)[a,b]	8(1)	3.6(6)	0.0(1)	1.1(2)	3.2	3489.0(3)	13(4)	24(7)	1.5(6)	4(2)	0.2
2332.7(3)	10(2)	5.4(9)	1.4(1)	2.6(5)	3.6	3500.5(3)[a]	14(2)	16(2)	0.0(1)	1.1(1)	6.9
2365.6(3)[a]	44(6)	23(3)	0.0(1)	5.1(7)	5.4	3509.1(9)	12(3)	18(4)	0.7(2)	2.0(7)	1.4
2422.8(3)[a]	12(1)	6.2(7)	0.0(1)	1.2(1)	6.9	3528.0(4)[a]	4.8(7)	5.5(8)	0.0(1)	0.36(5)	3.9
2491.5(5)	9(1)	5.2(8)	0.7(3)	1.6(8)	4.5	3548.0(6)	5.7(8)	7(1)	2.0(3)	1.3(3)	5.0
2529.0(3)	12(2)	7(1)	0.3(1)	1.8(5)	5.4	3562.8(3)	5.4(6)	6.8(8)	1.3(3)	0.9(2)	5.8
2593.7(6)	6.6(7)	4.1(4)	0.18(4)	0.8(2)	8.9	3594.9(5)	6.4(8)	8(1)	1.2(2)	1.1(2)	5.6
2602.5(4)	3.1(3)	1.9(2)	0.4(1)	0.4(1)	9.6	3608.7(3)	12(1)	14(1)	0.50(8)	1.3(2)	8.0
2844.2(9)[a]	3.5(5)	2.6(4)	0.0(1)	0.33(4)	4.5	3615.9(3)	3.7(5)	5.1(7)	2.6(5)	1.0(2)	4.2
2862.2(5)	4.3(5)	3.6(4)	1.5(3)	1.1(2)	6.2	3623.9(3)	3.4(4)	4.5(6)	1.5(3)	0.6(1)	4.9
2877.1(3)[a]	4.1(6)	3.1(4)	0.0(1)	0.37(6)	2.3	3640.1(3)	3.5(6)	4.5(7)	0.8(2)	0.5(1)	2.3
2896.6(3)	5.4(8)	4.4(6)	0.8(2)	0.9(3)	3.6	3650.5(3)	8.2(9)	11(1)	0.9(1)	1.1(2)	6.8
2908.9(3)	7.5(9)	6.2(8)	0.8(2)	1.3(3)	5.3	3659.7(6)	3.5(5)	4.4(7)	0.7(1)	0.4(1)	3.4
2910.0(4)	11(1)	11(1)	1.1(1)	2.6(4)	9.2	3673.7(6)	4.1(7)	5.8(9)	2.0(4)	1.0(3)	2.8
3005.9(4)	6.2(7)	5.8(6)	0.7(8)	1.0(2)	2.6	3728.0(9)	4(1)	5(1)	0.9(3)	0.5(2)	0.1
3018.9(3)	2.9(6)	2.6(5)	1.0(3)	0.6(2)	1.0	3738.5(8)	13(2)	18(2)	0.8(2)	1.7(5)	4.0
3043.6(3)	5.0(6)	4.4(5)	0.1(9)	0.40(7)	2.6	3759.9(3)	16(2)	23(2)	0.9(2)	2.3(5)	9.3
3046.9(3)[a]	5.0(6)	22(3)	0.0(1)	2.2(3)	6.5	3805.1(3)[b]	18(2)	26(2)	0.9(1)	2.5(4)	9.4
3051.7(3)	7.8(7)	7.2(6)	0.7(1)	1.4(2)	5.2	3819.0(6)	11(1)	16(2)	1.1(2)	1.9(4)	6.9

Continued on Next Page...

[a] No observed transition to first excited state.

[b] New parity assignment for previously known state.

Table 6.7 – Continued

E_γ (keV)	I_s (eVb)	Γ_0^2/Γ (meV)	R_{exp}	$B(E1)\times10^{-3}$ (e^2fm^2)	n	E_γ (keV)	I_s (eVb)	Γ_0^2/Γ (meV)	R_{exp}	$B(E1)\times10^{-3}$ (e^2fm^2)	n
3057.1(4)	15(2)	14(1)	0.03(1)	1.9(2)	2.4	3828.7(3)[a]	5.2(8)	7(1)	0.0(1)	0.36(5)	3.4
3060.6(3)	7(1)	7(1)	0.58(5)	1.1(2)	2.7	3965.7(4)	10(2)	18(3)	0.49(4)	1.2(2)	3.0
3086.7(4)	4.8(9)	4.5(9)	0.29(3)	0.6(1)	2.0	3990.7(9)	4.7(4)	9.5(8)	1.2(1)	0.9(1)	0.3
3090.6(4)	8(1)	7(1)	0.24(2)	0.9(1)	3.7	3995.8(3)	6(1)	11(2)	0.6(4)	0.8(1)	0.9
3094.2(3)	7.2(8)	7.8(7)	1.4(2)	1.8(2)	2.8	4023.7(7)	5(1)	10(2)	1.0(1)	0.9(2)	2.0
3096.4(3)	11(1)	13(2)	1.1(3)	2.8(4)	5.5	4031.4(7)	7.5(8)	15(2)	0.5(1)	1.2(3)	2.2
3101.7(4)	3.8(7)	3.7(7)	0.65(6)	0.6(2)	0.0	4046.7(3)	5.0(8)	11(2)	1.3(4)	1.0(4)	3.2
3117.7(4)	8(2)	9(2)	1.0(1)	1.7(4)	2.0	4065.3(3)	3.8(7)	9(2)	1.7(4)	1.1(3)	1.8
3207.8(4)	2.8(5)	2.8(6)	0.42(6)	0.5(1)	0.2	4072.1(6)	8(1)	14(2)	0.6(1)	1.0(2)	4.6
3239.6(3)	3.6(8)	4.0(9)	2.6(7)	1.2(4)	1.3	4088.9(7)	3.3(5)	7(1)	1.0(3)	0.6(2)	2.8
3274.4(3)	7(1)	9(2)	0.9(1)	1.5(3)	2.8	4093.4(3)	8.4(7)	15(2)	0.40(4)	0.9(1)	8.0
3297.2(4)[a]	6(1)	7(1)	0.0(1)	0.53(9)	3.4	4100.2(3)	4.1(4)	10(1)	1.8(2)	1.2(2)	5.6
3303.6(3)	2.5(4)	3.5(5)	1.1(1)	0.6(1)	2.9	4105.2(3)[a]	3.9(5)	6.5(8)	0.0(1)	0.27(3)	5.4
3329.1(6)	7(1)	9(1)	0.89(9)	1.4(2)	4.6	4122.9(5)	3.7(9)	7(2)	0.84(9)	0.6(2)	0.8
3384.3(3)	10(2)	13(2)	0.43(5)	1.4(3)	4.0	4138.9(7)	5.2(6)	10(1)	0.41(7)	0.5(1)	3.8
3397.9(8)	10(1)	12(2)	0.38(4)	1.3(2)	4.6	4145.8(3)	2.7(5)	6(1)	0.6(6)	0.7(1)	0.3
3416.0(4)	2.7(6)	12(2)	4.0(4)	2.0(5)	1.8	4151.3(6)	3.3(9)	7(2)	1.0(3)	0.5(2)	0.5
3421.5(5)[a]	3.0(6)	3.5(6)	0.0(1)	0.25(5)	2.7	4155.4(3)[a]	12(2)	20(4)	0.0(1)	0.8(2)	1.1
3441.0(9)	6(1)	6(1)	0.5(2)	0.7(2)	1.4	4175.8(4)	11(2)	21(3)	0.28(3)	1.1(2)	3.4
3454.1(4)	3(1)	7(2)	2.6(3)	1.8(6)	0.0	4181.5(7)	7(1)	16(3)	1.0(1)	1.2(3)	1.9
3467.8(6)	9(1)	10(1)	0.6(1)	1.2(3)	5.3	4217.3(8)	5(1)	12(2)	1.1(1)	0.9(2)	1.1
						4239.1(3)[a]	14(2)	26(3)	0.0(1)	1.0(1)	5.6

[a] No observed transition to first excited state.
[b] New parity assignment for previously known state.

Chapter 7

Discussion of the Results

In the following sections, the characteristics of the observed discrete dipole excitations as well as of the continuum will be discussed. A comparison to previous experiments on $140 < A < 180$ and actinide nuclei as presented in Chapter 4 is addressed in their relation to the current experiments. The QRPA model described in Chapter 3 is also compared with the current experiment.

7.1 Comparison to Previously-Known ^{238}U States

Since the lower energy range studied by this dissertation also covers those investigated by the previous experiments, comparisons can be made between the features of these overlapping energy ranges. Notably the most significant difference is the absence of the $M1$ transition at $E_\gamma = 3253$ keV ($\Gamma_0 = 0.52(19)$ meV) [62, 64] which was not observed above the detection limit in this experiment. The uncertainty of another previously measured $M1$ transition, originally with a width of $\Gamma_0 = 5(5)$ meV [68], is reduced in the present work to 2.4(5) meV. A $M1$ transition measured originally at $E_\gamma = 2754$ keV with $\Gamma_0 = 0.08$ meV [64] was observed in this experiment at 2756 keV with the new width of $\Gamma_0 = 5(1)$ meV.

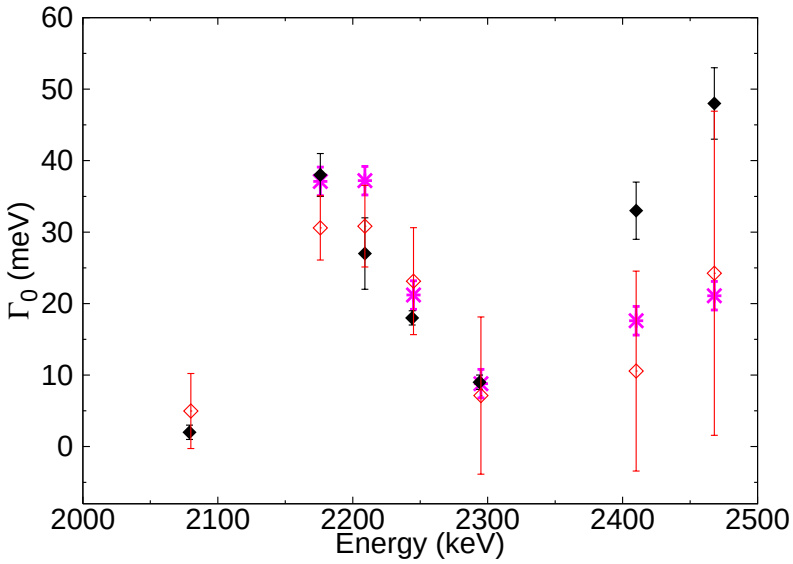

Figure 7.1: The ground-state widths of the present experiment (◆) compared with those from Heil *et al.* [1] (∗) and Quiter *et al.* [68] (⋄).

The $M1$ transition at 2287 keV [68] is reassigned by the present work as a transition to the first excited state of the $E1$ transition at 2332 keV. Previously measured $E1$ transitions at E_γ = 3809 keV with Γ_0 = 1.6 meV [64] as well as E_γ = 4217 keV with Γ_0 = 1.6 meV [65] are assigned new widths of Γ_0 = 41(7) meV and 25(6) meV, respectively. The ground-state widths from previous measurements of Heil *et al.* [1] and Quiter *et al.* [68] are compared with those from the present experiment in Fig. 7.1.

7.2 Magnetic Dipole Excitations

In the present measurement, $M1$ excitations are observed at incident energies in 2.0 <E_γ <3.5 MeV range with a strong concentration of $M1$ states observed around 2.5 MeV. As E_γ increased, the $M1$ strength decreased until no more discrete states (above the detection limit of about 3 eVb) are observed above 3.5 MeV. The upper limit of the integrated cross section of a $M1$ transition to the ground-state between 3.5 MeV <E_γ <4.2 MeV is estimated to be

<1 eVb. For incident-beam energies in the range of 2.0-4.3 MeV, $\Sigma B(M1)$ is found to be 8(1) $\mu_N{}^2$ with mean excitation energy ω_{M1} of 2.6(6) MeV for the observed $M1$ transitions.

The observed $M1$ strength may include states from both the scissors mode and the spin-flip mode, which are indistinguishable from each other based solely on the use of the NRF technique. A combination of theoretical models and experimental data from reactions other than (γ,γ') are needed for firm identification.

The authors of Ref. [1] used a reformulation of the two-rotor model [87, 88] and determined the mean excitation energy (in MeV) of the scissors mode to be,

$$\omega_{M1} = \left(\frac{A^2}{4NZ}\frac{26A^{4/3}\delta^2}{\mathcal{I}_\pi + \mathcal{I}_\nu}\right)^{1/2} \approx \left(\frac{26A^{4/3}\delta^2}{\mathcal{I}_\pi + \mathcal{I}_\nu}\right)^{1/2} \simeq 42|\delta|A^{-1/6} \quad , \tag{7.1}$$

where $\mathcal{I}_\pi$ ($\mathcal{I}_\nu$) is the moment of inertia for protons (neutrons) and is assumed to be a rigid body in order to make the approximation. For ^{238}U, where $\delta = 0.234$, the mean excitation energy ω_{M1} calculated with this model is 2.03 MeV, which is lower than the experimental value. For rare-earth nuclei, the ω_{M1} increases to ~3 MeV. The interacting boson model (IBA-2) [89] was used to determine the transition strength for the scissors mode,

$$B(M1)\uparrow = \frac{3}{4\pi}\frac{8N_\pi N_\nu}{2\,(N_\pi + N_\nu) - 1}\,(g_\pi - g_\nu)^2 \quad , \tag{7.2}$$

where N_π (N_ν) is the valence proton (neutron) boson number and g_π (g_ν) is its corresponding boson gyromagnetic factor. Using bare boson parameters, $g_\pi - g_\nu = 1$, $B(M1)$ is 13 $\mu_N{}^2$. However with the average g-factors given in Ref. [90] ($g_\pi = 0.65$ and $g_\nu = 0.08$), $B(M1)$ is reduced to 4.2 $\mu_N{}^2$.

About two-thirds of the $M1$ strength found in the present measurement is observed in between 2 and 3 MeV, doubling the previous experiment's value [1] of 3.2 $\mu_N{}^2$. The observed strength is also about twice of the value measured for the rare-earth nuclei [38] as shown in Fig. 7.2. The "sum rule" by Enders *et al.* puts the range of the scissors mode between 2 and 3 MeV and predicts a strength of 5.0(8) $\mu_N{}^2$ which agrees with the strength of 6.1(9) $\mu_N{}^2$ observed in the present work within the same energy range. These authors suggest that even though there is a possibility of scissors mode strength lying outside the region specified, it would only be a small fraction and no larger than the inherent uncertainty on the strength itself.

Using the energy range of 2-3 MeV of the sum rule presented by Enders *et al.* [38], ω_{M1} is determined for ^{238}U to be 2.4(4) MeV, which is close to the ω_{M1} observed in ^{232}Th of 2.5 MeV [14]. It is smaller than the observed scissors mode ω_{M1} for many rare earth nuclei which is usually found at ~3 MeV for the energy range of 2.4-3.7 MeV [38]. Similar to Eq. (7.2), the phenomenological relation of the strength to the nuclear deformation is given by Lo Iudice and Richter [91] such that,

$$B(M1)\uparrow = 0.0042\omega A^{\frac{5}{3}}\delta^2\,(g_\pi - g_\nu) \quad , \tag{7.3}$$

where $g_\pi - g_\nu$ is approximated by $^{2Z}/_{A}$. If the mean excitation energy ω of the scissors mode is 2.4 MeV, then the $B(M1)\uparrow$ is 3.02 $\mu_N{}^2$ which is, again, about half of the strength observed in the range of 2-3 MeV.

The remaining ~2.6 $\mu_N{}^2$ of the total $M1$ strength observed at energies above the scissors mode range is about one-half of the value found in similarly deformed rare-earth nuclei

[40], and only one-fifth of the spin-flip strength measured by a (p,p') experiment [39]. One should note that the calculation of Ref. [92] for ^{238}U extends the scissors mode energy range to 4 MeV and pushes the spin-flip mode above 5-6 MeV. Due to the lack of any definitive theoretical models and the lack of comparison with data from the (e,e') reaction over the same energy range, it can not be established which prediction is correct.

7.3 Electric Dipole Excitations

Most of the $E1$ transitions observed are above 3 MeV. As E_γ increased, the number of $E1$ states and the $E1$ strength increased due to the increasing proximity of the GDR. Multiple concentrations of states centered around the energies 3.1, 3.5, and 4.1 MeV are observed. For the energy range of 2.0-4.2 MeV, the observed $\Sigma B(E1)$ is 110(30) $\times 10^{-3}$ $e^2\text{fm}^2$ with ω_{E1} of 3.3(8) MeV. For comparison, the $E1$ strength found in similarly deformed ^{154}Sm is 53 $\times 10^{-3}$ $e^2\text{fm}^2$ [57], which is a factor of 2 smaller than the strength in ^{238}U.

The enhanced $E1$ strength above the extrapolated GDR tail could arise from octupole deformations or from α-clustering, two mechanisms discussed by Iachello in Ref. [32] (see Section 2.3). Using values for the quadrupole and octupole deformation parameters from RIPL-2 [76], the octopole deformation $E1$ strength $B(E1)_{oct}$ was deduced to be $16\times 10^{-3} e^2\text{fm}^2$ (see Section 2.3.2). On the other hand for α-clustering, in order to reproduce the experimental $E1$ strength in ^{238}U in the energy range between 2 and 3 MeV, the amplitude must be $\eta = 0.12$ which gives an $E1$ strength of $B(E1)_\alpha \approx 31 \times 10^{-3} e^2\text{fm}^2$ (see Chapter 2 for details on calculating the strength from octupole scattering and α clustering). A value significantly greater than 10^{-3} for η would denote a large amount of states mixing

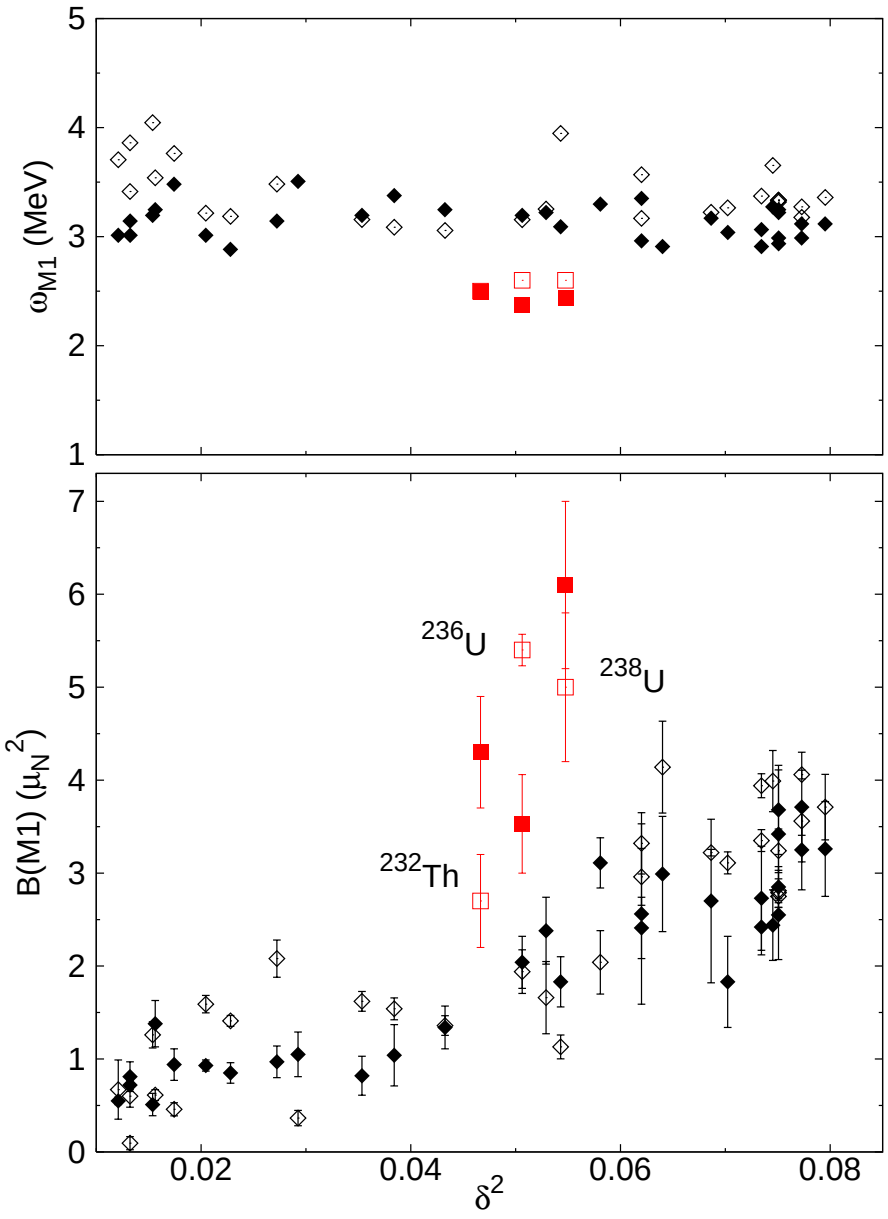

Figure 7.2: The mean excitation energy and the transition strength observed between 2-3 MeV for nuclei with $140 < A < 180$ and the actinides. The sum-rule prediction of Ref. [38]is in (◊) while the experimental data is in (◆) for rare-earth nuclei. For the actinides, the sum-rule prediction is in (□) while the experimental data is in (■). The present experimental value for $B(M1)$ within the energy range corresponding to the scissors mode is shown for ^{232}Th [14] and ^{238}U.

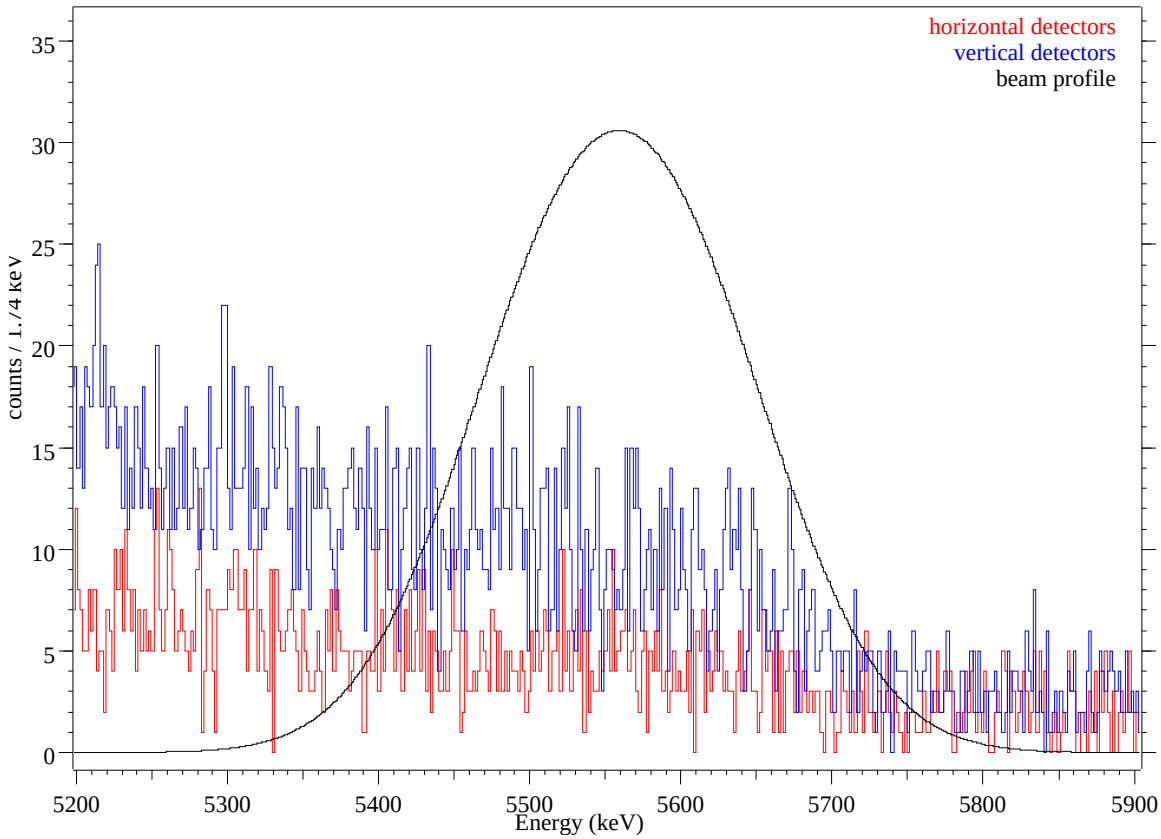

Figure 7.3: The γ-ray spectrum, observed in the horizontal detectors (red) and in the vertical detectors (blue), of E_γ=6000 keV with the beam profile overlayed. The integration window of 1 sigma is shown.

into the ground state.

With less than half of the observed $E1$ strength assigned to those two mechanisms, the rest of the observed $E1$ strength could be produced by the low-energy tail of the GDR. To evaluate this GDR-tail influenced strength, the NRF cross section is extracted from the continuum between 2.0-6.2 MeV. Assuming that only ground-state transitions would appear on the right-hand side of the beam profile, an integration window is created at each beam energy. This window started at E_{beam} and then extended one standard deviation toward the high-energy side of the beam profile, thus excluding all transitions to the first excited state (see Fig. 7.3). The incident γ-ray flux, associated with this window, is used

Table 7.1: Modified double Lorentzian GDR fit parameters using the present data and data from Ref. [42].

	First Peak		
	E_r (MeV)	σ_r (mb)	Γ_r (MeV)
Ref. [42]	10.78	315.9	2.39
Present work + Ref. [42]	10.85 (4)	344 (10)	3.0 (1)
	Second Peak		
	E_r (MeV)	σ_r (mb)	Γ_r (MeV)
Ref. [42]	13.81	455.5	5.08
Present work + Ref. [42]	14.04 (5)	430 (7)	4.9 (2)

to produce the total cross section values. An average R_{exp}, weighted by the $E1$ strength, is extracted from Table 6.7 to be 0.96(23). This value is used to determine the cross sections of the integration window.

The average total γ-ray interaction cross section σ_{tot} for $E1$ transitions is calculated using the methods from Ref. [64, 93]. For a zero-spin ground state and a dipole excitation, the ratio of the elastic scattering cross section to σ_{tot} is 0.67(16) with no other reaction channels open except the photon scattering one. The quantity σ_{tot} is corrected for coherent scattering involving the following processes: Rayleigh scattering [22], nuclear Thomson scattering, Delbrück scattering [21, 26], and coherent nuclear resonance scattering [27]. Table 2.2 from Chapter 2 lists the coherent scattering contribution at selected beam energies used during this experiment.

To evaluate the energy dependence of the $E1$ cross section, both a modified double Lorentzian (MLO) and a standard double Lorentzian (SLO) functions were used to fit the ^{238}U(γ,*tot*) data of Ref. [42] which included both photoneutron and photofission reaction cross sections. The strength function $\vec{f}_{MLO}(E)$, measured in MeV^{-3}, with free parameters

describing the energy E_r, the amplitude σ_r, and the width Γ_r, is of the following form [76]:

$$\vec{f}_{MLO}(E) = \frac{8.7 \cdot 10^{-8} E}{1 - e^{-\frac{E}{T_f}}} \sum_{i=1}^{2} \frac{\sigma_{r,i} {\Gamma_{r,i}}^2}{\left(E^2 - {E_{r,i}}^2\right)^2 + \left(E\,\Gamma_{r,i}\right)^2} \,, \tag{7.4}$$

where T_f is the final state temperature which can be approximated by the effective temperature T_{eff} of the target [18] such that it is ~1.2 MeV for the MLO fit to the data of Ref. [42]. The strength function for the SLO fit is similar to Eq. (7.4), but does not include the exponential term. See Table 7.1 for values of the fit parameters. The total cross section σ_{tot} is calculated from

$$\sigma_{tot} = 3\,(\pi\hbar c)^2\, E \vec{f}_{MLO}(E) \,. \tag{7.5}$$

The results are shown in Fig. 7.4: the σ_{tot} for $E1$ transitions from the present work, the experimental ^{238}U(γ,γ') cross section data from 4.9-6.2 MeV [66], the experimental ^{238}U(γ,*tot*) cross section data [42], as well as the MLO and SLO fits to the GDR data of Ref. [42].

In the present work, a large amount of $E1$ cross section was observed between 2.0 and 6.1 MeV to be a summed total of 394(78) mb. However, it is very similar to the summed cross section produced from the MLO fit to the GDR, which has a cross section of about 400 mb in the same energy range. This observation is illustrated in Fig. 7.4 where σ_{tot} from the present work follows the MLO and SLO fits. It must be concluded that no evidence is seen in the present data for the presence of a PDR in ^{238}U. Furthermore, this is the only analysis to date in which the existence of a PDR has been analyzed in the actinides.

Using the statistical code TALYS [75], the strength above and below the GDR was

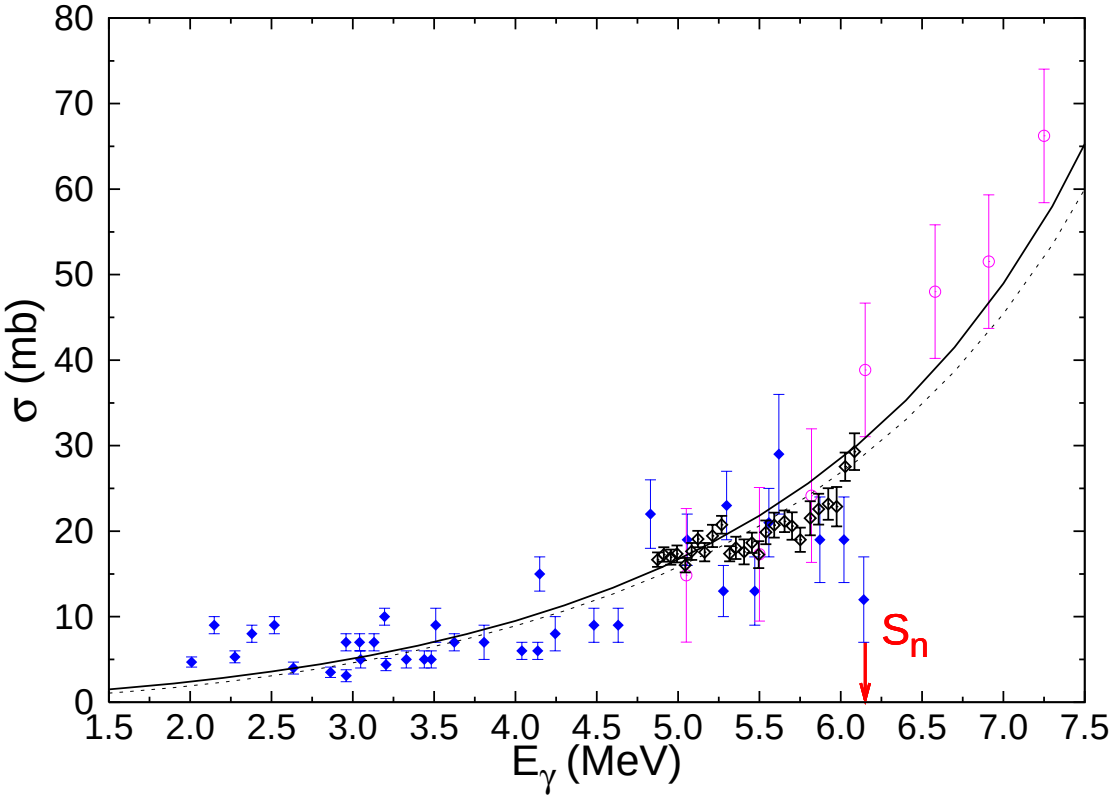

Figure 7.4: The average of the total γ-ray interaction cross section for $E1$ transitions from the discrete and unresolved transitions of the present work (◆) compared with experimental ^{238}U(γ,γ) cross section data [66] (◇), and with ^{238}U(γ,tot) cross section data [42] (○). MLO fit (solid curve) and SLO fit (dashed curve) to the GDR [42, 76] is also shown.

modeled with and without including a PDR around the neutron separation energy S_n, using the parameters from the MLO fits. The back-shifted Fermi gas model was chosen to calculate the level density. In order to include a PDR into the model, another Lorentzian-shaped contribution was added to the Brink-Axel strength function [75]. This modeled PDR was arbitrarily centered around S_n = 6.15 MeV with a strength of 13 mb and a width of 1 MeV. The TALYS results, with and without a PDR included, are shown in Fig. 7.5, along with the experimental ^{238}U(γ,γ') cross sections from the present work and the experimental ^{238}U(γ,tot) cross sections [42]. Again, the TALYS calculation verifies that even a PDR with a small intensity does not fit the intensity of the current results for ^{238}U.

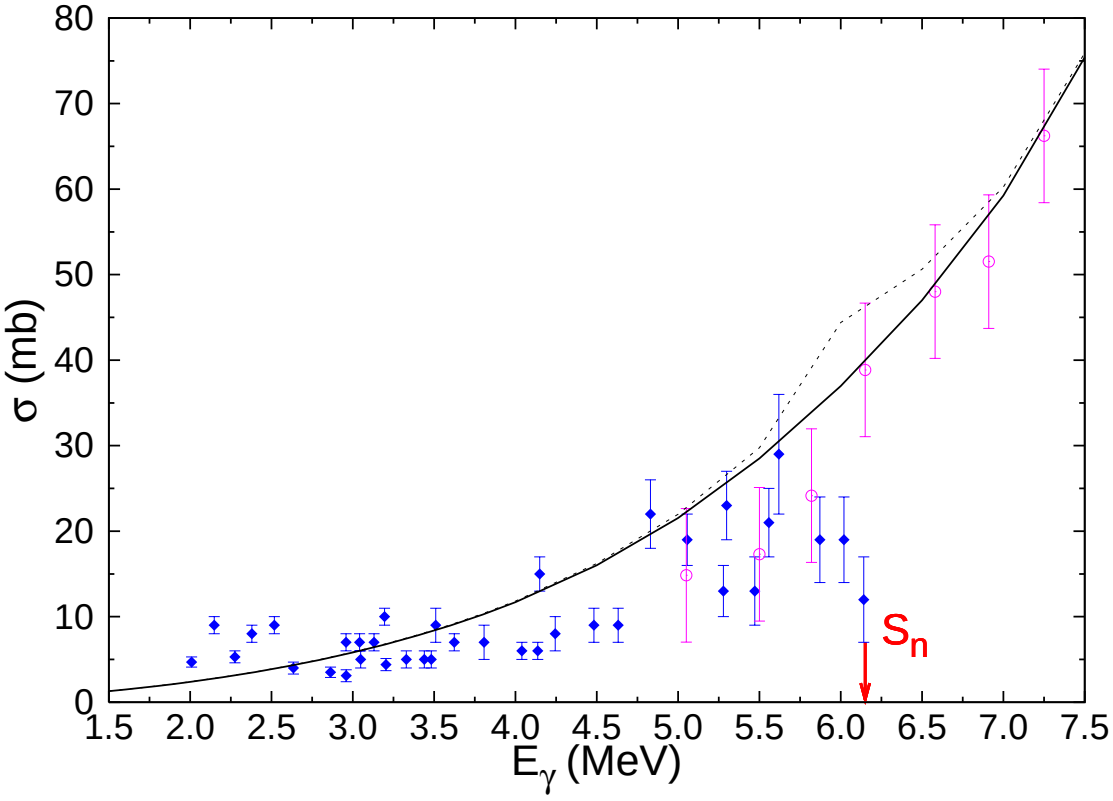

Figure 7.5: Total γ-ray interaction cross section for $E1$ transitions from the present work (◆) compared with the ^{238}U(γ,tot) cross section data [42] (○). TALYS models of the GDR (solid curve) and including one PDR around S_n (dashed curve) are also shown.

7.4 Continuum of States

Above E_γ=4.2 MeV, the level density becomes too high to observe individual excited states and only the strength of the continuum can be observed. Using ΔE = 50 keV energy bins around the beam energy centroid E_{beam} within a $E_{beam} \pm 2\Delta E$ window (see Fig. 7.6), an asymmetry profile $\bar{A}_{HV}$ was calculated for each beam energy and the results are shown in Fig. 7.7. Recall from the discussion of A_{HV} in Chapter 2 that the average asymmetry $\bar{A}_{HV}$ is not only a relative asymmetry between the horizontal and vertical detectors but it is also weighted by the I_s in order to compare $\bar{A}_{HV}$ across all energies in the present experiment.

In addition to removing the fitted background within each spectrum, all known room-

background peaks are also subtracted from the spectra at energies below 2.7 MeV. Between 2 and 3 MeV there is a lot of positive-valued $\bar{A}_{HV}$ bins which could denote the presence of the scissors mode. As the beam energy increased, $\bar{A}_{HV}$ decreased, indicating increasing $E1$ strength and decreasing $M1$ strength. This effect is expected, given that there is an increasing presence of the GDR through its low-energy tail. However, when the γ-ray energy starts to approach 4 MeV, the intensity of $E1$ radiation returns to a level where it resembles the intensity of $M1$ radiation. This could be due to the presence of the spin-flip mode, which is observed to be between 4-8 MeV [39]. However, $\bar{A}_{HV}$ bins are primarily on the negative side of zero, which could demonstrate the significance of the GDR as a mode of greater intensity. In general, most of the $\bar{A}_{HV}$ values are within ±0.1 of zero, indicating

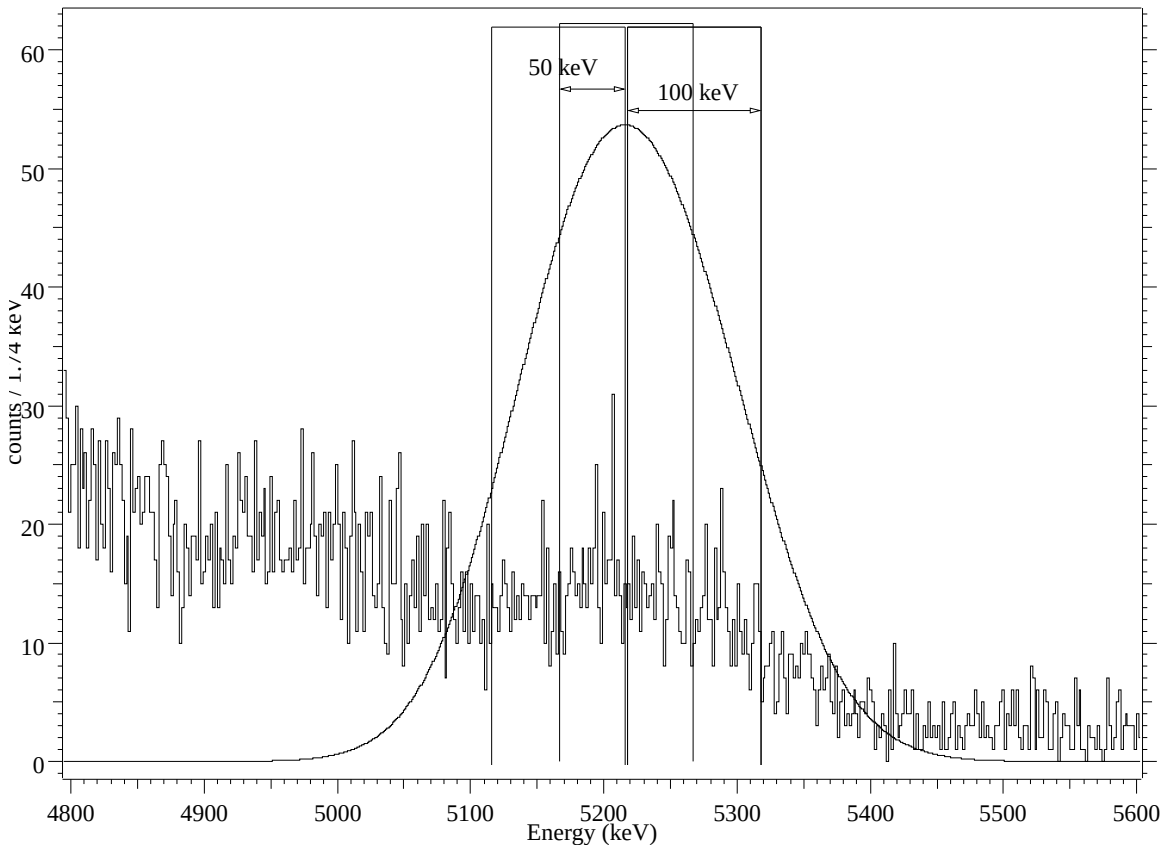

Figure 7.6: The γ-ray spectrum, observed in the vertical detectors, of E_γ=5250 keV with the beam profile overlayed. The integration windows of 50 keV and 100 keV are shown.

$M1$ and $E1$ transitions have a similar population frequency in the low-energy range as well as similar excitation energies.

7.5 Comparison to $140 < A < 180$ Nuclei

7.5.1 Comparison of R_{exp} for $140 < A < 180$ Nuclei with the Actinides

For the deexcitation of both dipole states, the Alaga selection rules [19] give $R = ½$ for $K = 1$ states and $R = 2$ for $K = 0$ states as discussed in Section 2.1.2. A value for R which lies between these Alaga values implies that there is K-mixing between the $M1$ and $E1$ transitions. For the rare-earth nuclei, Zilges *et al.* [94] compiled the R_{exp} values of about 170 levels and plotted the frequency distribution of these ratios. These results are shown in Fig. 7.8. Two maxima, one at $R = ½$ and one at $R = 2$, are observed, thus showing that a

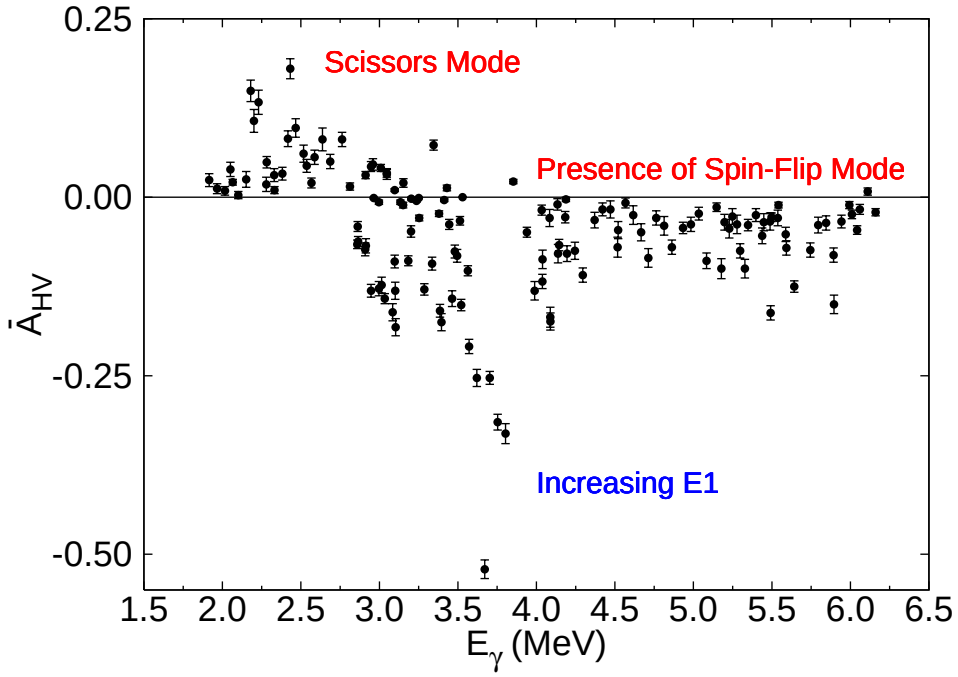

Figure 7.7: The I_s-weighted asymmetry $\bar{A}_{HV}$ of the discrete and unresolved transitions for all 30 incident beam energies. Each point corresponds to a 50-keV wide energy bin.

large fraction of transitions observed in the rare-earth nuclei follows the Alaga rules.

For comparison, the nonzero R_{exp} values of about 150 levels from ^{232}Th [14], ^{235}U [78], ^{236}U [54], ^{238}U [37], and the present work are collected and the results are shown in Fig. 7.8. The most prominent distinction between the rare-earth and the actinide nuclei is the missing maximum of $K = 0$ states in the actinide data, which could be explained by the large amount of $M1$ strength observed at low energies in the actinides. Due to the selection rules, states with $K = 0$ are only observed with $E1$ transitions. However, in the current experiment on ^{238}U, there is a significant amount of $E1$ strength present which suggests that there should be a greater amount of $K = 0$ states present than what was observed. In both the rare-earth and the actinide nuclei, there is a large number of transitions with R_{exp} values between ½ and 2. This is may be evidence of the K-mixing which is known to

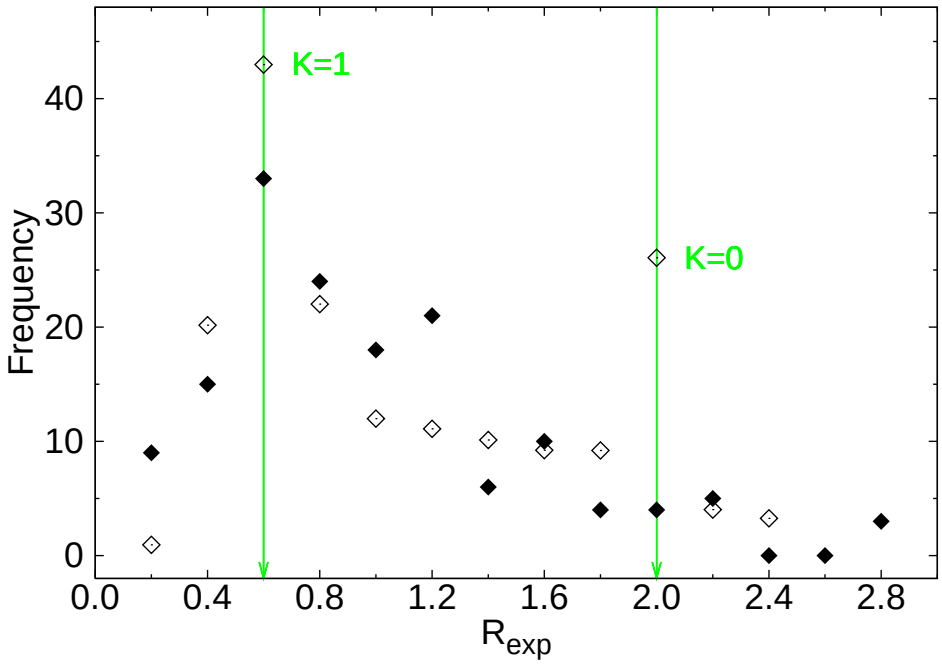

Figure 7.8: The frequency distribution of R_{exp} values for rare-earth nuclei (◊) from Ref. [94] and for actinide nuclei (◆) from the present work and Refs. [14, 37, 54, 78].

increase in regions of high level density [95]. This is the first compilation of R_{exp} values for the actinide nuclei.

7.5.2 Spreading Widths

The width of an isobaric analog state (IAS), also called the spreading width $\Gamma\uparrow$, is proportional to the matrix element that couples the IAS to lower-spin states. The spreading widths for many nuclei were extracted experimentally from the strength function. It was observed that although the distance between levels changes drastically between nuclei, the spreading width hardly varies [96]. The spreading width, $\Gamma\uparrow$ is defined as

$$\Gamma\uparrow = \frac{2\pi\bar{H}_C^2}{D} \quad , \tag{7.6}$$

where D is the mean level spacing and $\bar{H}_C$ is the mixing matrix element such that,

$$< H_C >= |E_{oct} - E_{GDR}| \cdot \sqrt{\frac{B(E1)}{B(E1, GDR)}} \quad , \tag{7.7}$$

where E_{oct} (E_{GDR}) is the excitation energy of the low-lying octupole states (GDR) and $B(E1)$ ($B(E1, GDR)$) is the strength from $E1$ ground-state transitions (from the GDR). Zilges *et al.* [97] calculated the spreading widths from averaged mixing matrix elements for rare-earth and actinide nuclei, comparing the widths with those extracted from isobaric analog resonances [96] (see Fig. 7.9). In Ref. [97], the spreading width for ^{238}U, ~8 keV, grossly underestimates the one obtained from the isobaric analog state, 142(37) keV. However, substituting for the present work's $E1$ strength, the spreading width increases to

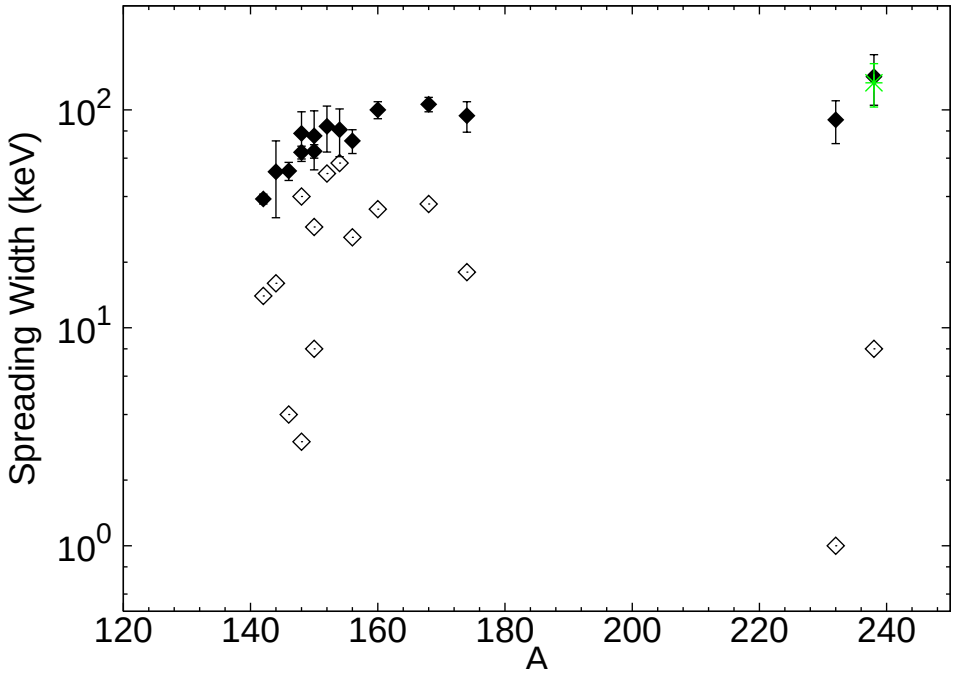

Figure 7.9: The spreading widths for select nuclei with $140 < A < 180$. The spreading width calculations of Ref. [97] are in (◇) while the experimental data complied by Ref. [96] are in (◆). The present experimental value for the spreading width is shown as (∗).

133(30) keV, which is in very good agreement with the value from Ref. [96].

7.5.3 Comparison of Experimental Transition Strengths from $140 < A < 180$ Nuclei

Many nuclei with $140 < A < 180$ have deformations and neutron excesses which could provide a comparison with the structure of the heavier nuclei in the actinide region with similar deformations. Two deformed nuclei of ^{154}Sm ($\delta = 0.273$) and ^{178}Hf ($\delta = 0.230$) were subjects of many experiments and theoretical calculations [31, 59]. If the deformation of a nucleus is the primary generator of $M1$ strength then it is plausible that similarly deformed nuclei should contain a similar amount of $M1$ strength. A comparison of the observed $M1$ strength within the same energy range shows that the strength observed in those

two nuclei is only 75% of the ^{238}U ($\delta = 0.234$) strength measured in Ref. [1] and only 33% of the strength found in the current experiment. However, the $M1$ strength measured in ^{232}Th ($\delta = 0.216$) [14] is of a similar magnitude. QRPA calculations of Ref. [31] of the $M1$ strength detail that a similar strength should be found with similarly deformed nuclei in both the rare-earth and actinide nuclei. However, these calculations are only approximations and do not describe each particular nuclei as an exact solution. This inconsistency between comparisons indicates that deformation is not the primary generator of the $M1$ strength and that other physical processes need to be taken into account.

Within the $E1$ transition strengths, the deviations between the $140 < A < 180$ nuclei and the actinides are more significant. The theoretical calculations of Ref. [31] predict for the $140 < A < 180$ nuclei only about 70-80% of the strength predicted for the actinides. With limited experimental values of $E1$ strength for the $140 < A < 180$ nuclei available, it is hard to say whether this is a good indication of a disagreement between the two mass regions.

Therefore, these $140 < A < 180$ nuclei provide some insight into the $M1$ and $E1$ strengths in actinide nuclei. The experimental transition strengths are not the same as the calculations which could suggest that some other physical processes remain unaccounted within the calculations. In general, the actinides have a larger strength present than the $140 < A < 180$ nuclei, which could possibly be due to the larger neutron excess present. More experimental data are needed on both dipole strengths for the $140 < A < 180$ and actinide nuclei in order to make a fair assessment of their compatibilities. With more experimental data, better theoretical calculations could be developed to assess the similarities

between similarly deformed nuclei.

7.6 Comparison to Theoretical Calculations

The strengths of the dipole states observed in the present measurement are similar in magnitude to the strength predicted by QRPA calculations of Kuliev *et al.* [30] described in Section 3.2. Comparisons of experimentally summed strengths to the calculated values are given in Tables 7.2 and 7.3 for ^{154}Sm, ^{160}Gd, ^{232}Th, and ^{238}U from Refs. [14, 53, 57]. The calculations of the $M1$ strength in ^{154}Sm and of the $E1$ strength in ^{160}Gd show that the QRPA calculations reproduce dipole strength distribution and intensity fairly well for the rare-earth nuclei. Well-studied rare-earth nuclei can be used to test the robustness and the ability of the calculation to reproduce measurements. The experimental $M1$ strengths from ^{232}Th [14] and ^{238}U are similar to those from the calculations [30, 31]. However, the $E1$ strengths from the present work and from the QRPA calculations of Kuliev *et al.* [30] have a different conclusion. The calculation for $E1$ strength in ^{232}Th is about ten times larger than what was experimentally observed [14]. For ^{238}U, the reverse is true and the calculation underproduces the observed $E1$ strength in the same energy range from the present experiment by a factor of two. The possible differences between the two calculations could be due to the different type of ground states used in each (see Chapter 3 for more details).

The results of the QRPA calculation by Kuliev *et al.* [30, 55] reproduce the gross structure of the current experimental summed $M1$ and $E1$ strengths in this energy region fairly well. In Fig. 7.10, the calculations of Ref. [30] and the present measurement are compared using a 0.2 MeV bin size. The present measurement of the $M1$ and $E1$ strength is shown

Table 7.2: $M1$ strength of the present work compared with other experiments [14, 54, 57] and theoretical calculations [30, 31] for actinide nuclei. Energy range for comparison was chosen based on predicted location of the scissors mode.

	Experiment		
	^{154}Sm [57]	^{232}Th [14]	^{238}U
ω (MeV)	3.26(9)	2.5	2.4(4)
$\sum B$ ($\mu_N{}^2$)	2.4(4)	4.3(6)	6.1(9)
$\sum B/\Delta E$ ($\mu_N{}^2$/MeV)	1.6	2.2	6.2
Range (MeV)	2.5-4	2-4	2-3

	Theory			
	^{154}Sm [31]	^{232}Th [30]	^{238}U [30]	^{238}U [31]
ω (MeV)	–	2.6	2.4	–
$\sum B$ ($\mu_N{}^2$)	3.3	5.0	4.6	3.7
$\sum B/\Delta E$ ($\mu_N{}^2$/MeV)	1.7	2.5	4.6	2.5
Range (MeV)	2-4	2-4	2-3	1.5-3

in two ways on Fig. 7.10: as strength originating from the discrete states and as strength extrapolated from the continuum of states using the method described in Section 7.3. Both methods compare well with the QRPA calculation. The extrapolated strength from the continuum is slightly lower than that from the discrete states because the extrapolated strength uses an average R_{exp} since it is taken from a 50-keV window while the strength derived from the discrete states uses real R_{exp} values measured in this experiment.

Over half of the predicted $M1$ strength is present within 2.0-2.6 MeV and are assumed to be part of the scissors mode. Away from this narrow energy region, the predicted $M1$ strength decreases. Both of those features are observed in the present experiment. However, $M1$ strength above 3.5 MeV is predicted with a similar amplitude as the transitions at lower energies. This feature is not observed in the present experiment within the detection limit. Calculations of the $M1$ strength for the actinides by the authors of Ref. [30] yield a result of $\sim 6\ \mu_N{}^2$ which underestimates the measured strength of the present experiment by 25%.

Table 7.3: $E1$ strength of the present work compared with experiments [14, 53] and theoretical predictions [30, 31, 59] for actinide nuclei.

	Experiment		
	^{160}Gd [53]	^{232}Th [14]	^{238}U
ω (MeV)	2.9(1)	3.7(4)	3.3(8)
$\sum B$ ($\times 10^{-3} e^2\text{fm}^2$)	16(2)	3.3(7)	110(30)
$\sum B/\Delta E$ ($\times 10^{-3}$ $e^2\text{fm}^2$/MeV)	8	2	48
Range (MeV)	2-4	2-4	2-4.3

	Theory			
	^{160}Gd [59]	^{232}Th [30]	^{238}U [30]	^{238}U [31]
ω (MeV)	–	2.7	3.6	–
$\sum B$ ($\times 10^{-3} e^2\text{fm}^2$)	21	35	50	~40
$\sum B/\Delta E$ ($\times 10^{-3}$ $e^2\text{fm}^2$/MeV)	11	18	22	24
Range (MeV)	2-4	2-4	2-4.3	2.6-4.3

In the present work, eight $E1$ transitions are observed below 2.5 MeV of a summed strength equal to 20(4) $\mu_N{}^2$, which is much larger than predicted. The $E1$ strength calculations do not predict the summed $E1$ strength well since there is a significant amount of the summed strength due to discrete transitions above 4.3 MeV, which are not resolved in the experiment. Over 70% of the $E1$ strength predicted is located in the range between 4.3 and 5.6 MeV, and not at the lower energies, as observed in the experiment. Furthermore, there is a significant amount of observed strength around 3.5 MeV that the calculation misses entirely. Again, the example of ^{160}Gd from the rare-earth nuclei provides verifiability of the choices for models and parameters used within these calculations [59]. However, this same calculation does not seem to predict the fragmentation of the strength very well for heavier nuclei. It is possible that more higher-order quasiparticle states are needed to describe the collective excitations in the actinides or that the effective charge used to model the nuclear charge quenches too much of the predicted strength.

The calculations by Soloviev *et al.* [31] predict two concentrations of transitions in the area of interest. One concentration of $M1$ strength is predicted between 2.6-3.0 MeV, and the second concentration of $E1$ strength is predicted between 3.4-4.0 MeV. In the present experiment, four concentrations are observed: one for $M1$ states around 2.5 MeV and three for $E1$ states around 3.1, 3.5, and 4.0 MeV. The authors of Ref. [31] also predicted that within the energy range of 3-11 MeV, 28% of the total $M1$ strength would be from the scissors mode and 107% would be from the spin-flip mode. A value over 100% indicates some interference between the orbital and spin components of the $M1$ matrix element. The $M1$ strength predicted by Ref. [31] is similar in magnitude to the prediction by Ref. [30]. It is found in Ref. [31] that the total $E1$ strength is about 3-4 times larger than the total $M1$ strength. Also the calculated $E1$ strength for ^{238}U is about three times larger than the experimental value.

Comparing the calculation by Soleviev *et al.* [31] for ^{154}Sm and ^{178}Hf between the energies of 3.6-7.6 MeV, the $B(M1)$ values were predicted to be 5.7 and 7.1 $\mu_N{}^2$, respectively, and the $B(E1)$ values were 217 and 271 $\times 10^{-3} e^2 \mathrm{fm}^2$, respectively. These $B(M1)$ values are about twice as large as the experimental ones while the $B(E1)$ values are about two orders of magnitude too large from their associated experimental values (see Section 4.1 for details). Also these $B(E1)$ predictions are twice as large as the experimental $E1$ strength for ^{238}U. Since the energy ranges for the experiment and the calculation are different, a comparison of $\sum B/\Delta E$ may prove to be a better testament of the calculation's abilities of predicting strength. For $\sum B(M1)/\Delta E$, the measured and calculated values are similar but for $\sum B(E1)/\Delta E$, these values are quite different (see Table 4.1 for values).

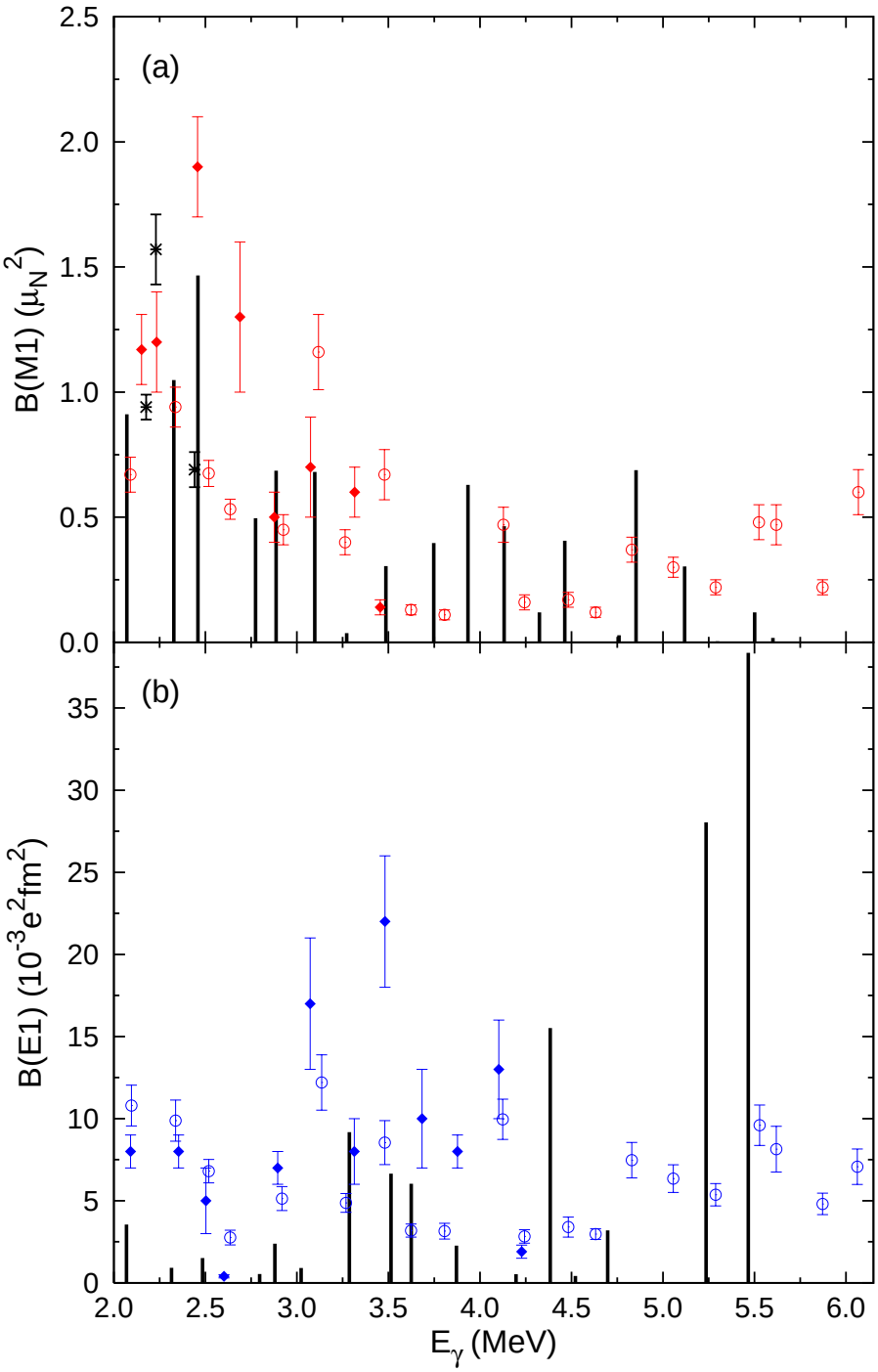

Figure 7.10: Experimental (a) $M1$ and (b) $E1$ strengths such that (◆) are from this work and (∗) are from Ref. [1]. The data points shown as (○) are extrapolated from the total cross section data. These data are compared with a QRPA calculation (|) from Ref. [30] with a 0.2 MeV bin size. Experimental strength values are shown with statistical error bars.

In summary, the present experimental data on dipole transitions in ^{238}U were compared with previous data as well as data on $140 < A < 180$ nuclei. The experimental transition strengths were in good agreement with the theoretical calculations of Ref. [30].

Chapter 8

Conclusions

In the course of this work, NRF measurements were performed on ^{238}U at the HIγS facility using 100% linearly-polarized, quasi-monoenergetic beams with energies between 2.0 and 6.2 MeV. Over 200 hours of beam time was used to observe one-hundred thirteen new discrete deexcitations to the ground state at energies between 2.0 and 4.2 MeV. Their spin and parity were determined using the unique polarimetry setup of the detector array. Thirty percent of the observed states were $M1$ transitions and the rest were $E1$ transitions. Strengths, R_{exp} values, as well as other spectroscopic data were measured for these states and were compared to data from previous experimental sets on $140 < A < 180$ nuclei as well as other actinide nuclei. The first R_{exp} compilation for the actinide nuclei was made, which provided the observation that a significant amount of K-mixing is present in the actinides.

Above 4.2 MeV, only the asymmetry of the continuum of states could be investigated due to the detection limit of the experiment and the increasing level density. The average total γ-ray interaction cross section were determined from 2.0 to 6.2 MeV in order to deduce the origins of the low-lying strength. Comparison of the low-lying $E1$ strength to the

MLO and SLO fits to the low-energy tail of the GDR as well as statistical model calculations provided evidence that the observed strength is not from a pygmy resonance. This is the first analysis on any actinide nuclei which investigates the existence or nonexistence of a PDR.

Discrete states were compared with QRPA calculations and "sum rule" predictions. These calculations and predictions describe the overall structure of the observed states but do not describe its finer details well. In particular, the calculations seem to represent the observed fragmentation of the $M1$ strength fairly well but this is not the case for the $E1$ strength where it is largely concentrated towards higher energies. More comparisons between experiments and theoretical calculations are needed for other $140 < A < 180$ and actinide nuclei in order to provide a better understanding of the low-energy structure of nuclei with large deformations and large neutron excess.

The present work on ^{238}U was a part of a larger effort to extensively study the low-energy nuclear structure of the actinide nuclei in which ^{232}Th [14] and ^{235}U [78] were also studied. Algorithms for data acquisition for NRF experiments were established and tested through experiments on ^{11}B [48], on ^{138}Ba [45], on ^{142,150}Nd [98], on ^{232}Th [14], on ^{235}U [78], as well as on many others. These methods provide robust systems that are much improved from their initial deployment. Future efforts may include NRF experiments on other actinides such as ^{234,236}U as well as ^{239,240}Pu. It may also involve other deformed nuclei between $140 < A < 180$ for more thorough comparisons with actinide nuclei.

National security efforts funded the present experiments since safeguarding national borders from terrorist threats are an important undertaking and the NRF process provides

a well-understood and efficient way to procure information from hidden SNM. In the future, the NRF technique will most likely be used in monitoring nuclear waste assays or exploring the concentrations of reprocessed nuclear fuel rods. With the miniaturization of high-intensity γ-ray beams from large facilities [71] to table-top optical systems [99, 100], the feasibility of scanning many nuclear assays across the nation seems much more attainable with the development of new technologies.

Finally, as more NRF measurements are produced, a database for isotope-specific identification will need to be developed in order to organize and compare experimental data with ease. This library of results would be resourced by those trying to identify unknown materials inside sealed containers. The present work made a substantial contribution towards establishing such a database.

This work was supported in part by the United States Department of Homeland Security through the Academic Research Initiative with grants 2008-DN-077-ARI014 and 2008-DN-077-ARI010 and by the United States Department of Energy with grant DE-FG02-97ER41041.

The results of this work have been submitted for publication under the same title in a peer-reviewed journal, the Physical Review C.

Appendix A

Self Absorption

Relative self absorption, S_a, is a correction to I_s, which depends on the Z of the target material, the photon energy, and the Doppler-broadened width of the transition. As photon energy increases, self absorption decreases. It is defined as [18]

$$S_a(d) = \frac{R(0) - R(d)}{R(0)} \ , \tag{A.1}$$

where $R(x)$ is the count rate with ($x = d$) and without ($x = 0$) the absorbing material.

$$S_a(d) = \frac{\int N(E) e^{-n_{tot}\sigma_e} \left(1 - e^{-n_t \sigma_{\gamma\gamma}(E) - n_{tot}\sigma_e}\right)(1 - e^{-n_t \sigma_D})\ \mathrm{d}E}{\int N(E) e^{-n_{tot}\sigma_e} \left(1 - e^{-n_t \sigma_{\gamma\gamma}(E) - n_{tot}\sigma_e}\right)\ \mathrm{d}E} \ , \tag{A.2}$$

where N(E) is the number of incident γ rays, σ_e is the total effective electronic absorption cross section, n_{tot} is the total number of nuclei per area, n_t is the number of resonant target nuclei per area, $\sigma_{\gamma\gamma}(E)$ is the elastic scattering Doppler broadened cross section, and $\sigma_D(E)$ is the Doppler broadened absorption cross section.

$$\sigma_e = \sigma_{ph} + \sigma_c + \sigma_{pp} \ , \tag{A.3}$$

where subscripts ph, c, and pp stand for photoelectric effect, incoherent (Compton) scattering, and pair production, respectively. Each electronic cross section takes on the following

form:

$$\sigma_x = \frac{M_n}{N_A}\mu_x \ , \tag{A.4}$$

where M_n is the nuclear mass, N_A is Avogadro's number, and μ_x is the corresponding electronic process's mass attenuation coefficient in cm^2/g. Mass attenuation coefficients for the three processes are found in NIST's XCOM database [85]. As seen in Fig.A.1, σ_e is approximately constant over the selected energy region. Assuming slow-energy variation of σ_e means that it is independent of E and can be pulled out from the integral.

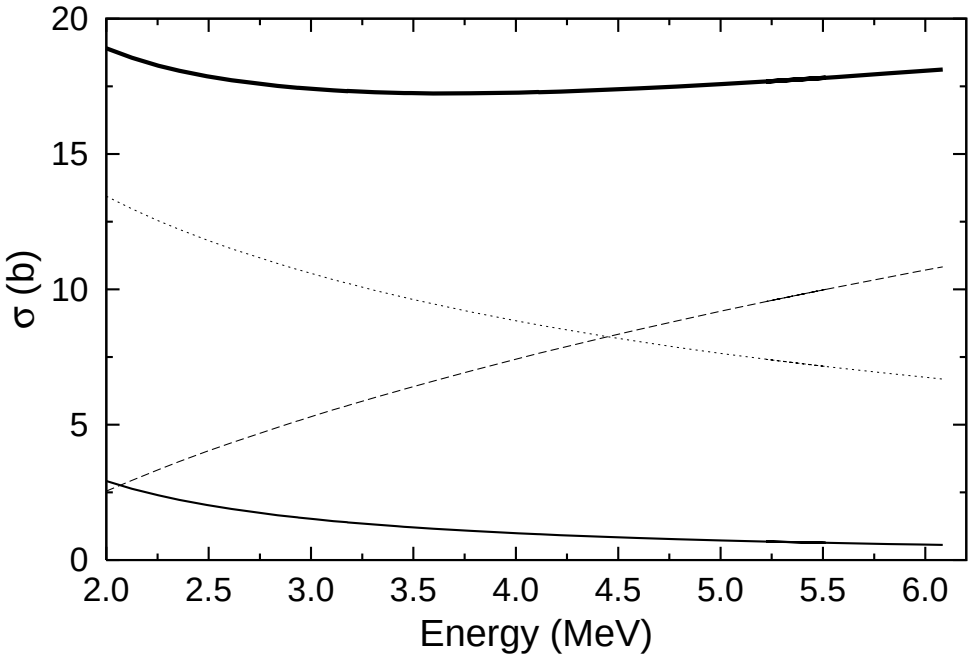

Figure A.1: Total electronic cross section between 2.0 and 6.2 MeV (thick,solid curve). The cross sections of photoelectric (thin,solid curve), Compton (dotted curve), and pair production (dashed curve) are shown as well.

Also, if we assume that $N(E)$ is either slow-varying or linear in E then this term can also be pulled from the integral and subsequently cancels out of S_a. This is a valid assumption since $N(E)$ is nearly constant over the width of the transitions described in this dissertation which are on the order of $10^{-3}\ eV$ while the width of the beam is on the order of $10^2\ keV$.

The exponentials in Eq. (A.2) can be written in an series form,

$$e^{-x} = \sum_{n=0}^{\infty} \frac{x^n (-1)^n}{n!} \tag{A.5}$$

and

$$e^{x} = \sum_{n=0}^{\infty} \frac{x^n}{n!} \ . \tag{A.6}$$

Assuming a first order approximation of the exponential terms including $\sigma_{\gamma\gamma}(E)$ and $\sigma_D(E)$ we can rewrite e^{-x} as $(1 - x)$:

$$S_a(d) = \frac{\int \left(1 - \left(1 - n_t \sigma_{\gamma\gamma}(E)\right) e^{-n_{tot}\sigma_e}\right) (1 - (1 - n_t \sigma_D(E)))\ \mathrm{d}E}{\int \left(1 - \left(1 - n_t \sigma_{\gamma\gamma}(E)\right) e^{-n_{tot}\sigma_e}\right) \mathrm{d}E} \ . \tag{A.7}$$

Rearranging the terms,

$$S_a(d) = \frac{n_t \left(e^{n_{tot}\sigma_e} - 1\right) \int \sigma_D(E)\mathrm{d}E + n_t^2 \int \sigma_{\gamma\gamma}(E)\sigma_D(E)\mathrm{d}E}{\left(e^{n_{tot}\sigma_e} - 1\right) \int \mathrm{d}E + n_t \int \sigma_{\gamma\gamma}(E)\mathrm{d}E} \ , \tag{A.8}$$

but

$$\int \mathrm{d}E = \int_{E-\Gamma_0/2}^{E+\Gamma_0/2} \mathrm{d}E' = \Gamma_0 \ , \tag{A.9}$$

which is the width of the ground state resonance. If we again take a first order approximation of the term $e^{n_{tot}\sigma_e}$ where $e^x \approx (1 + x)$, we have

$$S_a(d) = \frac{(n_{tot}\sigma_e) \int \sigma_D(E)\mathrm{d}E + n_t \int \sigma_{\gamma\gamma}(E)\sigma_D(E)\mathrm{d}E}{\frac{n_{tot}}{n_t}\sigma_e\Gamma_0 + \int \sigma_{\gamma\gamma}(E)\mathrm{d}E} \ . \tag{A.10}$$

From the discussion of the photon scattering cross section in Chapter 2, we have the defi-

nitions for two of these integrals, Eq. (2.20) and Eq. (2.22), such that,

$$\int \sigma_{\gamma\gamma}(E)\sigma_D(E)\mathrm{d}E = \pi^3 \lambda\!\!\!^{-4} g^2 \frac{\Gamma_0^3}{\Gamma} \int \frac{1}{\Delta^2} e^{-2\left(\frac{E-E_r}{\Delta}\right)^2} \mathrm{d}E \ . \tag{A.11}$$

Recall that $\Delta = aE$ and change the integration variable to z where $z = E_r/E$

$$\int \sigma_{\gamma\gamma}(E)\sigma_D(E)\mathrm{d}E = \frac{\pi^3 \lambda\!\!\!^{-4} g^2}{a^2 E_r} \frac{\Gamma_0^3}{\Gamma} \int_{-\infty}^{\infty} e^{-\frac{2}{a^2}(1-z)^2} \mathrm{d}z \ , \tag{A.12}$$

where

$$\int_{-\infty}^{\infty} e^{-\frac{2(1-z)^2}{a^2}} \mathrm{d}z = a\sqrt{\frac{\pi}{2}} \ , \tag{A.13}$$

and

$$\int \sigma_{\gamma\gamma}(E)\sigma_D(E)\mathrm{d}E = \frac{\pi^{7/2} \lambda\!\!\!^{-4} g^2}{aE_r\sqrt{2}} \frac{\Gamma_0^3}{\Gamma} \ . \tag{A.14}$$

Therefore, the self absorption is defined as,

$$S_a(d) = \frac{(n_{tot}\sigma_e)\,\pi^2 \lambda\!\!\!^{-2} g \Gamma_0 + n_t \dfrac{\pi^{7/2} \lambda\!\!\!^{-4} g^2 \left(\Gamma_0^3/\Gamma\right)}{aE_r\sqrt{2}}}{\dfrac{n_{tot}}{n_t}\sigma_e\Gamma_0 + \pi^2 \lambda\!\!\!^{-2} g \left(\Gamma_0^2/\Gamma\right)} \ , \tag{A.15}$$

or in terms of experimental parameters,

$$S_a(d) = \frac{(n_{tot}\sigma_e) + \dfrac{n_t I_s}{aE_r\sqrt{2\pi}}}{\dfrac{n_{tot}}{n_t}\dfrac{\sigma_e}{\pi^2 \lambda\!\!\!^{-2} g} + b} \ , \tag{A.16}$$

where $n_t = \dfrac{\chi_i}{100} n_{tot}$ (i indicates the resonant isotope), I_s is the integrated elastic photon scattering cross section, and b is the branching ratio Γ_0/Γ. $S_a(d)$ will have values between

0 and 1 where values closer to 0 indicate low self-absorption within the target material and values closer to 1 indicate high self-absorption. The integrated cross section I_s has to be corrected for $S_a(d)$ in any target with a finite thickness d. For a thin target (negligible thickness), the terms with σ_e would be eliminated from Eq. (A.15) making for a much smaller correction:

$$S_a = \sqrt{\frac{\pi^3}{2}} \lambda\!\!\!^{-2} g n_t \frac{\Gamma_0}{\Delta} \ , \tag{A.17}$$

where $E = E_r$ in the definitions of $\lambda\!\!\!^{-}$ and Δ.

Appendix B

Sample MCNPX Input Files

B.1 Summed 60% Detectors Efficiency Calculation

```
The 60% Ge-detector; original by A. Tonchev & A. Chyzh;
                                    (modified by S. L. Hammond)
c --------------------------CELLS-------------------------------------
c *
11     1  -2.6989     -11  21            u=1      $ Al End Cap
12     1  -2.6989     -12  31 23         u=1      $ Al Foild
21     0              -21  12 22         u=1      $ Inner Vacuum
23     0              -23  22            u=1      $ Top Vacuum
24     1  -2.6989     -24  12 22         u=1      $ Al mount cup base
31     3  -5.323      -31  22            u=1      $ Ge Crystal
c 34     3  -5.323      -34  12          u=1      $ Dead Zone
22     5  -8.96       -22               u=1      $ Hole
62     5 -8.96     -62 63 11            u=1      $ Cu attenuator
63     6 -11.35     -63 62 11           u=1      $ Pb attenuator
13     0                11 62 63        u=1      $void
2      0              -11       u=2  fill=1      $detector object
25     0              -62       u=2  fill=1
26     0              -63       u=2 fill=1
20     0               11 62 63         u=2      $ void
3 like 2 but *trcl=(0 0 6.20 0 -90 -90 90 -90 -180 -90 0 90 -1) u=3
32 like 25 but *trcl=(0 0 6.20 0 -90 -90 90 -90 -180 -90 0 90 -1) u=3
33 like 26 but *trcl=(0 0 6.20 0 -90 -90 90 -90 -180 -90 0 90 -1) u=3
4 like 2 but *trcl=(0 0 6.20 0 -90 90 -90 90 0 90 180 90 -1) u=3
42 like 25 but *trcl=(0 0 6.20 0 -90 90 -90 90 0 90 180 90 -1) u=3
43 like 26 but *trcl=(0 0 6.20 0 -90 90 -90 90 0 90 180 90 -1) u=3
74     4  -0.00129   #3 #32 #33 #4 #42 #43   u=3  $ Air Environment
52     0             -52              fill=3      $ empty cell filled
10     0              52                          $ Void
c *
c ------------------------------------------------------------------------
c *
c -------------------------SURFACES-------------------------------------
c *
11   rcc 0.0 0.0  16.2    0.0 0.0  11.576   3.806   $ Al End Cap
12   rcc 0.0 0.0  16.7    0.0 0.0  10.576   3.306   $ Al Foil Cup
21   rcc 0.0 0.0  16.3    0.0 0.0  11.376   3.706   $ Inner Vacuum
22   rcc 0.0 0.0  17.596  0.0 0.0  7.27     0.56    $ Hole
23   rcc 0.0 0.0  24.866  0.0 0.0  2.09     3.23    $ Top Vacuum
24   rcc 0.0 0.0  26.956 0.0 0.0  0.244    3.23     $ Al mount cup base
31   rcc 0.0 0.0  16.776  0.0 0.0  8.09     3.23    $ Ge Crystal
c 34   rcc 0.0 0.0  19.11  0.0 0.0  0.1      3.23   $ Dead Zone
```

```
62   rcc 0.0 0.0  15.677  0.0 0.0 0.4    3.806      $ Cu attenuator
63   rcc 0.0 0.0  15.147  0.0 0.0 0.53    3.806     $ Pb attenuator
52   rcc 0.0 0.0 -50.0    0.0 0.0 100.0    100.0    $ Air Environment
c *
c ---------------------------------------------------------------------
c *
c -------------------------MATERIALS-----------------------------------
c *
c #1 (Aluminum)
M1     13000.02p   1.0
c #3 (Germanium)
M3     32000.02p   1.0
c #4 (Air)
M4      8016.02p   0.23555
        7014.02p   0.75086
       18000.02p   0.01281
        1001.02p   0.00064
        6012.02p   0.00014
c #5 (Copper)
M5     29000.02p  1.0
c #6 (Lead)
 M6     82000.02p  1.0
c #7 (238U target)
c M7  92238.02p   0.9927
c     92235.02p   0.0072
c     92234.02p   0.0001
c
c -------------------------SOURCE--------------------------------------
c (5 mm diameter source)
SDEF POS= 0.0 0.0 0.0 RAD=D2 PAR=P ERG=5.5
c
SI2   0.25
c ---------------------------------------------------------------------
c *
c -------------------------TALLIES-------------------------------------
FC18 *Pulse Height Ge-Detector at cell 31 Ge-crystal*
F18:P 31
E18 0.0 1E-5 1000i 6.5
c -----------------------------------------------
c *
c -------------------------Physics-------------------------------------
IMP:P,E 1 1 1 1 1 1 1 1 0 1 1 1 1 1 1 1 1 1 1 0
MODE P E
CUT:P,E j 0.1
NPS 1e6
```

B.2 Clover Detector Efficiency Calculation

```
c  Tony Hutcheson  (modified by S.L.Hammond)
c ----------------------------- Cell Definitions ------------------------------
1   2   -2.6989   (-1 5 3 4):(-2 6 4):(-7 3 4)         TRCL=1   $ Al Walls
2   4   -7.13     (-10:-11) 8 9                        TRCL=1   $ BGO
```

```
3   1   -0.00129  (-5 10 11):(-6 11):(-8 7):(-9 7)     TRCL=1   $ Inner Space
4   3   -5.323     -21 -25 31                          TRCL=1   $ Ge 2Q1
5   3   -5.323     -22 -26 32                          TRCL=1   $ Ge 2Q2
6   3   -5.323     -23 -27 33                          TRCL=1   $ Ge 2Q3
7   3   -5.323     -24 -28 34                          TRCL=1   $ Ge 2Q4
8   2   -2.6989    -30 29                              TRCL=1   $ Al Cap
9   2   -2.6989   (-31 35):(-32 36):(-33 37):(-34 38)  TRCL=1   $ Al Inner
10  0   (-25 21):(-26 22):(-27 23):(-28 24):(-29 25 26 27 28):-35:-36:-37:-38 &
                                                       TRCL=1
11  LIKE 1 BUT                                         TRCL=2
12  LIKE 2 BUT                                         TRCL=2
13  LIKE 3 BUT                                         TRCL=2
14  LIKE 4 BUT                                         TRCL=2
15  LIKE 5 BUT                                         TRCL=2
16  LIKE 6 BUT                                         TRCL=2
17  LIKE 7 BUT                                         TRCL=2
18  LIKE 8 BUT                                         TRCL=2
19  LIKE 9 BUT                                         TRCL=2
20  LIKE 10 BUT                                        TRCL=2
90  0               90                                        $ Void
99  1   -0.00129    #1  #2  #3  #4  #5  #6  #7  #8  #9  #10              &
                    #11 #12 #13 #14 #15 #16 #17 #18 #19 #20              &
                    #90                                       $ Air
c --------------------------- Surface Definitions -----------------------------
1    arb   5.950  5.950 0.000   5.950 -5.950 0.000   -5.950 -5.950 0.000 &
          -5.950  5.950 0.000   10.60  10.60 12.77    10.60 -10.60 12.77 &
          -10.60 -10.60 12.77  -10.60  10.60 12.77                       &
           1234 5678 1265 4378 1584 2673                      $ Al Walls #1
2    box   10.60  10.60 12.77  -21.20  0.000 0.000    0.000 -21.20 0.000 &
           0.000  0.000 12.93                                 $ Al Walls #2
3    box   4.25 4.25 0.00   -8.50 0 0   0 -8.50 0   0 0 1.00  $ Inner Hollow #1
4    box   5.10 5.10 1.00   -10.2 0 0   0 -10.2 0   0 0 24.7  $ Inner Hollow #2
5    arb   6.045  6.045 0.700   6.045 -6.045 0.700   -6.045 -6.045 0.700 &
          -6.045  6.045 0.700   10.45  10.45 12.77    10.45 -10.45 12.77 &
          -10.45 -10.45 12.77  -10.45  10.45 12.77                       &
           1234 5678 1265 4378 1584 2673                      $ Inner Wall #1
6    box   10.45 10.45 12.77   -20.9 0 0   0 -20.9 0   0 0 12.85         &
                                                           $ Inner Wall #2
7    box   5.18  5.18 0.700  -10.36 0 0   0 -10.36 0   0 0 24.92         &
                                                           $ Inner Wall #3
8    arb   5.18  5.18 0.700   5.18 -5.18 0.70  -5.18 -5.18 0.70          &
          -5.18  5.18 0.700   5.25 5.25 2.173   5.25 -5.25 2.173         &
          -5.25 -5.25 2.173  -5.25 5.25 2.173   1234 5678 1265 4378 1584 2673
                                                           $ Inner BGO #1
9    arb   5.25  5.25 2.173   5.25 -5.25 2.173 -5.25 -5.25 2.173         &
          -5.25  5.25 2.173   7.14  7.14 25.62  7.14 -7.14 25.62         &
          -7.14 -7.14 25.62  -7.14  7.14 25.62  1234 5678 1265 4378 1584 2673 &
                                                           $ Inner BGO #2
10   arb   5.975  5.975 0.70    5.975 -5.975 0.70   -5.975 -5.975 0.70   &
          -5.975  5.975 0.70    7.450  7.450 4.76    7.450 -7.450 4.76   &
          -7.450 -7.450 4.76   -7.450  7.450 4.76                       &
           1234 5678 1265 4378 1584 2673                      $ Outer BGO #1
11   arb   7.450  7.450 4.76    7.450 -7.450 4.76   -7.450 -7.450 4.76   &
          -7.450  7.450 4.76    9.128  9.128 25.62   9.128 -9.128 25.62  &
          -9.128 -9.128 25.62  -9.128  9.128 25.62                       &
           1234 5678 1265 4378 1584 2673                      $ Outer BGO #2
21   rcc   2.26  2.26 4.40   0.00 0.00 8.00   2.5             $ Ge Q1
22   rcc  -2.26  2.26 4.40   0.00 0.00 8.00   2.5             $ Ge Q2
23   rcc  -2.26 -2.26 4.40   0.00 0.00 8.00   2.5             $ Ge Q3
```

```
24   rcc   2.26 -2.26 4.40   0.00 0.00 8.00   2.5             $ Ge Q4
25   box   0.03  0.03 4.40   4.50 0.00 0.00   0.0   4.5 0.0   0.0 0.0 8.0
26   box  -0.03  0.03 4.40  -4.50 0.00 0.00   0.0   4.5 0.0   0.0 0.0 8.0
27   box  -0.03 -0.03 4.40  -4.50 0.00 0.00   0.0  -4.5 0.0   0.0 0.0 8.0
28   box   0.03 -0.03 4.40   4.50 0.00 0.00   0.0  -4.5 0.0   0.0 0.0 8.0
29   box  -4.90 -4.90 3.75   9.80 0.00 0.00   0.0   9.8 0.0   0.0 0.0 8.65
30   box  -5.05 -5.05 3.60   10.1 0.00 0.00   0.0   10.1 0.0   0.0 0.0 8.95
31   rcc   2.26  2.26 5.90   0.00 0.00 6.50   0.5             $Au Outer Surface
32   rcc  -2.26  2.26 5.90   0.00 0.00 6.50   0.5             $Au Outer Surface
33   rcc  -2.26 -2.26 5.90   0.00 0.00 6.50   0.5             $Au Outer Surface
34   rcc   2.26 -2.26 5.90   0.00 0.00 6.50   0.5             $Au Outer Surface
35   rcc   2.26  2.26 5.95   0.00 0.00 6.45   0.45            $Au Inner Surface
36   rcc  -2.26  2.26 5.95   0.00 0.00 6.45   0.45            $Au Inner Surface
37   rcc  -2.26 -2.26 5.95   0.00 0.00 6.45   0.45            $Au Inner Surface
38   rcc   2.26 -2.26 5.95   0.00 0.00 6.45   0.45            $Au Inner Surface
90   so    50
c ------------------------------ Material List --------------------------------
c   Material #1 (Air)
M1    7000.04p    0.75527   GAS=1   &
      8000.04p    0.23178   GAS=1   &
     18000.04p    0.01283   GAS=1   &
      6000.04p    0.00012   GAS=1
c   Material #2 (Aluminum)
M2   13000.04p    1.0
c   Material #3 (Germanium)
M3   32000.04p   1.0
c   Material #4 (BGO)
M4    8000.04p    0.63158           &
     32000.04p    0.15789           &
     83000.04p    0.21053
c
*TR1  0 10  0   0 90 90   90 -90 -180   90  0 -90
*TR2  0  0 10   0 90 90   90   0   90   90 90   0
c
imp:p,e 1 1 1 1 1 1 1 1 1 1 1 1 1 1 1 1 1 1 0 1
mode p e
c
c --------------------------------- Source Definition ------------------------
c (5mm diameter source)
SDEF POS=0.0 -0.3175 0.0 RAD=D2 PAR=P ERG=0.625
c
SI2    0.25
c
F8:P  4
E8  0.0 1E-5 2000I 6.0
F18:P 5
E18 0.0 1E-5 2000I 6.0
F28:P 6
E28 0.0 1E-5 2000I 6.0
F38:P 7
E38 0.0 1E-5 2000I 6.0
F48:P 14
E48 0.0 1E-5 2000I 6.0
F58:P 15
E58 0.0 1E-5 2000I 6.0
F68:P 16
E68 0.0 1E-5 2000I 6.0
F78:P 17
E78 0.0 1E-5 2000I 6.0
```

```
c
NPS 1e6
```

B.3 Flux Monitor Efficiency Calculation

```
The 123% Ge-detector; original by A. Tonchev & A. Chyzh;
                                        (modified by S. L. Hammond)
c *
c ---------------------------CELLS-----------------------------------
c *
11     1  -2.6989     -11  21        u=1
                                 $ Al End Cap at 158.7cm from Cu-target
12     1  -2.6989     -12  31  23    u=1     $ Al Foild
21     0              -21  12  62    u=1     $ Inner Vacuum
23     0              -23  62        u=1     $ Top Vacuum
31     3  -5.323      -31  22        u=1     $ Ge Crystal
22     0              -22  62        u=1     $ Hole
62     5  -8.96       -62            u=1     $ Cu Contact
41     6 -11.35       -41  11        u=1     $ Pb Shield around Ge
10     0                   41  11    u=1     $ Void
 2     0              -42            u=2  fill=1
                                  $ Ge-detector as an object in u=2
20     0                   42        u=2     $ Void
 3     like 2 but                            $ Ge-detector in u=3
       trcl=(0 -2.22 -11.4825   $ [x y z]-translation vector; origin is
             1   0       0      $ [xx xy xz] at Cu-target, so no translation;
             0  .9806  -.1959   $ [yx yy yz]-rotation matrix, just rotate;
             0  .1959   .9806  1)    u=3     $ [zx zy zz]
73     4  -0.00129         #3        u=3     $ Air around Ge-detector
52     0              -52  61        fill=3  $ Empty cell filled by u=3
61     5  -8.96       -61                    $ Cu-Target
71     7  -2.4        -71                    $ Concrete End Wall
100    0                   52  71            $ Void
c *
c -------------------------------------------------------------------
c *
c ------------------------SURFACES---------------------------------
c *
11   rcc 0.0 0.0  158.7    0.0 0.0  14.46    4.75     $ Al End Cap
12   rcc 0.0 0.0  159.197  0.0 0.0  13.0     4.175    $ Al Foil Cup
21   rcc 0.0 0.0  158.8    0.0 0.0  14.04    4.65     $ Inner Vacuum
22   rcc 0.0 0.0  160.49   0.0 0.0   8.51    0.575    $ Hole
23   rcc 0.0 0.0  169.0    0.0 0.0   1.5575  3.9      $ Top Vacuum
31   rcc 0.0 0.0  159.2    0.0 0.0   9.80    3.9      $ Ge Crystal
41   rcc 0.0 0.0  158.7    0.0 0.0  14.46   10.0      $ Pb Shield u=1
42   rcc 0.0 0.0  158.7    0.0 0.0  14.46   10.0      $ Pb Shield u=2
43   rcc 0.0 0.0  158.7    0.0 0.0  14.46   10.0      $ Pb Shield u=0
62   rcc 0.0 0.0  160.49   0.0 0.0  10.06    0.2      $ Cu Contact
61   rcc 0.0 0.0  0.0    0.0 0.0  -0.1     5.0        $ Cu Target
52   rcc 0.0 0.0  -20.0    0.0 0.0 279.9   200.0      $ Air Environment
71   rcc 0.0 0.0  260.0    0.0 0.0  50.0   200.0      $ Concrete End Wall
c *
```

```
c ---------------------------------------------------------------------
c *
c -------------------------MATERIALS-----------------------------------
c *
c #1 (Al End Cap)
M1     13000.02p   1.0
c #3 (Ge-crystal)
M3     32000.02p   1.0
c #4 (Air)
M4      8016.02p   0.23555
        7014.02p   0.75086
       18000.02p   0.01281
        1001.02p   0.00064
        6012.02p   0.00014
c #5 (Cu-plate)
M5     29000.02p  1.0
c #6 (Pb-shield)
M6     82000.02p  1.0
c
c #7 (Concrete End Wall)
M7     8016.02p   0.67
      14000.42c   0.33
c ---------------------------------------------------------------------
c *
c -------------------------SOURCES-------------------------------------
SDEF POS=0.0 0.0 0.3175 RAD=D2 PAR=P ERG=0.025
c
SI2 0.25
c ---------------------------------------------------------------------
c *
c -------------------------TALLIES-------------------------------------
F8:P 31
E8 0 1E-5 1000i 6
c -----------------------------------------
c *
c -------------------------Physics-------------------------------------
IMP:P,E 1 1 1 1 1 1 1 1 0 1 1 1 1 1 1 1 0       $ Importance for each cell
MODE P E                                        $ dE/dX for P,E
NPS 7E7                                         $ Number of histories
```

B.4 Attenuation Calculation

```
The 60% Ge-detector; original by A. Tonchev & A. Chyzh;
                                    (modified by S.L. Hammond)
c *
c --------------------------CELLS-------------------------------------
c *
11     1  -2.6989     -11  21               $ Al End Cap
12     1  -2.6989     -12  31 23            $ Al Foild
21     0              -21  12 22            $ Inner Vacuum
23     0              -23  22               $ Top Vacuum
24     1  -2.6989     -24  12 22            $ Al mount cup base
31     3  -5.323      -31  22               $ Ge Crystal
c 34     3  -5.323      -34  12             $ Dead Zone
22     5  -8.96       -22                   $ Hole
62     5 -8.96     -62 63                   $ Cu attenuator
63     6 -11.35     -63 62                  $ Pb attenuator
70     7  -19.1      -70  62 63 11          $ 238U
74     4  -0.00129   -74 11 62 63 70        $ Air Environment
10     0              74                    $ Void
c *
c ---------------------------------------------------------------------
c *
c -------------------------SURFACES-------------------------------------
c *
11   rcc 0.0 10.0 0.0    0.0 11.576 0.0   3.806    $ Al End Cap
12   rcc 0.0 10.50 0.0   0.0 10.576 0.0   3.306    $ Al Foil Cup
21   rcc 0.0 10.10 0.0    0.0 11.376 0.0   3.706   $ Inner Vacuum
22   rcc 0.0 11.39 0.0  0.0 7.27 0.0     0.56      $ Hole
23   rcc 0.0 18.67 0.0  0.0 2.09 0.0     3.23      $ Top Vacuum
24   rcc 0.0 20.75 0.0  0.0 0.244 0.0    3.23      $ Al mount cup base
31   rcc 0.0 10.57 0.0  0.0 8.09 0.0     3.23      $ Ge Crystal
c 34   rcc 0.0 0.0  19.11  0.0 0.1 0.0      3.23   $ Dead Zone
62   rcc 0.0 9.48  0.0  0.0 0.4 0.0    3.806       $ Cu attenuator
63   rcc 0.0 8.95  0.0   0.0 0.53 0.0    3.806     $ Pb attenuator
70   rcc 0.0 0.0 0.0      0.0 0.0 0.204    1.27    $ 238U target
74   rcc 0.0 0.0 -293.8    0.0 0.0 500    100.0    $ Air Environment
c *
c ---------------------------------------------------------------------
c *
c -------------------------MATERIALS------------------------------------
c *
c #1 (Aluminum)
M1     13000.02p   1.0
c #3 (Germanium)
M3     32000.02p   1.0
c #4 (Air)
M4      8016.02p   0.23555
        7014.02p   0.75086
       18000.02p   0.01281
        1001.02p   0.00064
        6012.02p   0.00014
c #5 (Copper)
M5     29000.02p  1.0
c #6 (Lead)
 M6     82000.02p  1.0
```

```
c #7 (238U target)
M7   92238.02p   0.9927
     92235.02p   0.0072
     92234.02p   0.0001
c
c -------------------------SOURCE---------------------------------------
c *E MeV gamma at POS=[xyz], weight 1, in vec=Z-direction under DIR=0-deg*
SDEF POS 0 0 0 RAD 0.9525 PAR=P ERG=D1
c
SI1 A 2.847 2.848 2.849 2.850 2.851 2.852 2.853 2.854
      2.855 2.856 2.857 2.858 2.859 2.860 2.861 2.862
      2.863 2.864 2.865 2.866 2.867 2.868 2.869 2.870
      2.871 2.872 2.873 2.874 2.875 2.876 2.877 2.878
      2.879 2.880 2.881 2.882 2.883 2.884 2.885 2.886
      2.887 2.888 2.889 2.890 2.891 2.892 2.893 2.894
      2.895 2.896 2.897 2.898 2.899 2.900 2.901 2.902
      2.903 2.904 2.905 2.906 2.907 2.908 2.909 2.910
      2.911 2.912 2.913 2.914 2.915 2.916 2.917 2.918
      2.919 2.920 2.921 2.922 2.923 2.924 2.925 2.926
      2.927 2.928 2.929 2.930 2.931 2.932 2.933 2.934
      2.935 2.936 2.937 2.938 2.939 2.940 2.941 2.942
      2.943 2.944 2.945 2.946 2.947 2.948 2.949 2.950
      2.951 2.952 2.953 2.954 2.955 2.956 2.957 2.958
      2.959 2.960 2.961 2.962 2.963 2.964 2.965 2.966
      2.967 2.968 2.969 2.970 2.971 2.972 2.973 2.974
      2.975 2.976 2.977 2.978 2.979 2.980 2.981 2.982
      2.983 2.984 2.985 2.986 2.987 2.988 2.989 2.990
      2.991 2.992 2.993 2.994 2.995 2.996 2.997 2.998
      2.999 3.000 3.001 3.002 3.003 3.004 3.005 3.006
      3.007 3.008 3.009 3.010 3.011 3.012 3.013 3.014
      3.015 3.016 3.017 3.018 3.019 3.020 3.021 3.022
      3.023 3.024 3.025 3.026 3.027 3.028 3.029 3.030
      3.031 3.032 3.033 3.034 3.035 3.036 3.037 3.038
      3.039 3.040 3.041 3.042 3.043 3.044 3.045 3.046
      3.047 3.048 3.049 3.050 3.051 3.052 3.053 3.054
      3.055 3.056 3.057 3.058 3.059 3.060 3.061 3.062
      3.063 3.064 3.065 3.066 3.067 3.068 3.069 3.070
      3.071 3.072 3.073 3.074 3.075 3.076 3.077 3.078
      3.079 3.080 3.081 3.082 3.083 3.084 3.085 3.086
      3.087 3.088 3.089 3.090 3.091 3.092 3.093 3.094
      3.095 3.096 3.097 3.098 3.099 3.100 3.101 3.102
      3.103 3.104 3.105 3.106 3.107 3.108 3.109 3.110
      3.111 3.112 3.113 3.114 3.115 3.116 3.117 3.118
      3.119 3.120 3.121 3.122 3.123 3.124 3.125 3.126
      3.127 3.128 3.129 3.130 3.131 3.132 3.133 3.134
      3.135 3.136 3.137 3.138 3.139 3.140 3.141 3.142
      3.143 3.144 3.145 3.146 3.147 3.148 3.149 3.150
      3.151 3.152 3.153 3.154 3.155 3.156 3.157 3.158
      3.159 3.160 3.161 3.162 3.163 3.164 3.165 3.166
      3.167 3.168 3.169 3.170 3.171 3.172 3.173 3.174
      3.175 3.176 3.177 3.178 3.179 3.180 3.181 3.182
      3.183 3.184 3.185 3.186 3.187 3.188 3.189 3.190
c
SP1   0.013 0.025 0.031 0.025 0.034 0.020 0.016 0.023
      0.024 0.043 0.026 0.026 0.021 0.020 0.027 0.029
      0.033 0.034 0.045 0.032 0.035 0.036 0.035 0.055
      0.039 0.033 0.034 0.041 0.019 0.046 0.046 0.047
      0.045 0.047 0.054 0.046 0.053 0.052 0.062 0.066
      0.051 0.061 0.061 0.062 0.064 0.080 0.084 0.066
```

```
      0.061 0.080 0.084 0.077 0.092 0.089 0.100 0.097
      0.107 0.106 0.101 0.111 0.097 0.120 0.128 0.121
      0.128 0.124 0.134 0.156 0.152 0.155 0.141 0.167
      0.170 0.176 0.167 0.178 0.172 0.183 0.192 0.200
      0.184 0.208 0.204 0.214 0.225 0.236 0.238 0.231
      0.237 0.253 0.254 0.251 0.270 0.264 0.264 0.281
      0.287 0.302 0.324 0.311 0.303 0.321 0.327 0.331
      0.337 0.342 0.347 0.352 0.365 0.380 0.373 0.380
      0.394 0.387 0.397 0.423 0.411 0.403 0.428 0.414
      0.435 0.435 0.464 0.449 0.457 0.466 0.467 0.467
      0.477 0.484 0.486 0.495 0.515 0.498 0.529 0.509
      0.519 0.514 0.541 0.537 0.522 0.542 0.538 0.555
      0.553 0.566 0.560 0.567 0.565 0.579 0.563 0.581
      0.564 0.601 0.594 0.590 0.590 0.608 0.600 0.604
      0.599 0.590 0.615 0.621 0.601 0.625 0.615 0.620
      0.612 0.619 0.622 0.641 0.615 0.639 0.646 0.626
      0.616 0.627 0.621 0.623 0.640 0.642 0.617 0.627
      0.631 0.626 0.639 0.636 0.641 0.619 0.617 0.628
      0.608 0.621 0.603 0.613 0.610 0.621 0.615 0.596
      0.607 0.596 0.581 0.600 0.578 0.592 0.573 0.551
      0.573 0.563 0.574 0.545 0.557 0.553 0.542 0.550
      0.533 0.528 0.518 0.525 0.525 0.510 0.490 0.490
      0.481 0.491 0.479 0.475 0.481 0.463 0.458 0.450
      0.447 0.435 0.441 0.431 0.422 0.425 0.407 0.407
      0.398 0.405 0.388 0.381 0.397 0.386 0.375 0.366
      0.360 0.343 0.342 0.340 0.338 0.335 0.314 0.314
      0.304 0.314 0.302 0.283 0.283 0.280 0.280 0.266
      0.257 0.259 0.237 0.246 0.236 0.232 0.229 0.211
      0.216 0.200 0.206 0.199 0.182 0.192 0.179 0.169
      0.166 0.161 0.156 0.150 0.147 0.146 0.139 0.135
      0.129 0.126 0.120 0.108 0.103 0.100 0.094 0.095
      0.090 0.081 0.077 0.073 0.078 0.073 0.065 0.059
      0.060 0.056 0.050 0.049 0.045 0.042 0.039 0.033
      0.031 0.031 0.030 0.026 0.027 0.021 0.020 0.021
      0.018 0.014 0.013 0.014 0.012 0.007 0.010 0.006
      0.007 0.006 0.006 0.004 0.004 0.004 0.003 0.003
      0.002 0.002 0.002 0.001 0.002 0.001 0.001 0.001
c ----------------------------------------------------------------------
c *
c -------------------------TALLIES--------------------------------------
FC18 *Pulse Height Ge-Detector at cell 31 Ge-crystal*
F18:P 31
E18 0.0 6000i 6.0
c ---------------------------------------------
c *
c -------------------------Physics--------------------------------------
IMP:P,E 1 1 1 1 1 1 1 1 1 1 0
MODE P E
CUT:P,E j 0.1
c
NPS 1e6
```

B.5 Compton-Scattered Spectrum Simulation

```
The 123% Ge-detector; original by A. Tonchev & A. Chyzh;
                                        (modified by S.L. Hammond)
c *
c --------------------------CELLS-----------------------------------
c *
11     1  -2.6989     -11  21        u=1
                                $ Al End Cap at 158.7cm from Cu-target
12     1  -2.6989     -12  31  23    u=1   $ Al Foild
21     0              -21  12  62    u=1   $ Inner Vacuum
23     0              -23  62        u=1   $ Top Vacuum
31     3  -5.323      -31  22        u=1   $ Ge Crystal
22     0              -22  62        u=1   $ Hole
62     5  -8.96       -62            u=1   $ Cu Contact
41     6 -11.35       -41  11        u=1   $ Pb Shield around Ge
10     0                   41  11    u=1   $ Void
c
 2     0              -42            u=2  fill=1
c                               $ Ge-detector as an object in u=2
20     0                   42        u=2   $ Void
c
 3     like 2 but                           $ Ge-detector in u=3
       trcl=(0  -1.22   6.77    $ [x y z]-translation vector; origin is
             1   0       0      $ [xx xy xz] at Cu-target, so no translation;
             0  .9781  -.2079   $ [yx yy yz]-rotation matrix, just rotate;
             0  .2079   .9781  1)    u=3   $ [zx zy zz]
73     4  -0.00129         #3        u=3   $ Air around Ge-detector
c
52     0              -52  51  61         fill=3
c                                        $ Empty cell filled by u=3
51     4  -0.00129    -51                $ Air Det 1
61     5  -8.96       -61                $ Cu-Target
71     7  -2.4        -71                $ Concrete End Wall
100    0                   52  71        $ Void
c *
c --------------------------------------------------------------------
c *
c ------------------------SURFACES-----------------------------------
c *
11   rcc 0.0 0.0  158.7    0.0 0.0  14.46    4.75      $ Al End Cap
12   rcc 0.0 0.0  159.197  0.0 0.0  13.0     4.175     $ Al Foil Cup
21   rcc 0.0 0.0  158.8    0.0 0.0  14.04    4.65      $ Inner Vacuum
22   rcc 0.0 0.0  160.49   0.0 0.0   8.51    0.575     $ Hole
23   rcc 0.0 0.0  169.0    0.0 0.0   1.5575  3.9       $ Top Vacuum
31   rcc 0.0 0.0  159.2    0.0 0.0   9.80    3.9       $ Ge Crystal
41   rcc 0.0 0.0  158.7    0.0 0.0  14.46   10.0       $ Pb Shield u=1
42   rcc 0.0 0.0  158.7    0.0 0.0  14.46   10.0       $ Pb Shield u=2
43   rcc 0.0 0.0  158.7    0.0 0.0  14.46   10.0       $ Pb Shield u=0
62   rcc 0.0 0.0  160.49   0.0 0.0  10.06    0.2       $ Cu Contact
61   rcc 0.0 0.0    0.0    0.0 0.0  -0.1     5.0       $ Cu Target
51   rcc 0.0 0.0  -10.0    0.0 0.0   0.2     0.635     $ Air Det 1
52   rcc 0.0 0.0  -20.0    0.0 0.0 279.9   100.0       $ Air Environment
71   rcc 0.0 0.0  260.0    0.0 0.0  50.0   100.0       $ Concrete End Wall
c *
c --------------------------------------------------------------------
```

```
c *
c -------------------------MATERIALS---------------------------------
c *
c #1 (Al End Cap)
M1     13000.02p   1.0
c #3 (Ge-crystal)
M3     32000.02p   1.0
c #4 (Air)
M4      8016.02p   0.23555
        7014.02p   0.75086
       18000.02p   0.01281
        1001.02p   0.00064
        6012.02p   0.00014
c #5 (Cu-plate)
M5     29000.02p  1.0
c #6 (Pb-shield)
M6     82000.02p  1.0
c
c #7 (Concrete End Wall)
M7     8016.02p   0.67
      14000.42c   0.33
c ---------------------------------------------------------------------
c *
c -------------------------SOURCES-----------------------------------
c *9.5 MeV gamma at POS=[xyz], weight 1, in vec=Z-direction under DIR=0-deg*
SDEF POS=0.0 2.54 -4.0 AXS=0 0 1 VEC=0 0 1 DIR=1.0
     RAD=0.635 PAR=2 ERG=D1
c
SI1 A 2.301 2.302 2.303 2.304 2.305 2.306 2.307 2.308
      2.309 2.310 2.311 2.312 2.313 2.314 2.315 2.316
      2.317 2.318 2.319 2.320 2.321 2.322 2.323 2.324
      2.325 2.326 2.327 2.328 2.329 2.330 2.331 2.332
      2.333 2.334 2.335 2.336 2.337 2.338 2.339 2.340
      2.341 2.342 2.343 2.344 2.345 2.346 2.347 2.348
      2.349 2.350 2.351 2.352 2.353 2.354 2.355 2.356
      2.357 2.358 2.359 2.360 2.361 2.362 2.363 2.364
      2.365 2.366 2.367 2.368 2.369 2.370 2.371 2.372
      2.373 2.374 2.375 2.376 2.377 2.378 2.379 2.380
      2.381 2.382 2.383 2.384 2.385 2.386 2.387 2.388
      2.389 2.390 2.391 2.392 2.393 2.394 2.395 2.396
      2.397 2.398 2.399 2.400 2.401 2.402 2.403 2.404
      2.405 2.406 2.407 2.408 2.409 2.410 2.411 2.412
      2.413 2.414 2.415 2.416 2.417 2.418 2.419 2.420
      2.421 2.422 2.423 2.424 2.425 2.426 2.427 2.428
      2.429 2.430 2.431 2.432 2.433 2.434 2.435 2.436
      2.437 2.438 2.439 2.440 2.441 2.442 2.443 2.444
      2.445 2.446 2.447 2.448 2.449 2.450 2.451 2.452
      2.453 2.454 2.455 2.456 2.457 2.458 2.459 2.460
      2.461 2.462 2.463 2.464 2.465 2.466 2.467 2.468
      2.469 2.470 2.471 2.472 2.473 2.474 2.475 2.476
      2.477 2.478 2.479 2.480 2.481 2.482 2.483 2.484
      2.485 2.486 2.487 2.488 2.489 2.490 2.491 2.492
      2.493 2.494 2.495 2.496 2.497 2.498 2.499 2.500
      2.501 2.502 2.503 2.504 2.505 2.506 2.507 2.508
      2.509 2.510 2.511 2.512 2.513 2.514 2.515 2.516
      2.517 2.518 2.519 2.520 2.521 2.522 2.523 2.524
      2.525 2.526 2.527 2.528 2.529 2.530 2.531 2.532
      2.533 2.534 2.535 2.536 2.537 2.538 2.539 2.540
      2.541 2.542 2.543 2.544 2.545 2.546 2.547 2.548
```

```
        2.549 2.550 2.551 2.552 2.553 2.554 2.555 2.556
        2.557 2.558 2.559 2.560 2.561 2.562 2.563 2.564
        2.565 2.566 2.567 2.568 2.569 2.570 2.571 2.572
        2.573 2.574 2.575 2.576 2.577 2.578 2.579 2.580
        2.581 2.582 2.583 2.584 2.585 2.586 2.587 2.588
        2.589 2.590 2.591 2.592 2.593 2.594 2.595 2.596
        2.597 2.598 2.599 2.600 2.601 2.602 2.603 2.604
        2.605 2.606 2.607 2.608 2.609 2.610 2.611 2.612
        2.613 2.614 2.615 2.616 2.617 2.618 2.619 2.620
        2.621 2.622 2.623 2.624 2.625 2.626 2.627 2.628
        2.629 2.630 2.631 2.632 2.633 2.634 2.635 2.636
        2.637 2.638 2.639 2.640 2.641 2.642 2.643 2.644
        2.645 2.646 2.647 2.648 2.649 2.650 2.651 2.652
        2.653 2.654 2.655 2.656 2.657 2.658 2.659 2.660
        2.661 2.662 2.663 2.664 2.665 2.666 2.667 2.668
        2.669 2.670 2.671 2.672 2.673 2.674 2.675 2.676
        2.677 2.678 2.679 2.680 2.681 2.682 2.683 2.684
        2.685 2.686 2.687 2.688 2.689 2.690 2.691 2.692
        2.693 2.694 2.695 2.696 2.697 2.698 2.699 2.700
c
SP1     0.001 0.017 0.002 0.002 0.007 0.012 0.009 0.011
        0.014 0.012 0.008 0.017 0.018 0.035 0.031 0.018
        0.024 0.013 0.011 0.013 0.014 0.027 0.023 0.028
        0.019 0.013 0.038 0.025 0.032 0.022 0.014 0.046
        0.036 0.037 0.033 0.030 0.033 0.053 0.043 0.053
        0.043 0.049 0.052 0.060 0.036 0.047 0.056 0.059
        0.047 0.056 0.058 0.063 0.071 0.074 0.075 0.060
        0.073 0.080 0.081 0.090 0.095 0.100 0.091 0.087
        0.088 0.102 0.094 0.095 0.101 0.105 0.113 0.110
        0.109 0.117 0.121 0.124 0.126 0.120 0.130 0.129
        0.140 0.135 0.148 0.150 0.141 0.151 0.144 0.171
        0.163 0.176 0.174 0.180 0.188 0.211 0.174 0.193
        0.192 0.217 0.215 0.211 0.223 0.239 0.234 0.232
        0.240 0.255 0.253 0.270 0.279 0.282 0.298 0.282
        0.290 0.294 0.329 0.312 0.321 0.315 0.343 0.344
        0.337 0.347 0.357 0.346 0.369 0.384 0.379 0.397
        0.412 0.415 0.429 0.427 0.434 0.440 0.445 0.445
        0.456 0.473 0.490 0.481 0.496 0.505 0.494 0.512
        0.529 0.515 0.533 0.558 0.560 0.555 0.552 0.563
        0.563 0.567 0.588 0.578 0.594 0.617 0.594 0.613
        0.622 0.633 0.630 0.642 0.633 0.642 0.655 0.656
        0.657 0.675 0.679 0.664 0.692 0.687 0.691 0.703
        0.695 0.697 0.706 0.722 0.704 0.727 0.726 0.733
        0.730 0.734 0.744 0.720 0.715 0.735 0.746 0.726
        0.737 0.733 0.716 0.732 0.738 0.742 0.744 0.726
        0.733 0.751 0.742 0.721 0.715 0.712 0.728 0.729
        0.709 0.704 0.708 0.697 0.699 0.675 0.673 0.666
        0.666 0.657 0.651 0.628 0.624 0.609 0.612 0.611
        0.618 0.572 0.563 0.570 0.534 0.564 0.532 0.510
        0.509 0.503 0.482 0.475 0.462 0.470 0.449 0.446
        0.436 0.424 0.416 0.403 0.408 0.395 0.392 0.374
        0.368 0.356 0.346 0.333 0.325 0.334 0.322 0.308
        0.304 0.306 0.285 0.285 0.276 0.275 0.268 0.264
        0.252 0.241 0.239 0.228 0.223 0.222 0.211 0.206
        0.202 0.197 0.187 0.179 0.179 0.179 0.169 0.162
        0.160 0.148 0.150 0.141 0.134 0.135 0.126 0.122
        0.109 0.112 0.104 0.094 0.092 0.090 0.089 0.080
        0.075 0.074 0.069 0.067 0.066 0.066 0.058 0.050
        0.051 0.043 0.046 0.048 0.043 0.035 0.033 0.031
```

```
      0.025 0.027 0.024 0.023 0.024 0.025 0.026 0.021
      0.018 0.014 0.013 0.009 0.010 0.007 0.006 0.007
      0.007 0.006 0.005 0.005 0.004 0.003 0.004 0.003
      0.002 0.002 0.002 0.001 0.002 0.001 0.002 0.001
      0.001 0.000 0.001 0.001 0.001 0.001 0.001 0.001
      0.001 0.001 0.001 0.000 0.001 0.001 0.001 0.001
      0.001 0.001 0.000 0.001 0.000 0.000 0.001 0.001
      0.001 0.001 0.000 0.001 0.000 0.000 0.001 0.001
      0.001 0.000 0.001 0.001 0.000 0.001 0.001 0.001
      0.001 0.000 0.001 0.000 0.001 0.001 0.001 0.001
      0.001 0.001 0.001 0.001 0.001 0.000 0.001 0.001
c
c ---------------------------------------------------------------------
c *
c -------------------------TALLIES-------------------------------------
c
FC8 *Pulse Height Ge-Detector at cell 31 Ge-crystal*
F8:P 31
c
E8 0.0 6000i 4.0
c ---------------------------------------------
c *
c -------------------------Physics-------------------------------------
IMP:P 1 1 1 1 1 1 1 1 0 1 1 1 1 1 1 1 1 0     $ Importance for each cell
MODE P                                        $ dE/dX for P,E
c
CUT:P j 0.001                                 $10 keV cutoff for P,E
c
NPS 9e8                                       $ Number of histories
```

Appendix C

Sample TALYS Input

C.1 Total Photoabsorption Cross Section

```
projectile    g
element       92
mass          238
energy        energies
ejectiles     g n
#
ldmodel       2
shellmodel    2
spincutmodel  1
strength      2
strengthM1    2
preeqmode     1
mpreeqmode    2
pairmodel     1
fismodel      5
#
partable y
urr y
best n
fullhf y
autorot y
optmodall y
recoil y
fission y
gshell y
electronconv y
preequilibrium y
multipreeq y
twocomponent y
statepot y
colenhance y
colldamp y
channels y
channelenergy y
rotational n
maxrot 4
maxband 6
gammax 2
#
sysreaction n
maxchannel 1
```

```
maxlevelstar 30
maxlevelsres 30
Nlevels 92 238 0
transpower 2
transeps  0
Elow .001
#
aadjust 92 238 0.05
pair 92 238 0.31493
pairconstant 1
Pshift 92 238 0
Pshiftconstant 0
deltaW 92 238 3.01190
gammald 92 238 0.06621
D0 92 238 3.5
# Nlow 92 238 3
# Ntop 92 238 18
#
egr 92 238 10.8466 E1 1
egr 92 238 14.0378 E1 2
sgr 92 238 344.231 E1 1
sgr 92 238 430.312 E1 2
ggr 92 238 3.02075 E1 1
ggr 92 238 4.9271 E1 2
#
outgamma  y
outdensity y
outexcitation y
#
filedensity y
filegamdis y
filetotal y
```

C.2 Total Photoabsorption Cross Section with PDR

```
projectile    g
element       92
mass          238
energy        energies
ejectiles     g n
#
ldmodel       2
shellmodel    2
spincutmodel  1
strength      2
strengthM1    2
preeqmode     1
mpreeqmode    2
pairmodel     1
fismodel      5
#
partable y
urr y
```

```
best n
fullhf y
autorot y
optmodall y
recoil y
fission y
gshell y
electronconv y
preequilibrium y
multipreeq y
twocomponent y
statepot y
colenhance y
colldamp y
channels y
channelenergy y
rotational n
maxrot 4
maxband 6
gammax 2
#
sysreaction n
maxchannel 1
maxlevelstar 30
maxlevelsres 30
Nlevels 92 238 0
transpower 2
transeps  0
Elow .001
#
aadjust 92 238 0.05
pair 92 238 0.31493
pairconstant 1
Pshift 92 238 0
Pshiftconstant 0
deltaW 92 238 3.01190
gammald 92 238 0.06621
D0 92 238 3.5
# Nlow 92 238 3
# Ntop 92 238 18
#
egr 92 238 10.8466 E1 1
egr 92 238 14.0378 E1 2
sgr 92 238 344.231 E1 1
sgr 92 238 430.312 E1 2
ggr 92 238 3.02075 E1 1
ggr 92 238 4.9271 E1 2
#
epr 92 238 6.15 E1 1
spr 92 238 13 E1 1
gpr 92 238 1 E1 1
#
outgamma  y
outdensity y
outexcitation y
#
filedensity y
filegamdis y
filetotal y
```

Bibliography

[1] R. D. Heil et al. Observation of orbital magnetic dipole strength in the actinide nuclei ^{232}Th and ^{238}U. *Nucl. Phys.*, **A476**:39–47, 1988.

[2] D. Zawischa et al. Magnetic dipole strength functions in heavy deformed nuclei. *Phys. Rev. C*, **42**:1461–1471, 1990.

[3] A. Richter. Probing the nuclear magnetic dipole response with electrons, photons and hadrons. *Prog. Part. Nucl. Phys.*, **34**:261–284, 1995.

[4] A. Parker. Taking a Gander with Gamma Rays. *Science and Technology Review*, December:16–17, 2006.

[5] U.S. Department of Homeland Security. Fact Sheet: Domestic Nuclear Detection Office (Press Release). Technical report, DNDO, 2005.

[6] Passport Systems, Inc., 2002.

[7] *Rapiscan Systems*. OSI Systems, INC., 1993.

[8] Pruet et al. Detecting clandestine material with nuclear resonance fluorescence. *J. Appl. Phys.*, **99**:123102, 2006.

[9] C.A. Hagmann et al. Transmission-based detection of nuclides with nuclear resonance fluorescence using a quasimonoenergetic photon source. *J. Appl. Phys.*, **106**: 084901, 2009.

[10] International Atomic Energy Agency. Press Release for the Illicit Trafficking Database. Technical report, IAEA, 2004.

[11] R. Hajima et al. Proposal of Nondestructive Radionuclide Assay Using a High-Flux Gamma-Ray Source and Nuclear Resonance Fluorescence. *Nucl. Sci. and Tech.*, **45**: 441–451, 2008.

[12] T. Hayakawa et al. Nondestructive assay of plutonium and minor actinide in spent fuel using nuclear resonance fluorescence with laser Compton scattering γ-rays. *Nucl. Instr. Meth. A*, **621**:695–700, 2010.

[13] H.A. Bethe and G. Placzek. Resonance Effects in Nuclear Processes. *Phys. Rev.*, 51: 450–484, 1937.

[14] A. S. Adekola et al. Discovery of low-lying $E1$ and $M1$ strengths in ^{232}Th. *Phys. Rev. C*, 83:034615, 2011.

[15] U. Kneissl et al. Investigation of nuclear structure by resonance fluorescence scattering. *Prog. Part. Nucl. Phys.*, **37**:349–433, 1996.

[16] K. Siegbahn. *α-, β- and γ-ray Spectroscopy*. North-Holland Pub. Co., Amsterdam, 1965.

[17] W.E. Lamb. Capture of Neutrons by Atoms in a Crystal. *Phys. Rev.* , 55:190–197, 1939.

[18] F. Metzger. Resonance Fluorescence in Nuclei. *Prog. Nucl. Phys.*, **7**:53–88, 1977.

[19] E. Hammarén et al. Microscopic and phenomenological analysis of the Alaga rule for dipole states. *Nucl. Phys.*, **A541**:226–240, 1992.

[20] P. Schuck P. Ring and W. Beiglböck. *The nuclear many-body problem*. Springer-Verlag, Berlin, 1980.

[21] P. Papatzacos and K. Mork. Delbrück scattering. *Phys. Rep.*, **21**:81–118, 1975.

[22] L. Kissel et al. Rayleigh scattering by neutral atoms, 100 ev to 10 MeV. *Phys. Rev. A*, **22**:1970–2004, 1980.

[23] L. Kissel. RTAB: the Rayleigh scattering database. *Radiation Physics and Chemistry*, **59**:185–200, 2000.

[24] J.J. Sakurai and S.F. Tuan. *Modern Quantum Mechanics*. Addison-Wesley Pub. Co., Boston, 1994.

[25] A. Di Piazza and A. I. Milstein. Delbrück scattering in combined Coulomb and laser fields. *Phys. Rev. A*, **77**:042102, 2008.

[26] P. Papatzacos and K. Mork. Delbrück scattering calculations. *Phys. Rev. D*, **12**:206–218, 1975.

[27] M. Schumacher et al. The energy dependence of Delbrück scattering investigated at $Z = 73$, 82, and 92. *Nucl. Phys. A*, **346**:418–430, 1980.

[28] H. P. Loens. *Dissertation D17*. PhD thesis, Technische Hochschule Darmstadt, 2011. (unpublished).

[29] K. Heyde et al. Magnetic dipole excitations in nuclei: Elementary modes of nucleonic motion. *Rev. Mod. Phys.*, **82**:2365–2419, 2010.

[30] A. A. Kuliev et al. The low-energy dipole structure of ^{232}Th, ^{236}U, and ^{238}U actinide nuclei. *Eur. Phys. J. A*, **43**:313–321, 2010.

[31] V. G. Soloviev et al. Dipole strength distribution in doubly even deformed nuclei. *J. Phys. G*, **25**:1023–1042, 1999.

[32] F. Iachello. Local versus global isospin symmetry in nuclei. *Phys. Lett.*, **160B**:1–4, 1985.

[33] A.P. Tonchev et al. Overview: Nuclear Structure Study at HIGS. Technical report, Triangle Universities Nuclear Laboratory, 2005.

[34] P. Ring. New developments in covariant density functional theory. Technical report, Technische Universitat München, 2009. Arctic FIDIPRO-EFES Workshop, April 20-24, 2009.

[35] D. Bohle et al. New magnetic dipole excitation mode studied in the heavy deformed nucleus ^{156}Gd by inelastic electron scattering. *Phys. Lett.*, **137B**:27–31, 1984.

[36] N. Pietralla et al. Systematics of the excitation energy of the 1^+ scissors mode and its empirical dependence on the nuclear deformation parameter. *Phys. Rev. C*, **58**: 184–190, 1998.

[37] A. Zilges et al. Strong dipole excitations around 1.8 MeV in ^{238}U. *Phys. Rev. C*, **52**: R468–R470, 1995.

[38] J. Enders et al. Parameter-free description of orbital magnetic dipole strength. *Phys. Rev. C*, **71**:014306, 2005.

[39] H. J. Wörtche. *Dissertation D17*. PhD thesis, Technische Hochschule Darmstadt, 1994. (unpublished).

[40] D. Frekers et al. Spin excitations in the deformed nuclei ^{154}Sm, ^{158}Gd and ^{168}Er. *Phys. Lett.*, **244B**:178–182, 1990.

[41] A. Veyssière et al. A study of the photofission and photoneutron processes in the giant dipole resonance of ^{232}Th, ^{238}U, and ^{237}Np. *Nucl. Phys.*, **A199**:45–64, 1973.

[42] J. T. Caldwell et al. Giant resonance for the actinide nuclei: Photoneutron and photofission cross sections for ^{235}U, ^{236}U, ^{238}U, and ^{232}Th. *Phys. Rev. C*, **21**:1215–1231, 1980.

[43] Y. Suzuki et al. New Type of Dipole Vibration in Nuclei. *Prog. Theor. Phys.*, **83**: 180–184, 1990.

[44] Ponomarev et al. Double giant resonances in deformed nuclei. *Phys. Rev. C*, **58**: 27502753, 1998.

[45] A. P. Tonchev et al. Spectral Structure of the Pygmy Dipole Resonance. *Phys. Rev. Lett.*, **104**:072501, 2010.

[46] U. Kneissl et al. Low-lying dipole modes in vibrational nuclei studied by photon scattering. *J. Phys. G.*, **32**:R217–R252, 2006.

[47] P. Adrich et al. Evidence for Pygmy and Giant Dipole Resonances in ^{130}Sn and ^{132}Sn. *Phys. Rev. Lett.*, **95**:132501, 2005.

[48] G. Rusev et al. Multipole mixing ratios of transitions in ^{11}B. *Phys. Rev. C (R)*, **79**: 061302, 2009.

[49] F. Dönau et al. Effect of nuclear deformation on the electric-dipole strength in the particle-emission threshold region. *Phys. Rev. C*, **76**:014317, 2007.

[50] S. Goriely. Radiative neutron captures by neutron-rich nuclei and the r-process nucleosynthesis. *Phys. Lett. B*, **436**:10–18, 1998.

[51] G. A. Bartholomew et al. Gamma-ray strength function. *Adv. Nucl. Phys.*, **7**:229–324, 1973.

[52] H. Maser et al. Systematics of low-lying dipole excitations in the deformed even-even nuclei ^{164,166,168,170}Er. *Phys. Rev. C*, **53**:2749–2762, 1996.

[53] H. Friedrichs et al. Low-lying $E1$ and $M1$ strengths in the deformed nucleus ^{160}Gd. *Nucl. Phys.*, **A567**:266–280, 1994.

[54] J. Margraf et al. Photoexcitation of low-lying dipole transitions in ^{236}U. *Phys. Rev. C*, **42**:771–774, 1990.

[55] A. A. Kuliev et al. Fully renormalized quasi-particle random phase approximation, spurious states and ground state correlations. *J. Phys. G*, **30**:1253–1267, 2004.

[56] A. Richter. Electron Scattering and Elementary Excitations. *Nucl. Phys.*, **A522**: 139c–166c, 1991.

[57] W. Ziegler et al. Low-energy dipole-strength distributions in ^{148,150,152,154}Sm. *Nucl. Phys.*, **A564**:366–382, 1993.

[58] N. Pietralla et al. The scissors mode and other magnetic and electric dipole excitations in the transitional nuclei ^{178,180}Hf. *Nucl. Phys. A*, **618**:141–165, 1997.

[59] E. Guliyev et al. Low-Lying Dipole Excitations in the Deformed EvenEven Isotopes 154 − 160Gd. *Act. Phys. Pol. B*, **40**:653–656, 2009.

[60] E. Lipparini and S. Stringari. Rotational magnetic state in deformed metal clusters. *Phys. Rev. Lett.*, **63**:570–572, 1989.

[61] J. W. Knowles and O. Y. Mafra. Intermediate Structure in the Photoneutron, Photofission, and Photoabsorption Cross Sections of ^{238}U at the Fission Threshold. *Proc. Intl. Conf. Photonucl. React. Appl.*, pages 647–843, 1973.

[62] W. Mückenheim and M. Schumacher. Delbrück and Rayleigh scattering by uranium investigated at photon energies between 0.1 and 1.5 MeV. *J. Phys. (London) G*, **6**: 1237–1250, 1980.

[63] W. Mückenheim et al. Nuclear Resonance Fluorescence in ^{238}U and a New Approach to Doppler-Shift-Attenuation Using High Speed Rotation. *Z. Phys. A*, **300**:43–46, 1981.

[64] P. Rullhusen et al. Coulomb correction effect in Delbrück scattering and nuclear resonance fluorescence of 2 to 10 MeV photons on ^{238}U. *Nucl. Phys.*, **A382**:79–96, 1982.

[65] U. Zurmühl et al. Nuclear resonance scattering studies on ^{238}U using a dense series of γ-ray photons. *Z. Phys. A*, **314**:171–179, 1983.

[66] Y. Birenbaum et al. Photon scattering on ^{238}U and the interpretation of near-threshold photofission resonances. *Phys. Rev. C*, **36**:1293–1297, 1987.

[67] G. A. Warren et al. On the Search for Nuclear Resonance Fluorescence Signatures of ^{235}U and ^{238}U Above 3 MeV. *IEEE Trans. on Nucl. Sci.*, **57**:317–322, 2010.

[68] B. J. Quiter et al. Transmission nuclear resonance fluorescence measurements of ^{238}U in thick targets. *Nucl. Instr. Meth. B*, **269**:1130–1139, 2011.

[69] W. Bertozzi and R. J. Ledoux. Nuclear resonance fluorescence imaging in non-intrusive cargo inspection. *Nucl. Instr. Meth. B*, 241:820–825, 2005.

[70] W. Bertozzi et al. Nuclear resonance fluorescence and effective Z determination applied to detection and imaging of special nuclear material, explosives, toxic substances and contraband. *Nucl. Instr. Meth. B*, 261:331–336, 2007.

[71] H. R. Weller et al. Research opportunities at the upgraded HIγS facility. *Prog. Part. Nucl. Phys.*, **62**:257–303, 2009.

[72] N. Pietralla et al. Parity Measurements of Nuclear Levels Using a Free-Electron-Laser Generated γ-Ray Beam. *Phys. Rev. Lett.*, **88**:012502, 2002.

[73] J. Apostolakis et al. *GEANT - Detector Description and Simulation Tool, CERN Program Library Long Writeup W5013*. CERN, Geneva, Switzerland, 1993.

[74] J. F. Briemeister. MCNP- A general Monte Carlo N-particle transport code. Technical Report LA-12625-M, Los Alamos National Laboratory, 1993.

[75] A. J. Koning et al. TALYS: A nuclear reaction program. Technical Report NRG-report 21297/04.62741/P, Los Alamos National Laboratory, 2004.

[76] T. Belgya et al. *Handbook for calculations of nuclear reaction data, RIPL-2*. IAEA, Vienna, Austria, 2006.

[77] J. Theuerkauf et al. *Program Tv*. Institute for Nuclear Physics, Cologne, 1993.

[78] E. Kwan et al. Discrete deexcitations in ^{235}U below 3 MeV from nuclear resonance fluorescence. *Phys. Rev. C*, 83 (R):041901, 2011.

[79] National Nuclear Data Center. information extracted from the Chart of Nuclides database. Technical report, Brookhaven National Laboratory, 2011.

[80] O. Klein and Y. Nishina. On the Scattering of Radiation by Free Electrons after the New Relativistic Quantum Dynamics of Dirac. *Z. Phys. A*, **52**:853–868, 1929.

[81] W. Heitler. *The Quantum Theory of Radiation*. Clarendom Press, Oxford, 1954.

[82] D. A. Gedcke. How Counting Statistics Controls Detection Limits and Peak Precision. Technical report, ORTEC, 2005.

[83] K. Debertin and R.G. Helmer. *Gamma- and X-Ray Spectrometry with Semiconductor Detectors*. North-Holland Pub. Co., Amsterdam, 1988.

[84] J.R. Taylor. *An introduction to error analysis: the study of uncertainties in physical measurements*. University Science Books, 1997.

[85] M.J. Berger et al. XCOM: Photon Cross Sections Database. Technical report, NIST, 2010.

[86] W.R. Leo. *Techniques for Nuclear and Particle Physics Experiments (editor - W.D. Hamilton)*. Springer-Verlag, Berlin, 1994.

[87] G. De Franceschi et al. Reformulation of the two-rotor model. *Phys. Rev. C*, **29**: 1496–1509, 1984.

[88] D. R. Bes and R. A. Broglia. Rotational Isovector $k^\pi = 1^+$ Mode in Deformed Nuclei. *Phys. Lett.*, **137B**:141–144, 1984.

[89] P. Van Isacker. M1 Transition Strengths in the Neutron-Proton Interacting Boson Model. *Phys. Lett.*, **144B**:1–4, 1984.

[90] R.F. Casten A. Wolf and D.D. Warner. g Factors in Heavy Nuclei and the Proton-Neutron Interaction. *Phys. Lett. B*, **190**:19–24, 1987.

[91] N. Lo Iudice and A. Richter. Scissors mode and nuclear deformation. A phenomenological model independent analysis. *Phys. Lett. B*, **304**:193–197, 1993.

[92] R. Nojarov et al. Orbital and spin $M1$ excitations in actinide nuclei. *Nucl. Phys.*, **A563**:349–386, 1993.

[93] P. Axel et al. Intermediate Structure in the Photon Interaction Cross Sections of Sn and Zr. *Phys. Rev. C*, **2**:689–711, 1970.

[94] A. Zilges et al. Uncommon decay branching ratios of spin-one states in the rare-earth region and evidence for K mixing. *Phys. Rev. C*, **42**:1945–1947, 1990.

[95] T. Guhr et al. On the nature of low-lying electric dipole excitations in light and heavy deformed nuclei. *Nucl. Phys.*, **A501**:95–107, 1989.

[96] J. Reiter and H. L. Harney. Isospin mixing matrix elements extracted from isobaric analog resonances. *Z. Phys. A*, **337**:121–129, 1990.

[97] A. Zilges et al. Admixture of the giant dipole resonance to low lying 1^--states in heavy nuclei. *Z. Phys. A*, **341**:489–490, 1992.

[98] C.T. Angell. *Dissertation*. PhD thesis, University of North Carolina at Chapel Hill, 2009. (unpublished).

[99] W. J. Walsh et al. Application of a Laser-Wakefield Driven Monochromatic Photon Source to Nuclear Resonance Fluorescence. *IEEE Nucl. Sci. Symp. Conf.*, **N04-4**: 80–85, 2009.

[100] D. Umstadter et al. Development of a Source of Quasi-Monoenergetic Mev-Energy Photons for Detection of Special Nuclear Materials. *Conf. Appl. Accl. Res. Ind. 20th Int. Conf.*, **CP1099**:606–609, 2009.